

# **Hierarchical Structured Porous Carbon Materials: Design, Synthesis, and Their Application in Energy Conversion**

**Dissertation**

zur Erlangung des Grades

des Doktors der Naturwissenschaften

der Naturwissenschaftlich-Technischen Fakultät III

der Universität des Saarlandes

von

**Eun-Jin Oh**

**Saarbrücken**

**2016**

Tag des Kolloquiums: 31. 10. 2016

Dekan: Prof. Dr. Guido Kickelbick

Berichterstatter: Prof. Dr. Rolf Hempelmann

Prof. Dr. David Scheschkewitz

Vorsitz: Prof. Dr. Kaspar Hegetschweiler

Akad. Mitarbeiter: Dr. Valeri G. Grigoryan

## **Abstract**

Polymer electrolyte membrane fuel cells (PEMFC) are one of the most promising clean energy technologies under development. The major advantages include electrical efficiencies of up to 60 %, high energy densities (relative to batteries), and low emissions. However, the main obstacles to a broad commercialization of PEMFC are largely related to the limitations of the catalyst, typically platinum (Pt). Because of the high cost and limited resources of Pt, efforts are needed to identify metal-free catalysts or efficient carbon supports for the oxygen reduction reaction (ORR) in fuel cells. In the field of electrocatalysis, catalysts supported on high-surface area materials have been developed to increase their electrochemically active surface area. In addition, the performance of many electrocatalytical processes such as energy storage/-conversion, production of chemicals, biotechnological or environmental related applications depends on the structure and electronic conductivity of the used catalyst supports. The development of high effective catalyst supports could decrease the energy consumption of electrochemical processes and could lead to a reduction of greenhouse gases. Especially, hierarchical structured porous carbons with heteroatoms are proposed to increase the catalytic activity due to a high specific surface area and high electrical conductivity. Therefore, we suggest a very simple and cost effective way to produce conductive carbon supports coated with a nitrogen-containing carbon layer. The process works with the thermal decomposition of a suitable ionic liquid (IL) on the surface of different types of carbon materials (foam structures, graphene-like structures, CNTs, particles). The nitrogen content in the microporous coatings and therefore the electronic conductivity could be improved. In this work the preparation, characterization and also the fuel cell application of hierarchical structured carbon foams coated with a nitrogen-containing carbon layer are presented.

## Zusammenfassung

Polymerelektrolytmembran-Brennstoffzellen (PEMFC) gehören zu den vielversprechendsten Technologien zur Bereitstellung von sauberer Energie. Die wesentlichen Vorteile sind hohe Wirkungsgrade (bis zu 60%), hohe Energiedichten (verglichen mit Batterien) und niedrige Emissionen. Allerdings wird eine breite Kommerzialisierung der PEM Brennstoffzellen durch die Verfügbarkeit der Platinkatalysatoren behindert. Wegen der hohen Kosten und der begrenzten Ressourcen an Pt sind Forschungen erforderlich um metallfreie Katalysatoren oder effiziente Kohleträger für die Sauerstoffreduktion (ORR) zu entwickeln. Im Bereich der Elektrokatalyse wurden Katalysatoren entwickelt, die auf Materialien mit großer Oberfläche geträgert sind um deren elektrochemisch aktive Fläche zu erhöhen. Darüber hinaus ist die Leistungsfähigkeit vieler elektrokatalytischer Prozesse wie Energiespeicherung/-umwandlung, die Produktion von Chemikalien, biotechnologischen oder umweltbezogenen Anwendungen abhängig von der Struktur und der elektronischen Leitfähigkeit der verwendeten Katalysatorträger. Die Entwicklung von hochwirksamen Katalysatorträgern könnte den Energieverbrauch der elektrochemischen Prozesse senken und dadurch die Erzeugung von Treibhausgasen verringern. Insbesondere poröse, hierarchisch strukturierte und mit Heteroatomen dotierte Kohlenstoffmaterialien werden eingesetzt, um die katalytische Aktivität aufgrund einer hohen spezifischen Oberfläche und elektrischen Leitfähigkeit zu erhöhen. Deshalb schlagen wir eine sehr einfache und kostengünstige Methode vor um Kohlenstoffträger mit einer leitfähigen stickstoffhaltigen Kohlenstoffschicht zu beschichten. Das Verfahren arbeitet mit der thermischen Zersetzung einer geeigneten ionischen Flüssigkeit (IL) auf der Oberfläche von verschiedenen Kohlenstoffmaterialien (Schaumstrukturen, graphenartige Strukturen, CNTs, Partikel). Der Stickstoffgehalt in der mikroporösen Schicht und damit die elektronische Leitfähigkeit können dadurch gesteigert werden. In dieser Arbeit wird die Herstellung, Charakterisierung und Brennstoffzellenanwendung eines hierarchischen strukturierten Kohlenstoffschaums, welcher mit einer stickstoffhaltigen Kohlenstoffschicht beschichtet wurde, vorgestellt.

# Table of Contents

<b>Abstract</b>	<b>ii</b>
<b>Zusammenfassung</b>	<b>iii</b>
<b>Table of Contents</b>	<b>iv</b>
<b>List of abbreviation</b>	<b>viii</b>
<b>1. Introduction</b>	<b>1</b>
<b>2. Scientific / Technological Background</b>	<b>3</b>
2.1 Fuel Cells in General	3
2.2 Types of Fuel Cells	3
2.3 PEM Fuel Cell	5
2.3.1 Basic Structure and Operation	5
2.3.2 Polarization Curve Losses	7
2.3.3 Components of PEMFC	10
2.3.3.1 Membrane	11
2.3.3.2 Catalyst Layer	12
2.3.3.3 Gas Diffusion Layer	13
2.3.3.4 Membrane Electrode Assembly	14
2.3.3.5 Bipolar Plates	15
2.3.3.6 Electrode	17
2.4 Catalyst Supports	19
2.4.1 Types of Catalyst Supports	20
2.4.1.1 Metals	20
2.4.1.2 Carbon Nanotubes	21
2.4.1.3 Carbon Nanofibers	21
2.4.1.4 Mesoporous Carbon	21
2.4.1.5 Diamond	22
2.4.1.6 Graphene	22
2.4.2 Recent Development	24
2.4.3 Hierarchical Porous Carbon	24
2.4.4 Hierarchically Structured Nitrogen-Coated Porous Carbon	26
2.4.5 Catalytic Property of Nitrogen-Containing Carbon	27
2.4.5.1 Different Types of Nitrogen Species	29

2.4.5.2	Oxygen Reduction Reaction	30
2.4.5.3	Chemical Stability	32
2.4.5.4	Electronic Conductivity	32
<b>3.</b>	<b>Characterization Techniques</b>	<b>34</b>
3.1	Electron Microscopy Techniques	34
3.1.1	Scanning Electron Microscopy (SEM)	34
3.1.2	Transmission Electron Microscopy (TEM)	34
3.1.3	Energy Dispersion X-ray spectroscopy (EDX)	34
3.2	Structural Characterization	35
3.2.1	Powder X-ray Diffraction (XRD)	35
3.3	Chemical and Physicochemical Characterization	35
3.3.1	CHN analysis	35
3.3.2	Inductively Coupled Plasma – Optical Emission Spectroscopy (ICP-OES)	35
3.3.3	Brunauer-Emmett-Teller Surface Area Analysis (BET)	36
3.4	Spectroscopic Characterization	37
3.4.1	X-ray Photoelectron Spectroscopy (XPS)	37
3.4.2	Raman Spectroscopy	37
3.5	Electrochemical Characterization	37
3.5.1	Rotating Disk Electrode (RDE) Measurement	37
3.5.2	Electrochemical Impedance Spectroscopy (EIS)	40
3.5.2.1	Ex-Situ EIS Measurement	40
3.5.2.2	In-Situ EIS Measurement	411
3.5.3	Cyclic Voltammetry (CV)	41
3.5.4	Electrochemical Long-Term Stability Experiments	43
3.5.5	Membrane Electrode Assembly Testing	43
<b>4.</b>	<b>Experimental</b>	<b>45</b>
4.1	Materials	45
4.2	Preparation Methods	46
4.2.1	Preparation of GF	46
4.2.2	Preparation of N-GF	46
4.2.3	Preparation of N-G and N-CNT	47
4.2.4	Chemical Preparation of Catalysts	47
4.2.5	Electrochemical Preparation of Catalysts	47
4.2.6	Preparation of MEAs	48

<b>5. Hierarchical Structured Multilayer Graphene Foams (GF) Coated with Nitrogen-Containing Carbon Layers (N-GF)</b>	<b>49</b>
5.1 Results	50
5.1.1 Chemical Composition of GF and N-GF	50
5.1.2 Morphology and Structure of GF and N-GF	52
5.1.3 Characterization of GF and N-GF	54
5.1.3.1 BET Characterization	54
5.1.3.2 XPS Characterization	55
5.1.3.3 XRD Characterization	58
5.1.3.4 Raman Spectroscopy Characterization	59
5.1.4 Characterization of Supported Pt Catalysts	61
5.1.5 Electrochemical Characterizaion of the Foam Structures	63
5.1.5.1 Electronic Conductivity of the GF and N-GF	63
5.1.5.2 Electrochemical Activity towards the ORR	64
5.1.5.3 Stability of the Catalysts	66
5.1.5.4 Polarization Curves on MEA	67
5.2 Discussion	70
<b>6. Different Carbon Morphologies Coated with Nitrogen-Containing Carbon Layers</b>	<b>71</b>
6.1 Results	72
6.1.1 Elemental Analysis	72
6.1.2 Morphology Characterization	73
6.1.3 Structure Characterization	76
6.1.4 Physical Characterization	77
6.1.4.1 BET Characterization	77
6.1.4.2 Raman Spectroscopy Characterization	78
6.1.4.3 XPS Characterization	80
6.1.5 Catalyst Characterization	82
6.1.5.1 SEM Analysis	82
6.1.5.2 TEM Analysis	83
6.1.5.3 XRD Analysis	84
6.1.6 ORR Activity	85
6.1.7 Conductivity Test	86
6.1.7.1 Ex-situ EIS with RED measurement	86
6.1.7.2 In-situ EIS in PEM fuel cell	87
6.1.7.3 A fuel cell performance of MEA	90

6.2	Discussion	94
<b>7.</b>	<b>Summary</b>	<b>95</b>
<b>8.</b>	<b>Outlook</b>	<b>97</b>
<b>9.</b>	<b>Appendix</b>	<b>98</b>
9.1	List of Figures	98
9.2	List of Tables	101
9.3	Acknowledgements	102
9.4	References	103
9.5	Publications	113
9.5.1	Journal Articles	113
9.5.2	Presentations	113
9.5.3	Posters	114
9.5.4	Awards	114

## List of abbreviation

Abbreviation	Description
AFC	Alkaline fuel cell
BET	Brunauer-Emmett-Teller surface area analysis
CCM	Catalyst coated membrane
CCS	Catalyst coated substrate
CE	Counter electrode
CNT	Carbon nanotube
CV	Cyclic voltage
CVD	Chemical vapour deposition
DMFC	Direct methanol fuel cell
ECSA	Electrochemically active surface area
EDX	Energy dispersive X-ray spectroscopy
EG	Ethylene glycol
EIS	Electrochemical impedance spectroscopy
FWHM	Full width at half maximum
GC	Glassy carbon
GDE	Gas diffusion electrode
GDL	Gas diffusion layer
HDA	Hydrogen depolarized anode
ICP-OES	Inductively coupled plasma – optical emission spectroscopy
IL	Ionic liquid
MCFC	Molten carbonate fuel cell
MEA	Membrane electrode assembly
MPL	Microporous layer
OCV	Open circuit voltage
ORR	Oxygen reduction reaction
PAFC	Phosphoric acid fuel cell
PEMFC	Polymer electrolyte membrane fuel cell
PFSA	Perfluorated sulfonic acid
PTFE	Polytetrafluorethylen
RDE	Rotating disk electrode
RE	Reference electrode
SEM	Scanning electron microscopy
SOFC	Solid oxide fuel cell
TEM	Transmission electron microscopy
TPB	Triple phase boundary
WE	Working electrode
XPS	X-Ray photoelectron spectroscopy
XRD	X-ray diffraction

# 1. Introduction

The world's ever increasing energy requirement, continuous and rapid depletion of fossil fuels along with alarming increase in the concentration of greenhouse gases have directed large scale research into the development of alternative and green energy sources. Consequently, fuel cells which have very low or no emission of harmful greenhouse gases (e.g. CO<sub>2</sub>, NO<sub>x</sub>, SO<sub>x</sub>, etc.), have generated a lot of interest in the scientific and engineering communities [1–5]. Today, fuel cells are widely considered to be efficient and non-polluting power sources offering much higher energy densities and energy efficiencies compared to conventional systems. A fuel cell is an electrochemical device that converts the chemical energy of a fuel (e.g. hydrogen, methanol, etc.) and an oxidant (air or pure oxygen) in the presence of a catalyst into electricity, heat and water.

The main objective in fuel cell technologies is to develop low cost, high performance and durable materials. Another important issue in fuel cell technology is to develop efficient catalysts for the ORR. In this regard, Pt has been regarded as the best catalyst for the ORR in fuel cell applications, however the Pt-based electrode limits the practical use of fuel cell applications because of the global scarcity of Pt and its high cost [6-9]. Many efforts are made to replace cost intensive Pt-based electrodes or minimize the amount of Pt by increasing the efficiency of the catalyst [10], and by optimization of the catalyst structure and/or morphology and conductivity of the catalyst support. It is well known that supported metal catalysts show improved stability and higher activity compared to unsupported bulk metal catalysts. Surface area, porosity, electrical conductivity, electrochemical stability and surface functional groups characterise a support.

Most recent catalyst support research has focused on 2D graphene-like structures which consist of several carbon monolayers. For catalytical purpose the extended flat structure of 2D carbon systems and the possibility of a chemical surface modification lead to potential catalyst support applications. These properties decrease the catalyst agglomeration and therefore the performance is increased [11], for example, these high surface carbon species were used for energy storage applications in supercapacitor devices. Thus, the search for promising alternative catalysts has attracted numerous research efforts, and has led to the discoveries of unique materials, including microporous carbon-supported iron-based catalysts [12, 13], nanostructured manganese oxides [14], and metal-free N-doped carbon materials [15-21]. Among them, N-doped carbon materials show promising properties due to their high catalytic activity, excellent reliability, and environmental compatibility [15-21]. N-doped graphene has drawn special attention recently, largely due to the intriguing properties of graphene such as the high surface area and remarkable electronic conductivity.

To incorporate N-atoms into a multilayer graphene lattice, various methods have been developed, including chemical vapor deposition [16, 22], thermally annealing of multilayer graphene or graphene oxide (GO) with ammonia (NH<sub>3</sub>) [18, 23], arc discharge of graphite with pyridine/NH<sub>3</sub> [24],

and nitrogen plasma treatment of multilayer graphene [25, 26]. However, the applicability of these approaches is limited severely by the high costs, scale-up problems, and the use of a complex instrumentation or toxic precursors. Recently, using melamine and urea as nitrogen-sources, a high doping level of 7 to 8 at% has been achieved but for technical applications large amounts of N-doped multilayer graphene are required [27].

Recently, there have been many efforts on controlling the carbon-based composite nanostructures with heteroatom doping as well as specific surface area to improve the electrochemical activity for the fuel cell reactions. N-doped 3D porous structures like foams [27], aerogels [28-30], sponges [31, 32], hydrogels [33], and networks [34, 35] could provide a better solution for the issue of mass transport problems in PEMFC. Guo et al. [36-38] prepared N-doped hierarchical porous carbon foams by pyrolyzing nitrogen-enriched conductive polymers. They demonstrated that heteroatom doped carbon materials exhibit a nitrogen content of 0.31 to 1.77 at% and an efficient catalytic activity for ORR. Also, a fabrication of graphene/CNT structures with nitrogen can efficiently prevent the face-to-face orientation of graphene, and strongly distribute the anchoring sites for immobilized metal catalyst supports. The performance of these composites results in stability and high catalytic activity. For a further increase of the electronic conductivity and/or electrochemical stability which was necessary for technical applications a higher degree of nitrogen doping is required. Therefore, a state-of-the art architecture of nitrogen doped porous carbon materials with macro-, meso- and/or micropores is a big challenge today.

In the present thesis a low-cost, scalable, synthesis method for preparing a hierarchical structured porous carbon material is reported consisting of nitrogen-coated carbon layers. A special structure of the new catalyst support was produced by an optimized thermal decomposition of sodium ethoxide (NaOEt). Further, an increased conductivity by nitrogen coating of carbon combined with a hierarchical structure was achieved by surface modification with an ionic liquid. The surface modification is responsible for a significantly enhanced catalytic efficiency and therefore improved electrochemical performance. For this reason the application of these materials as a catalyst support for PEMFC applications is proposed.

## **2. Scientific / Technological Background**

### **2.1 Fuel Cells in General**

The current movement towards environmentally friendlier and more efficient power production has caused an increased interest in alternative fuel and power sources. Within the last decade fuel cells have been extensively studied for commercial use. The reliance upon the combustion of fossil fuels has resulted in severe air pollution, and extensive mining of the world's oil resources. In addition to being hazardous to the health of many species (including our own), the pollution is indirectly causing the atmosphere of the world to change (global warming). In addition to health and environmental concerns, the world's fossil fuel reserves are decreasing day by day. The world needs a power source that has low pollutant emissions, is energy efficient, and has an unlimited supply of fuel for a growing world population. Fuel cells have been identified as one of the most promising technologies to accomplish these goals. Many other alternative energy technologies, including solar, wind, hydroelectric power, bioenergy, geothermal energy, and so on, have been researched and developed. Each of these alternative energy resources have their advantages and disadvantages, and are in varying stage of development. In addition most of these energy technologies cannot be used for transportation or portable electronics. Other portable power technologies, such as batteries and supercapacitors, also are not suitable for transportation technologies, military applications, and the long term need for future applications remains a challenge. The ideal option for a wide variety of applications is using a hydrogen fuel cell combined with solar or hydroelectric power. Compared to other fuels, hydrogen does not produce carbon monoxide or other pollutants. When the fuel is hydrogen the only by-products are pure water and heat. Fossil fuels are limited in supply, and are located in selected regions throughout the world. The limited supply and large demand drives up the cost of fossil fuels tremendously. The end of low cost is rapidly approaching. Other types of alternative technology such as fuel cells can last indefinitely when non-fossil fuel based hydrogen are used. The 19th Century was the century of the steam engine and the 20th Century was the century of the internal combustion engine; it is likely that the 21st Century will be the century of the fuel cell [39]. Full cells are now on the road of being introduced commercially, revolutionizing the way we presently produce power. Fuel cells can use hydrogen as a fuel, offering the prospect of supplying the world with clean, sustainable electrical power [39].

### **2.2 Types of Fuel Cells**

A fuel cell is an electrochemical cell that converts chemical energy from fuel into electric energy in a constant temperature process. Electricity is generated from the reaction between a fuel supply

and an oxidizing agent. The reactants flow into the cell, and the reaction products flow out of it, while the electrolyte remains within it. Fuel cells can operate continuously using wide a range of fuels, including hydrogen, as long as the necessary reactant and oxidant flows are maintained. They are made up of three segments which are sandwiched together: the anode, the electrolyte, and the cathode. At the anode a catalyst oxidizes the fuel, usually hydrogen, turning the fuel into a positively charged ion and a negatively charged electron. At the cathode, a catalyst turns the ions into the waste chemicals such as water or carbon dioxide.

There are six main types of fuel cells [40–45] as listed below (Table 2.1). The lower temperature systems including alkaline fuel cell (AFC), PEMFC, direct methanol fuel cell (DMFC) and phosphoric acid fuel cell (PAFC), operate essentially on H<sub>2</sub> fuel, whereas the higher temperature systems, including molten carbonate fuel cell (MCFC) and solid oxide fuel cell (SOFC), can also electrochemically oxidize CO. Using of the higher temperature systems is advantageous when a hydrocarbon fuel is supplied to the fuel cell. For reasons of electrode activity, which translates into higher efficiency and greater fuel flexibility, higher temperature operation is preferred. However, for portable power applications, lower temperature operation is typically favored as it enables rapid start-up and minimizes stress due to thermal cycling. In addition, solid electrolyte systems can avoid the need to contain corrosive liquids, thus solid oxide and polymer electrolyte fuel cells are preferred by many developers comparing to alkali, phosphoric acid, or molten carbonate fuel cells. Table 2.1 represents the individual types of fuel cells, operating parameters, and the employed electrolytes (modified from the 5th edition of the Fuel Cell Handbook, U.S. Department of Energy, 2000). The remainder of this section goes into a more detailed account of the main types of fuel cells.

**Table 2.1** Different types of fuel cells and characteristics [46].

Fuel Cell Typ	T <sub>op</sub> , °C	Fuel gas / Oxidant	Anode	Electrolyte, Ion	Cathode	Theoretical / Electrical / CHP (Combined Heat and Power) Efficiency (%)
AFC	LT 60–90	H <sub>2</sub> /O <sub>2</sub> (high purity)	H <sub>2</sub> + 2OH <sup>-</sup> → 2H <sub>2</sub> O + 2e <sup>-</sup>	KOH, OH <sup>-</sup>	1/2O <sub>2</sub> + H <sub>2</sub> O + 2e <sup>-</sup> → 2OH <sup>-</sup>	Theoretical: 83, Electrical: 45-60, CHP: >80
PEMFC	LT 60–90	H <sub>2</sub> /O <sub>2</sub> , Air	H <sub>2</sub> → 2H <sup>+</sup> + 2e <sup>-</sup>	Nafion <sup>®</sup> , H <sup>+</sup>	2H <sup>+</sup> + 1/2O <sub>2</sub> + 2e <sup>-</sup> → H <sub>2</sub> O	Theoretical: 83, Electrical: 40–45, CHP: 70-90
DMFC	LT 80–130	CH <sub>3</sub> OH/O <sub>2</sub> , Air	CH <sub>3</sub> OH + + H <sub>2</sub> O → CO <sub>2</sub> + 6H <sup>+</sup> + 6e <sup>-</sup>	Nafion <sup>®</sup> , H <sup>+</sup>	3/2O <sub>2</sub> + 6H <sup>+</sup> + 6e <sup>-</sup> → 3H <sub>2</sub> O	Theoretical: 97, Electrical: 40-60, CHP: 85
PAFC	MT 140–200	H <sub>2</sub> /O <sub>2</sub> , Air	H <sub>2</sub> + → 2H <sup>+</sup> + 2e <sup>-</sup>	H <sup>+</sup> , H <sub>3</sub> PO <sub>4</sub>	2H <sup>+</sup> + 1/2O <sub>2</sub> + 2e <sup>-</sup> → H <sub>2</sub> O	Theoretical: 80 , Electrical: 40–45, CHP: >85
MCFC	HT 650–700	H <sub>2</sub> /CO <sub>2</sub> , Coal gas/ Air	H <sub>2</sub> + CO <sub>3</sub> <sup>2-</sup> → H <sub>2</sub> O + CO <sub>2</sub> + 2e <sup>-</sup>	Li <sub>2</sub> CO <sub>3</sub> , K <sub>2</sub> CO <sub>3</sub> , CO <sub>3</sub> <sup>2-</sup>	1/2O <sub>2</sub> + CO <sub>2</sub> + 2e <sup>-</sup> → CO <sub>3</sub> <sup>2-</sup>	Theoretical: 78, Electrical: 45-55, CHP: >80
SOFC	HT 800–1000	Natural gas/ Air, Coal gas/ Air	H <sub>2</sub> + O <sup>2-</sup> → H <sub>2</sub> O + 2e <sup>-</sup>	ZrO <sub>2</sub> /YO <sub>3</sub> , O <sup>2-</sup>	1/2O <sub>2</sub> + 2e <sup>-</sup> → → O <sup>2-</sup>	Theoretical: 73, Electrical: 40–50, CHP: <90

Among the various types of fuel cells, PEMFC is currently leading the commercial front for its advantages such as low temperature operation, quick startup time and dynamic operation capabilities. Significant advancements in fundamental, engineering and technological aspects have been achieved for PEMFC, leading to a wide range of portable, automotive and stationary applications.

Cost and durability of PEMFC are the two major challenges that need to be addressed to facilitate their commercialization. The properties of the membrane electrode assembly (MEA) have a direct impact on both durability of a PEMFC. The success of the MEA and thereby PEMFC technology is believed to depend largely on the electro-catalysis. The next chapters are devoted to the key components of the PEMFC, the MEA.

## **2.3 PEM Fuel Cell**

PEMFC has drawn the most attention because of its simplicity, viability, quick start up that made it suitable for several applications. The polymer electrolyte membrane fuel cells are capable of generating electricity with high power density and high efficiency, approximately 50 % and more than 80 % if the produced heat is considered in the application as well. The heart of the PEMFC technology is the polymer membrane used as electrolyte. This particular kind of membrane is capable of allowing only the transit of protons. The electrolyte layer plays a key role in the operating of a fuel cell. As stated above the task of the electrolyte is to allow the transit of ions from one electrode to the other, but it must also avoid the passage of free electrons or other substances. Typically, PEMFC operate at low temperature (60 ~ 80 °C) allowing a faster start up than high temperature fuel cells and also making problems like sealing, assembly and handling less complex. The main issue in the operation of a PEM fuel cell is water management. The electrolyte needs a certain degree of humidification to allow the ion conduction through itself, and to avoid its dehydration or the flooding phenomenon. A correct management of the humidification of the inflows is necessary.

### **2.3.1 Basic Structure and Operation**

Like every type of fuel cell the main structure of a PEMFC includes the electrolyte, two electrodes and an external circuit with the load. The electrolyte membrane (usually Nafion<sup>®</sup>) is squeezed between the two porous and electrically conductive electrodes. These electrodes are typically manufactured from carbon cloth or carbon fiber paper. Both electrodes present a layer with catalyst particles at the electrodes/electrolyte interface, typically platinum supported on carbon. The layer of

the electrodes with the catalyst is called the catalyst layer, while the layer without the catalyst is called the backing layer or diffusion layer. The layer has the aim of giving mechanical support at the fuel cell structure allowing the diffusion of reactants towards the electro-catalyst. The catalyst layer and membrane combination is called MEA. A basic schematic illustration of a PEMFC is shown in Figure 2.1.

The MEA is then sandwiched between two plates, usually made of graphite. These plates, called flow field plate (FFP) are to provide the pathways for the reactant gases in order to allow their good distribution over the surface of the electrode. The plates also have to guarantee electric connection with the electrodes given that the current collector plates are located on the other side. In a fuel cell stack, the connection is made by bipolar plates, which are capable of electrically connecting adjacent cells. Moreover, this plate is capable of managing both the flow of the fuel on the anode side and the flow of the oxidant on the cathode side and, at the same time, avoiding that they mix together. During the operation, hydrogen gas flows through the bipolar plates to the anode, the hydrogen is split at the anode into protons and electrons. The electrons flow through the anode to the electric circuit while the protons flow through the electrolyte membrane to the cathode. The electrons move to the cathode, and then the protons, oxygen, and electrons combine to form water at the cathode.

The following overall reaction occurs as follows (Eq. 2.1):

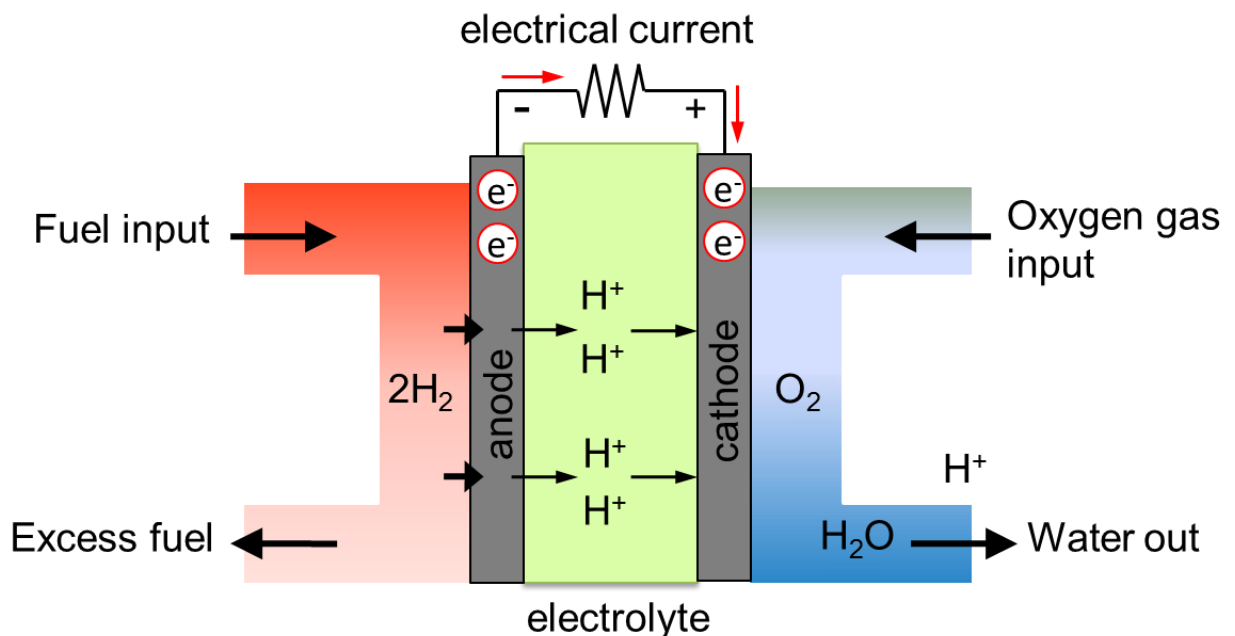


**Figure 2.1** Schematic illustration of PEMFC.



The electrochemical performance of fuel cells is typically characterized in terms of the voltage-current relationship, also known as the polarization curve. It is important to emphasize that the polarization curve of a fuel cell is a net or global effect of numerous transport (electron and ion conduction, chemical species diffusion/convection, mass convection) and electrochemical reactions, ORR and hydrogen evolution reaction (HER).

The reaction products of the individual electrode reactions are constituents of the aqueous electrolyte, which avoids polarization losses in the electrolyte.

Each of the two electrode reactions creates a characteristic potential difference across the interface solid electrode/electrolyte. The overall cell voltage between the two electrodes, which are joined by the same electrolyte, allows the electrons generated at the anode (HER) and consumed at the cathode (ORR) to create work in the external circuit. Therefore, chemical energy is released by the individual electrode reactions, locally separated in contrast to the combustion step in the thermomechanical power generation.

### 2.3.2 Polarization Curve Losses

Generally, the available cell voltage of electrochemical cells depends on the thermodynamics of the two electrode reactions in the electrolyte. According to the individual electrode potentials of the  $\text{H}_2/\text{H}^+$  reaction and the  $\text{O}_2/\text{H}_2\text{O}$  reaction, a cell with  $\text{H}_2$  and  $\text{O}_2$  as reactants should yield an ideal cell voltage of 1.23 V at standard conditions ( $T= 25\text{ }^\circ\text{C}$ ,  $P= 1\text{ bar}$ ). In practice, a lower value in the range of 1 V is observed due to different implications such as side reactions, depolarization of electrodes caused by crossover of gases through the electrolyte.

PEMFC polarization curve losses can be divided into three areas, which can have a significant impact in specific regions and/or throughout the polarization curve: Activation losses (kinetic effects at the electrode surfaces); Ohmic losses of the overall system (mainly due to membrane resistance); and mass transport limitations.

**1) Activation loss:** This loss is related to the electrochemical kinetics of the half-cell reactions and their effects are more dominant at lower current densities. The origin of the loss is in the requirement to alter the electrical potential difference at the electrode-electrolyte interface from its

equilibrium level to drive the electrochemical reactions. In PEMFC the activation loss are typically due to slow ORR kinetics at the cathode.

**2) Ohmic loss:** The ohmic loss arises due to the resistances of electron transport in the electrodes (gas diffusion layer and the catalyst layer) and the bipolar plates as well as the transport of ions in the electrolyte. The ohmic loss has linear relationship to the current density. This loss increases steadily with an increase in current density. Thus, as a result of the linear profile of the polarization curve in the intermediate current densities, it is commonly stated that ohmic loss dominates in this current density range.

**3) Mass transport loss:** The mass transport loss arises from the fact that the reactant cannot be supplied to the catalytic sites at sufficient rate resulting in reactant concentration at catalyst sites being significantly lower than the bulk or supplied reactant concentration. The low concentration translates into the requirement of higher activation overpotential to compensate for the lowering of reaction rate due to reduced concentration.

Every overvoltage can be expressed as a function of current produced by the fuel cell (Eq. 2.2), and in particular is common to use the current density instead of the total current. Figure 2.2 shows the typical shape of a polarization curve as well as the three different regions where the three different main overvoltages are dominant. Therefore, for a certain values of temperature and pressure, it is possible to write the real voltage delivered by the fuel cell:

$$E = E_{eq} - E_L - \eta_{act} - \eta_{iR} - \eta_{diff} \quad \text{Eq. 2.2}$$

$E$  - cell voltage / V

$E_{eq}$  - equilibrium potential (or theoretical OCV) / V

$E_L$  - loss in voltage due to leaks across the electrolyte

$\eta_{act}$  - activation overpotential due to slow electrode reactions

$\eta_{iR}$  - overpotential due to ohmic resistances in the cell

$\eta_{diff}$  - overpotential due to mass diffusion limitations

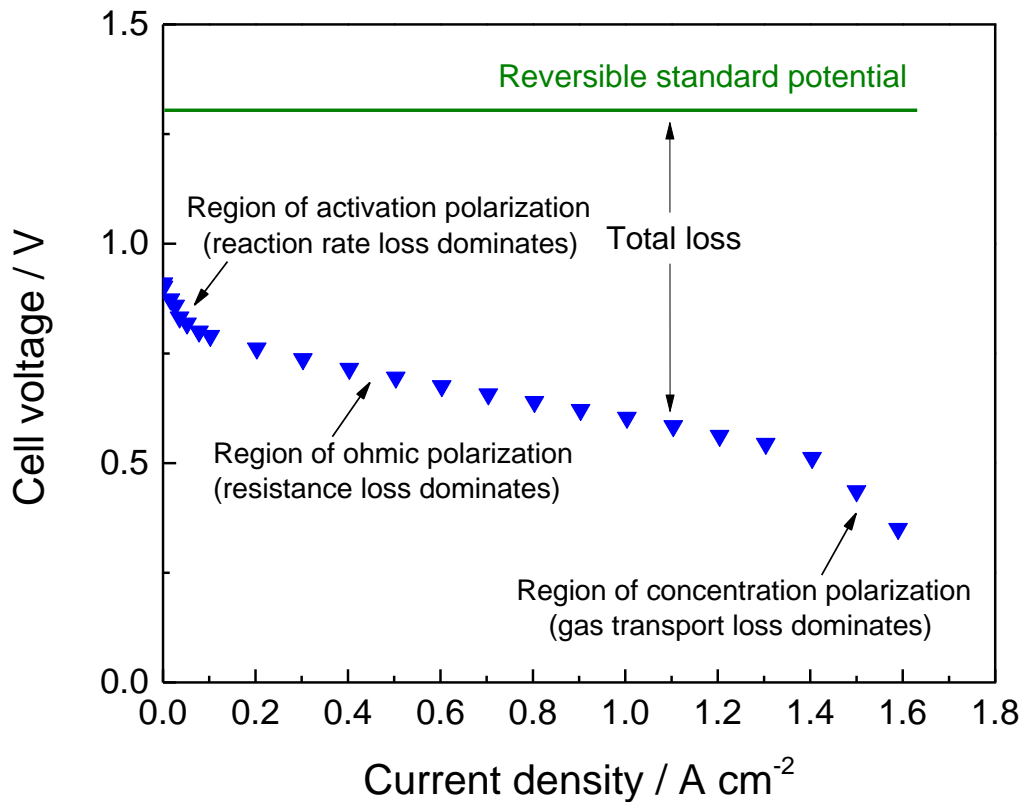


**Figure 2.2** Typical fuel cell polarization curve with labeled regions of loss. Polarization curves of Pt/C catalyst ( $0.4 \text{ mg cm}^{-2}$  Pt loading) with 15 wt% Nafion and 5 wt% PTFE solution performed operating at  $80 \text{ }^\circ\text{C}$  and 95 % relative humidity.

The various losses are obviously affected by the operating conditions (temperature, composition, relative humidity, and pressure). Therefore, there are several approaches to reduce or limit the internal current losses: 1) Providing a gold or zirconium alloy diffusion barrier between reactant and electro-catalyst layer; 2) Use of high ionic conductivity of an electrolyte; 3) Choosing porosity and structure of the electrode material. The ideal electrode must transport gaseous/or liquid species, ions, and electrons and the electrocatalysts at triplepoint boundaries must rapidly catalyze electro-oxidation (anode) or electro-reduction (cathode). The promising electrodes which have a porous, electronically and ionically conducting, electrochemically active material are presented in more details in Chapter 5.

### 2.3.3 Component of PEMFC

The main research area for improving the fuel cell is the MEA. The components of a PEMFC MEA are two GDLs, two catalyst layers (anode and cathode) and a membrane as shown in Figure 2.3. The GDL materials mostly origin from carbon cloth or carbon paper impregnated/or sprayed with Teflon. The GDL is placed between catalyst layer and bipolar plate. The electrochemical reactions in the anode and the cathode are effected on the electro-catalyst platinum which is supported on carbon. The anode and cathode layers are also porous to allow for reactant transport as well contain a certain amount of ionomer to allow for the transport of protons generated/consumed in the electrochemical reactions. The most commonly employed electrolyte for PEMFC is Nafion<sup>®</sup> produced by DuPont, which is a short-side-chain perfluorosulfonic ionomer (PFSI). The electrons generated/consumed in the anode/cathode catalyst layer are conducted through the adjacent GDL which is typically a porous carbon paper.

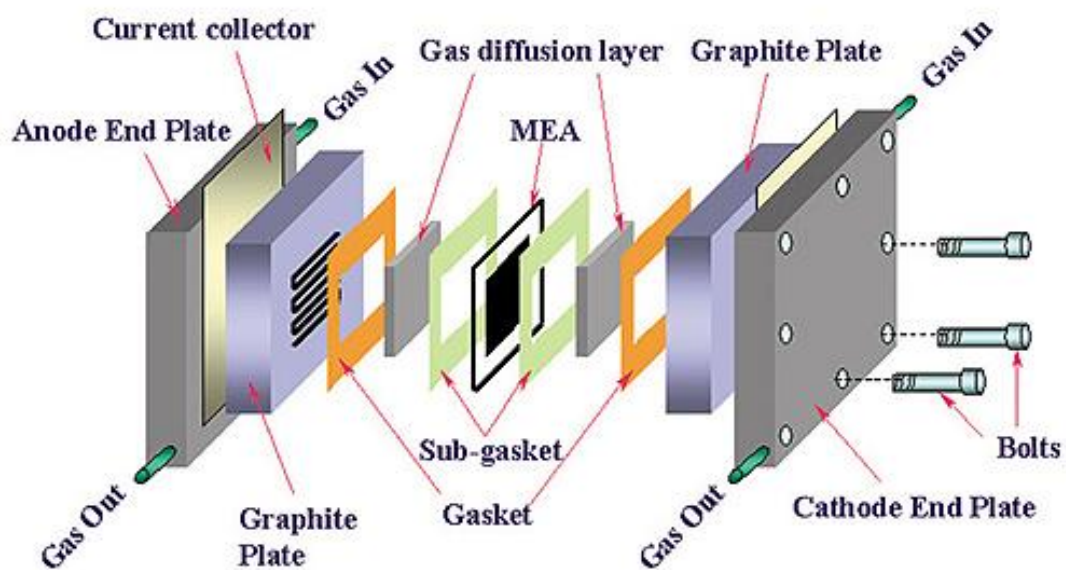


**Figure 2.3** Fuel-cell components [47].

Protons, electrons, and gases are often referred to as the triple phase boundary (TPB) found in a catalyst layer. The transport of gases, charged species and water can be better understood by taking a closer look at the electrode structure. Therefore, the optimization of an electrode design is the attempt to distribute the TPB for reducing transport losses in the catalyst layer. For this reason the desired electrode and their functionality is introduced in more details in the next part.

### 2.3.3.1 Membrane

Advances in the electrochemical conversion of water to and from hydrogen and oxygen have principally been achieved through the development of new materials and by understanding the mechanisms of the degradation of PEMFC during operation. Electrochemical conversion of hydrogen and oxygen into water in fuel cells relies on a proton exchange membrane (PEM). The PEMs form the heart of the electrochemical cells, where they ensure conduction of protons from the anode to the cathode, separation of reactant (fuel cell) or product (electrolyser) gases, and electronic insulation of the electrodes. Many of the requirements for effective PEMs in fuel cells and electrolysers are the same and have long been recognized. However, it is only recently that notable advancements have been made to enable chemically and mechanically stable membranes with high proton conductivity. An extensive library of polymers and ionomers has been developed and evaluated in recent years. This has led to a vast number of novel sulfonic acid functionalized non-fluorinated polyaromatics and polymer materials comprising protogenic functions other than sulfonic acid (typically phosphonic and heterocycle functionalized materials). These efforts have also remarkably advanced perfluorosulfonic acid (PFSA) polymer technologies to produce a new generation of state-of-the-art fuel cell membranes.

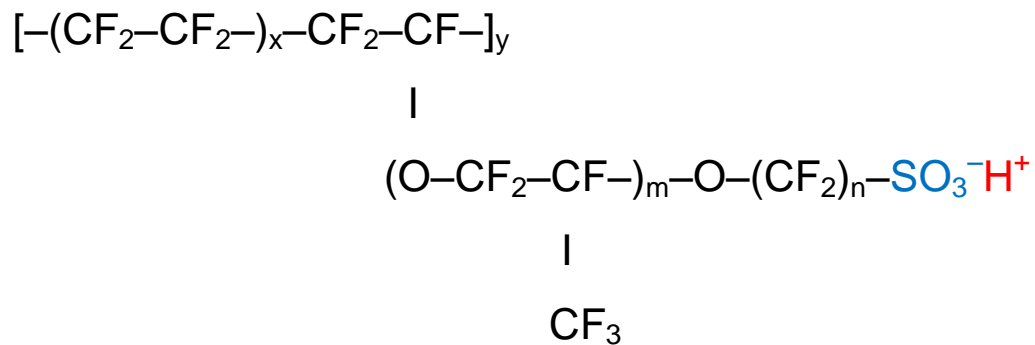
Nafion<sup>®</sup>, developed by DuPont, is generated by free radical initiated copolymerization of a perfluorinated vinyl ether sulfonyl fluoride co-monomer with tetrafluoroethylene (TFE). The polytetrafluoroethylene (Teflon<sup>®</sup>)-like molecular backbone gives its mechanical and chemical stability, while the sulfonic acid functional groups ( $-\text{SO}_3^-\text{H}^+$ ) provides charge sites for proton transport. Nafion<sup>®</sup> polymer chains aggregate and create voids and channels with walls covered by sulfonic acid functional groups. Within the overall structure of the membrane the end of the side chain ( $\text{SO}_3\text{H}$  group) tends to cluster. Although the Teflon<sup>®</sup>-like backbone is highly hydrophobic, the sulphonic acid at the end of the side chain is highly hydrophilic. The hydrophilic regions are created around the clusters of sulphonated side chains. Therefore this kind of material absorbs relatively large amounts of water (up to 50%).  $\text{H}^+$  ions movement in well hydrated region makes these materials proton conducting.

Perfluorinated ionomer membranes like Flemion<sup>®</sup> (Asahi Glass Company), Aciplex<sup>®</sup> (Asahi Kasei), and Fumion<sup>®</sup> F (FuMA-Tech) were also produced. Compared to other membranes the Nafion<sup>®</sup> membranes exhibit a good proton conductivity, a small tendency to swell in water and in low relative humidity. The desired properties of a membrane must meet the following requirements to operate properly in a fuel cell:

- High ionic conductivity
- Present an adequate barrier to the reactants

- Good chemical, mechanical and electrochemical stability in fuel cell operating conditions
- Low electronic conductivity
- Ease of manufacturability/availability
- Low cost

The long-side-chain membranes typically comprise an ionomer of equivalent weight 1,100–900 g/mole or ion exchange capacity of 0.91–1.11 mmole/g [48].



Flemion <sup>®</sup> :	m = 0, 1; n = 1 - 5
Aciplex <sup>®</sup> :	m = 1; n = 2; x = 6 - 8; y = 0, 1
DowMembrane <sup>®</sup> :	m = 0; n = 2 - 5; x = 3 - 10; y = 1
Nafion <sup>®</sup> :	m = 1; n = 2 - 5; x = 5 - 13; y = 1000

**Figure 2.4** Chemical structure of perfluorinated sulfonic acid ionomer.

### 2.3.3.2 Catalyst Layer

The catalyst layer is a porous composite of complex microstructure that is made of platinum, carbon, ionomer, and polytetrafluoroethylene (PTFE). The catalyst layer also contains open pores. The resulting catalyst layers are usually 5-20 μm thickness (depending on the Pt loading), comprising a large amount of meso- and macro-pores (5-100 nm), which are self-assembled during the electrode fabrication process.

An ideal catalyst layer should have properties as follows:

- A large interface area between gas phases and/or polymer electrode and catalyst

- Highly efficient proton transport
- High transportation capacity for oxygen and easy by-product removal
- High electronic conductivity
- Excellent chemical resistance and good mechanical properties to maintain an effective porous structure during fuel cell operation
- High tolerance to contamination.

### 2.3.3.3 Gas Diffusion Layer

The main function of the GDL is to diffuse the gas. The porous nature of the backing material facilitates the effective diffusion of each reactant gas to the catalyst on the MEA. The GDL is also an electrical connection between the carbon-supported catalyst and the bipolar plate or other current collectors. The GDL is usually made of a carbon-based porous substrate, such as carbon paper or carbon cloth, with a thickness of about 100 - 400  $\mu\text{m}$  and a dual-layer structure. The main function of GDL includes the following:

- A gas diffusion pathway from flow channels to the catalyst layer
- Help to remove by-produced water outside of the catalyst layer and prevent flooding
- Keep some water on the surface for conductivity through the membrane
- Heat transfer during cell operation
- Help to provide enough mechanical strength to hold the MEA from extension caused by water absorption.

The presented GDL in Figure 6 is typically wet-proofed with polytetrafluorethylene (PTFE) coating to ensure that the pores of the GDL do not become congested with liquid water. Production of an effective GDL is largely a matter of controlling the structure and porosity of the material. The vital role of GDL porosity in determining fuel cell performance has been studied by Chu et al. [49]. They found that it is important to consider the GDL as having a non-uniformly dispersed porosity, owing to the varying water content within the structure. As a consequence, graded porosity of the GDL both in the thickness and laterally across the layer is expected to improve performance by assisting water removal and access of gas when reactant becomes depleted in the flow channel. Increased porosity was found to have little benefit when operating at low current densities but has a considerable effect when operating at high load.

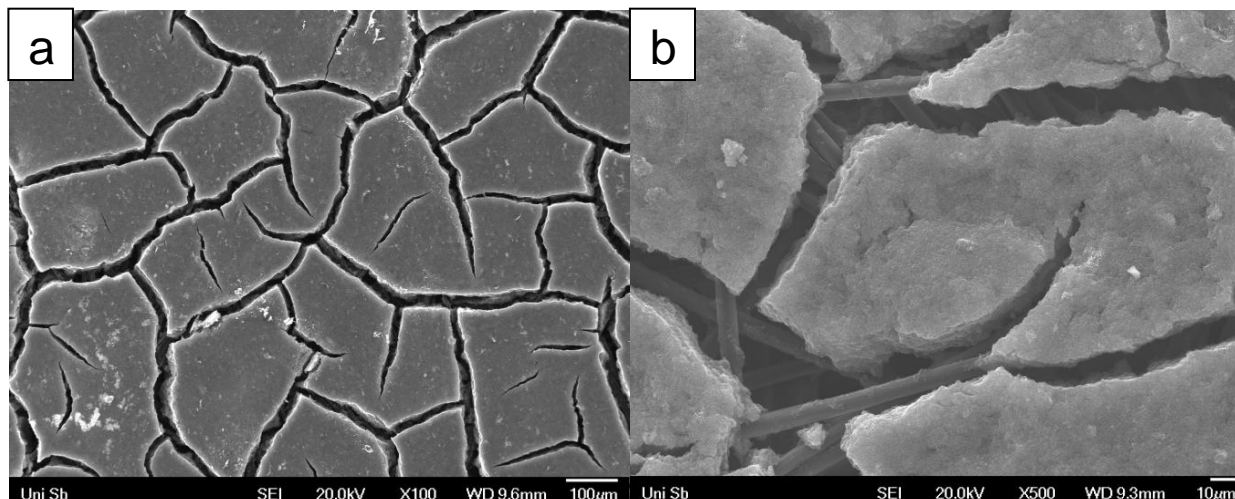


**Figure 2.5** SEM images of gas diffusion layer morphology.

An ideal GDL is required to effectively transport the gas reactants to the catalyst layers which have a low electronic resistance, a good electronic contacting surface and proper hydrophobicity for each application. In particular, for the highest power output when the fuel cell is operated at a relatively high current density, a higher flux of gas feed is needed, which requires the ideal GDL to effectively transport reactant gases to the catalyst surfaces at a high rate.

### 2.3.3.4 Membrane Electrode Assembly

MEA, as termed, is the assembly of the membrane and electrodes. As all the reactions within the fuel cell occur in the MEA, it is widely referred as the heart of the fuel cell. The MEA consists of a PEM, catalyst layers and GDL. Generally, the approaches taken to produce MEA can be divided into two general modes:

- (1) Catalyst coated membrane (CCM), which is to directly apply the catalyst layer to the membrane, followed by GDL addition
- (2) Catalyst coated substrate (CCS), which is the application of the catalyst layer to the GDL.

For the preparation of the MEA, the catalyst ink is firstly a mixture made of ionomer, supported catalyst and a solvent. The catalyst layer is formed by either coating the catalyst ink to the membrane or onto the GDL. After then, catalyst layer with minimized catalyst loading is prepared by impregnation reduction, dry spraying, catalyst powder deposition, electrodeposition, sputtering and pulsed laser deposition. The final GDEs are fabricated using hot pressing. The design and fabrication method of MEA is highly critical as it directly affects performance of the PEMFC. In the experimental section (Chapter 4) we will look at the methods used for assembling the membranes and electrodes and the methods studied to apply the catalyst layer.

### 2.3.3.5 Bipolar Plates

Bipolar plates (BPP) supply the reactant gases through the flow channels to the electrodes and serve the purpose of electrically connecting one cell to another in the electrochemical cell stack. These plates also provide structural support for the thin and mechanically weak MEAs and are means to facilitate water management as well as heat management within the cell [50-52]. An ideal material for BPPs should possess the properties of good electrical conductivity, high corrosion resistance, high mechanical strength, light weight and low cost etc. [53, 54]. Conventionally, graphite and graphite composite plates have been applied to machine BPPs due to their low interfacial contact resistance and high corrosion resistance. Presently, the design and manufacturing of metallic BPPs and the performance have achieved a mass production of very thin BPP, increasing the volumetric power density of the fuel cell stack, as well as lowering manufacturing costs.

Product water removal at the cathode is even more complex as this represents a two-phase flow problem. While some turbulence may help to release water from the open gas diffusion layer structure, opening up room for gas access, turbulent gas flow leads to larger pressure drops between flow field inlet and outlet. Pressure differentials require compression energy to drive the reactants through the flow field structure, and this has an impact on the system efficiency. Therefore, flow field designs to improve the fuel cell performance have been widely studied using serpentine, parallel, and interdigitated flow channels as indicated in Figure 2.6.

(1) Serpentine: This is a long continuous flow path from the start (inlet) to the end (outlet) of the channel and as the name suggests, it is in a serpentine path configuration. This flow-field type is characterized by a long flow path and subject to high pressure drop. As shown in Figure 1.6a, serpentine flow field channels are associated with the concentration gradient due to reactant depletion as it traverses the length of the channel. An advantage of the serpentine flow path is that any obstruction in the path, such as a water droplet, will not block all activity downstream of the obstruction. In an obstructed serpentine channel, the reactant gas is forced to bypass the channel by flowing under the current collecting rib, through the porous backing layer, and emerges in an adjacent channel. The bypass flow can then diffuse back toward the location of the obstruction, so that the net effect of the obstruction will be an increased pressure drop, but no loss of active area [55].

(2) Parallel: This is a manifold-like configuration where straight parallel channels are connected to inlet and outlet channels (Figure 2.6b). Unsteady voltages do occur after extended period of operation because of cathode gas flow distribution and water management [56]. Continuous operation results in water build up in the bottom and downward sides of the channel. A

disadvantage of this occurrence is that the reactants will flow through the path with least resistance thus there will be inactive sites within the cell. Also, cells near the manifold inlet tend to be more active than cells at the far end of the manifold resulting in pressure loss in the manifold and channel length.

(3) Interdigitated: The reactant flow for this design is parallel to the electrode surface. As shown in Figure 2.6c, the channels are interdigitated such that they are dead ended thus forcing the reactant to flow under pressure through the porous reactant layer to reach the flow channels connected to the stack manifold. Structures of the interdigitated type suggest that the channels are no longer continuous, but the gas is forced to flow through some part of the gas diffusion layer. This structure helps to induce forced water removal from the open structure of the gas diffusion layer but induces higher pressure drops between inlet and outlet than through-flow options do [55].

(4) Pin: As shown in Figure 2.6d, this flow field consists of an array of cubical or circular pins protruding from the surface of the flow field plate. A groove like section is created between pins and reactants flow through and around the groove in direction of pressure gradient. The limitation of this design is that there are multiple flow paths, hence the flow of reactants is determined by the path with least resistance. Also, reactant concentration may be depleted in the stable recirculation zones and consequently decrease the cell and/or stack performance [56].

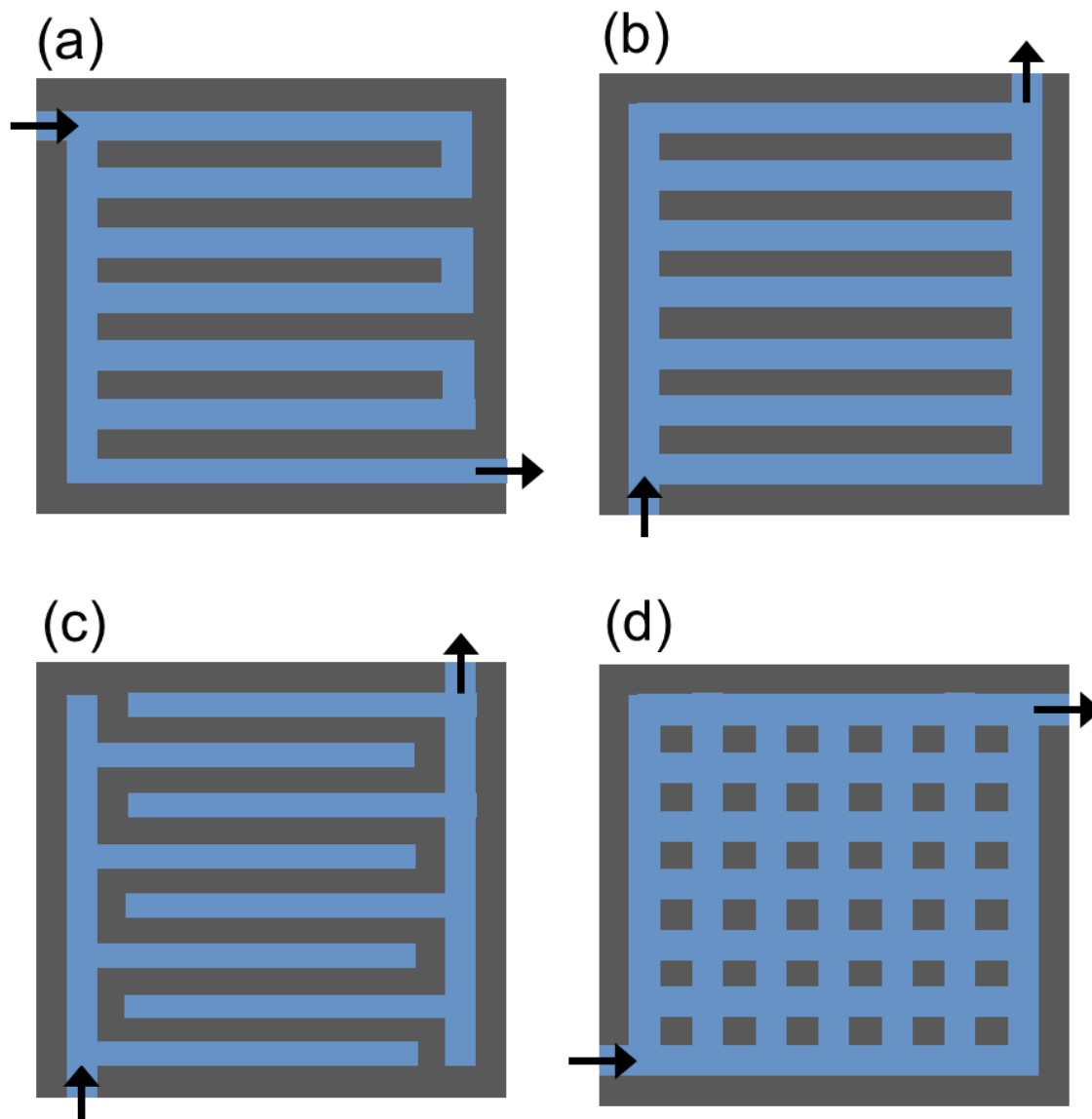


**Figure 2.6** Typical flow channels designs; (a) Serpentine, (b) Parallel, (c) Interdigitated, (d) Pin.

### 2.3.3.6 Electrode

A fuel cell electrode is essentially a thin catalyst layer pressed between membrane and porous, electrically conductive substrate. There are three kinds of species that participate in the electrochemical reactions, namely gases, electrons and protons, the reactions can take place on a portion of the catalyst surface. Electrons travel through electrically conductive solids including the catalyst itself. But it is important that the catalyst particles must be electrically connected to the substrate. Protons travel through the ionomer, and therefore the catalyst must be in intimate contact with the ionomer. And finally, the reactant gases travel only through voids and therefore the

electrode must be porous to allow gases to travel to the reaction sites. At the same time, product water must be effectively removed because otherwise the electrode would flood and prevent oxygen access.

As shown in Figure 2.7a, the reactions take place at TPB, which is ionomer, solid, and void phases. However, this boundary has an infinitesimally small area that would result in infinitely small current densities. In practice, because some gas may permeate through the polymer, the reaction zone is larger than a single three-phase boundary line. The reaction zone may be enlarged by either roughening the surface of the membrane or by incorporating ionomer in the catalyst layer (Figure 2.7b). In an extreme case, the entire catalyst surface may be covered by a thin ionomer layer (Figure 2.7c), except for some allowance for electrical contacts. Obviously, the ratios between the catalyst area covered by ionomer to catalyst area opened to void to catalyst area contacting other catalyst particles or electrically conductive support must be optimized.

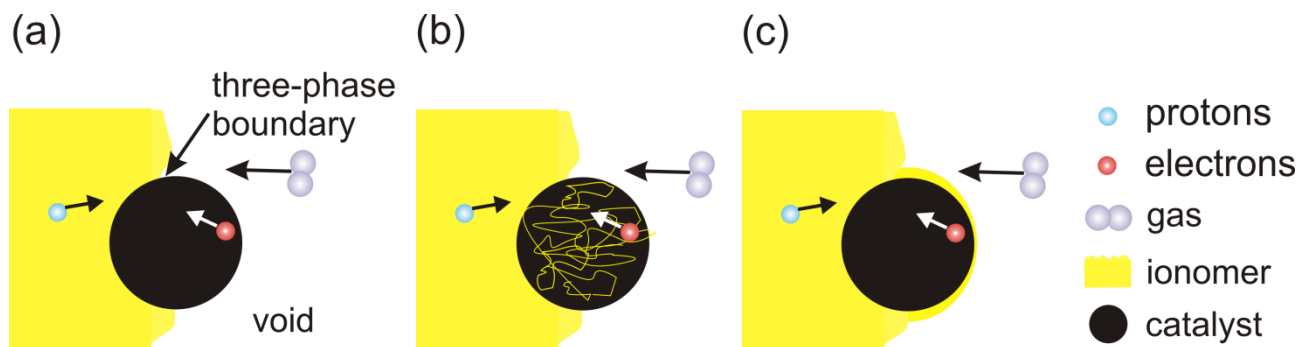


**Figure 2.7** Graphical representation of the reaction sites.

The most common catalyst in PEMFC for both oxygen reduction and hydrogen oxidation reactions is platinum. Pt has excellent properties: 1) high catalytic activity, 2) chemical stability, 3) good exchange current density, and 4) superior work function. However, the global scarcity of Pt and its high cost demand for an urgent need to reduce the use of Pt and to improve the efficiency in PEMFC. Therefore, catalysts in PEMFC are currently supported on conductive and porous carbon materials. With the use of supported catalyst structure platinum amount was reduced to 0.3-0.4 mg cm<sup>-2</sup>. It is important to have small platinum particles (2~5 nm) with large specific surface area finely dispersed on the surface of the catalyst support. It is also well known that carbon-supported metal catalysts show improved stability and higher activity compared to unsupported bulk metal catalysts.

As the use of a catalyst support, carbon materials have great advantages as follows:

- 1) Metals on the support can be easily reduced;
- 2) The carbon structure is resistant to acids and bases;
- 3) The structure is stable at high temperatures;

- 4) Porous carbon catalysts can be prepared in different physical forms, such as granules, cloth, fibers, pellets;
- 5) The active phase can be easily recovered;
- 6) The cost of conventional carbon supports is usually lower than that of other conventional supports (alumina and silica).

Nevertheless, carbon supports also present some disadvantages:

- 1) They can be easily gasified, which makes them difficult to use in high temperature hydrogenation and oxidation reactions;
- 2) Their reproducibility can be poor, especially activated carbon-based catalysts, since different batches of the same material can contain varying ash amounts.

An ideal support should offer the following:

- 1) Large specific surface area, which is necessary for improving the dispersion of catalytic metals;
- 2) Good electrochemical stability under fuel cell operating conditions;
- 3) High conductivity;
- 4) Low combustive reactivity under both dry and humid air conditions at low temperatures
- 5) Good corrosion resistance.

In the next session, I will briefly introduce the main catalyst supports, and present the possible perspectives of using that of carbon supports for energy generation and storage applications.

## **2.4 Catalyst Supports**

The physical and chemical properties of carbon materials, such as their tunable porosity and surface chemistry, make them suitable for application in many catalytic processes. Traditionally, carbon materials have been used as supports for catalysts in heterogeneous catalytic processes, although their use as catalysts on their own is becoming more and more common. Although several kinds of carbon materials have been studied, activated carbon (AC) and carbon black are the most commonly used carbon supports. The typically large surface area and high porosity of activated carbon catalysts favor the dispersion of the active phase over the support and increase its resistance to sintering at high metal loadings. The pore size distribution can be adjusted to suit the requirements of several reactions. The surface chemistry of carbon catalysts influences their performance as catalysts and catalyst supports.

## 2.4.1 Types of Catalyst Supports

The support materials are necessary to obtain a high dispersion and a narrow distribution of Pt and Pt-alloy nanoparticles, which is the prerequisite to obtain a high catalytic performance of catalysts. The support materials can also interplay with catalytic metals, which influence the catalytic activity. The durability of the catalyst is also greatly dependent on its support.

The most popular support material is Vulcan XC-72 carbon black. The high surface area ( $\sim 250 \text{ m}^2 \text{ g}^{-1}$  for Vulcan XC-72), low cost and easy availability of carbon black help reduce the overall cost of the fuel cell. Although widely used as catalyst-support, carbon black still suffers from problems such as the presence of organo-sulphur impurities, deep micropores or recesses which trap the catalyst nanoparticles making them inaccessible to reactants thus leading to reduced catalytic activity. The pore size and pore distribution also affect the interaction between Nafion<sup>®</sup> ionomer and the catalyst nanoparticles. Furthermore, thermochemical stability of carbon black is required under acidic conditions of a typical PEMFC and the absence of this leads to corrosion of the carbon support resulting in disintegration of catalyst layer. Consequently, much effort has been devoted to developing novel catalyst supports, including novel nanostructured carbons such as carbon nanotubes (CNT) [57–59], carbon nanofibers (CNF) [60] and mesoporous carbon [61], oxides [62], carbides [63], nitrides [64], etc. Nanostructured carbon can also be doped by other atoms [65, 66] or compounds to enhance both the catalytic activity and durability of the resultant catalysts. Recent progress in several important carbon-based catalyst supports is briefly summarized in Table 2.1.

### 2.4.1.1 Metals

To reduce the usage of expensive Pt and at the same time to improve the catalyst activity toward fuel cell reactions, one of the approaches is to develop some cost-effective metal-supported Pt catalysts. A typical metal-supported catalyst contains metal support particles and the metal catalyst particles. In the state of art, the metal support particles provide a physical surface for dispersion of smaller catalyst particles to achieve a high surface area. In some synthesis cases, the formed catalysts might be sintered at high temperatures to increase the attachment between the support and the catalyst particles. This process can produce some degree of alloying between the catalyst metal and the metal support, leading to improved catalyst activity and durability. The strong physicochemical and electronic interaction between the metal support and the catalyst particles can generate a bifunctional mechanism for catalytic reaction, benefiting the reaction kinetics. For Pt-based catalysts in PEMFC reactions [67, 68] several metals have been explored for metal supports, including Ru, Pd, Ag, Ir, Rh, Au, Re, Os, as well as Co. By the use of these catalysts a

high ORR activity was achieved through the modification [69-72] and control of the surface reactivity of catalyst metal monolayers [73-75].

#### **2.4.1.2 Carbon Nanotubes**

CNTs are 1D nanostructures, typically tubes formed by rolled up single sheets of hexagonally arranged carbon atoms. Depending on the structure, single walled CNT (SWCNT) can be conducting, i.e. metallic as well as semi-conducting in nature. Multi-walled CNT (MWCNT) can have diameters of a few tens of nanometers with a spacing of 0.34 nm between cylindrical walls. CNTs have advantages as compared with conventional carbon black for PEMFC electrocatalyst supports: 1) the unique structure and electrical properties of CNT provide a high electrical conductivity and a specific interaction between catalytic metals and the CNT supports, resulting in a higher catalytic activity, 2) CNTs have few impurities, 3) CNTs make it possible to construct an ordered catalyst layer in PEMFC [59, 76], which might provide benefits for mass/electron transport, resulting in higher cell performance.

#### **2.4.1.3 Carbon Nanofibers**

CNF is an industrially produced derivative of carbon formed by the decomposition and graphitization of rich organic carbon polymers. The most common precursor is polyacrylonitrile (PAN), as it yields high tensile and compressive strength fibers that have high resistance to corrosion, creep, and fatigue. For these reasons, the fibers are widely used in the automotive and aerospace industry [77]. Carbon fiber is an important ingredient of carbon composite materials, which are used in fuel cell construction, particularly in GDL where the fibers are woven to form a type of carbon cloth.

CNFs have a structure with ordered parallel graphene layers arranged in a specific conformation and are a novel graphitic support material with promising applications.

#### **2.4.1.4 Mesoporous Carbon**

Mesoporous carbon is a porous carbon material with pore sizes varying between 2-50 nm [78]. It can be classified to ordered mesoporous carbon (OMC) and disordered mesoporous carbon (DOMC) [79-91]. The disordered mesopores in irregular structures carbon are isolated and the pore size distribution is wider than in OMC [78].

The pore structure of mesoporous carbon is controlled by hard-templating method [92] where inorganic porous materials such as alumina membranes [93], zeolites [94], aerogels [95, 96], opals

[97], micelles [98] and ordered mesoporous silica [99-106] are used as templates. However, the structure and morphology of the produced mesoporous carbon materials are limited to the parent template [107] and thus new alternative methods are being investigated. These novel synthesis techniques include the evaporation-induced self-assembly [108-111] and hydrothermal method [107, 112]. Highly ordered mesoporous carbon with large uniform pores and high surface area was obtained.

Mesoporous carbon materials as catalyst supports for PEMFC have been extensively studied [113-115]. In contrast to conventional carbon supports, mesoporous carbon exhibits an attractive property structure as a catalyst support, i.e. a large surface area with mono-dispersed three-dimensionally interconnected mesopores. The mesoporous carbon-supported Pt [116, 117] and Pt alloy catalysts [118, 119] and even non-precious metal catalysts [120] have shown excellent performance in PEMFC electrode reactions. This is attributed to the high and uniform dispersion of catalytic metals, the high electrical conductivity, and the enhanced mass transfer due to the specific pore structure of mesoporous carbon [121].

#### **2.4.1.5 Diamond**

Diamond is another natural allotrope of carbon that has cubic structure in which each atom uses  $sp^3$  orbitals to form four strong, covalent bonds. These bonds contribute to the hardness and high melting point of diamond.

Due to its extreme chemical and electrochemical stability one of the most promising alternative support materials that has been considered is diamond, although in its nondoped form it has insufficient electrical conductivity [122, 123]. Diamond in nanoparticle form affords the opportunity of more facile doping because of its high surface area [124, 125]. If convenient ways to dope diamond nanoparticles could be developed, the latter could be quite promising as an electrocatalyst support material [126, 127].

#### **2.4.1.6 Graphene**

Graphene is an atomically thin sheet of hexagonally arranged carbon atoms which has attracted a lot of interest since its discovery by Geim et al. in 2004 [128]. It offers high conductivity and one of the fastest available electron transfer capabilities. As such, it is widely studied for various applications including fuel cell catalyst support. The use of graphene and its oxide (graphene oxide) in fuel cell is not only limited to that of catalyst support but it is also being explored as material for (i) conducting membranes as a composite with polymers and also as (ii) bipolar plate material [129].

Graphene has aroused interest as potential support owing its high electron transfer rate, large surface area and high conductivity [130-133]. The 2D planar structure of the carbon sheet allows both the edge planes and basal planes to interact with the catalyst nanoparticles. The rippled but planar sheet structure also provides a very high surface area for the attaching catalyst nanoparticles. Table 2.2 summarizes the carbonaceous materials discussed in this thesis.

**Table 2.2** Types of carbonaceous support materials for PEMFC: properties, electrochemically active surface area (ECSA) and observations.

Type of support	Support properties	ECSA (m <sup>2</sup> g <sup>-1</sup> )	Observation /comments	Ref.
<b>Metals</b>	<ul style="list-style-type: none"> <li>• sp<sup>2</sup>/sp<sup>3</sup> carbon</li> <li>• High conductivity</li> <li>• High catalyst activity</li> </ul>		<ul style="list-style-type: none"> <li>• metal stability and dispersion</li> <li>• High resistance to CO-poisoning</li> </ul>	[67, 68]
<b>CNT</b>	<ul style="list-style-type: none"> <li>• sp<sup>2</sup> carbon</li> <li>• Hydrophobic</li> <li>• High conductivity</li> <li>• N-doped CNTs for ORR</li> </ul>	Up to 44.3	<ul style="list-style-type: none"> <li>• Larger catalyst particles without surface treatment</li> <li>• Good metal dispersion in case of SWCNT</li> <li>• High metal stability for MWCNT</li> </ul>	[134-139]
<b>CNF</b>	<ul style="list-style-type: none"> <li>• sp<sup>2</sup> carbon</li> <li>• High conductivity</li> <li>• 3.9 S cm<sup>-1</sup></li> <li>• High durability</li> <li>• N-doping for ORR</li> </ul>	20–80	<ul style="list-style-type: none"> <li>• Long term stability and durability</li> <li>• Increased graphitization enhances ORR</li> </ul>	[140-143]
<b>Mesoporous carbon</b>	<ul style="list-style-type: none"> <li>• sp<sup>2</sup>/sp<sup>3</sup> carbon</li> <li>• High surface area</li> <li>• 0.3 S cm<sup>-1</sup></li> <li>• Good pore structure and size distribution</li> <li>• Few O-functional groups</li> </ul>	62.96	<ul style="list-style-type: none"> <li>• Easier mass transportation with desired pore morphology</li> <li>• Lack of good contact between Pt and Nafion buried inside large pore</li> </ul>	[144-152]
<b>Diamond</b>	<ul style="list-style-type: none"> <li>• sp<sup>3</sup> carbon</li> <li>• Low surface area</li> <li>• High stability</li> <li>• Low conductivity</li> <li>• Doped</li> <li>• High resistance to poisoning</li> </ul>	-	<ul style="list-style-type: none"> <li>• Low metal stability and dispersion</li> <li>• Agglomeration and large nanoparticle size variation</li> </ul>	[153-156]
<b>Graphene</b>	<ul style="list-style-type: none"> <li>• sp<sup>2</sup> carbon</li> <li>• Hydrophobic</li> <li>• High conductivity</li> <li>• 10<sup>3</sup>–10<sup>4</sup> S cm<sup>-1</sup></li> <li>• N-doping for ORR</li> </ul>	44.6–81.6	<ul style="list-style-type: none"> <li>• Often produced from reduced GO</li> <li>• Can be prepared as vertically aligned 1–3 layers graphene</li> <li>• High resistance to CO-poisoning</li> <li>• Properties depend on synthesis method</li> </ul>	[157-159]

## 2.4.2 Recent Development

In recent years, porous carbons have been of growing interest in new applications because of the hydrophobic nature of their surfaces, high surface area, large pore volumes, chemical inertness, good mechanical stability, and good thermal stability. Furthermore, very recently, hierarchical porous carbon materials have been proved to possess distinctive potential for high performance fuel cells [160, 161] because the well-defined hierarchical porosity could effectively concert each pore level during the electrochemical process. That is the meso-/or macropore channels with larger pore size could serve as micro reservoirs of electrolyte and the expressway for ion-transport, resulting in a decreased diffusion distance and high power performance. Also, the micropores within the wall of the meso-/or macropores supply high effective specific surface area. Therefore, catalyst support technology with using a hierarchical porous structure [160-167] is widely utilized as an effective approach to reduce the use of Pt catalysts and improve catalytic activity.

## 2.4.3 Hierarchical Porous Carbon

Many different classifications of the hierarchical materials have been proposed depending on the pore-geometry (size, porosity), pore-structure (closed pore or open pore structures), pore-arrangement (random or ordered pore arrangements), and material composition (metal, oxide, or carbon). The types of pores are defined by International Union of Pure and Applied Chemistry (IUPAC) as micropore (pore size <2 nm), mesopore (2–50 nm), and macropore (>50 nm) [168, 169].

Naturally occurring species are employed as resource for a wide range of materials which suggests that a significant fraction of complex functionalities of living systems are based on their hierarchical structures [170]. Compared to conventional porous materials with uniform pore dimensions that can be adjusted over a wide range of length scales, hierarchical porous materials with well-defined pore dimensions and topologies offer minimized diffusive resistance to mass transport by macropores, and high surface area for active site dispersion over the micro- and/or mesopores [171]. Such novel types of interconnected porous carbon materials with a 1D to 3D network are currently attracting a great degree of interest due to their potential technological application profile ranging from electrochemical capacitors [172], lithium ion batteries [173], solar cells [174], hydrogen storage systems [175], photonic materials [176], fuel cells [177], and sorbents for toxic gas separation [178]. Good electrical conductivity, high surface area, and excellent chemical stability are certain unique physicochemical properties which have caused micro/nanostructured porous carbon to be a highly trusted candidate for emerging nanotechnologies. Novel porous carbon materials with controlled morphology, porosities, and architectures are highly desirable because of their unique structural features, which have

mesopores in combination with macropores or micropores. The design of hierarchical porous carbons (HPC) with tailored macro-/mesopores and doping of electron-donating element has emerged as a promising field of further investigation with an extensive scope.

The most commonly used synthetic technique is currently templating methods. A range of different synthesis techniques for the fabrication of HPC through templating are available [179].

- Sol-gel deposition: The gelation (hydrolysis and condensation reactions) of a precursor sol in the presence of a template is initiated by adjustment of temperature or pH value.
- Electrodeposition: The template surface needs to be electronically conductive. It is coated with a metal film serving as cathode for electroplating of the precursor. The growth of the nanostructure is controllable by the applied voltage and time.
- Electroless (chemical deposition): Compared to electrodeposition the template surface does not have to be electrically conductive but the material is rather deposited by the utilization of a chemical agent. Here, the structure dimension is preset by the template but through adjustment of the reaction time either hollow (short reaction time) or solid (longer reaction time) structures are produced.
- Chemical polymerization: The template is immersed in a solution containing a monomer and a polymerization agent. The polymerization preferentially takes place on the template surface, thus the polymer adapts the template morphology.
- Chemical vapor deposition (CVD): The volatile precursor is solidified on the template surface. This technique is useful for the production of thin films and highly pure materials.

Regarding the template species, two different approaches such as hard- and soft-templating can be distinguished, including their merits and drawbacks:

(1) Soft-templating: This approach is based on the utilization of surfactants (e.g. cetyltrimethylammonium bromide, CTAB) or block copolymers (e.g. poly(ethylene oxide)- or poly(styrene)-based block copolymers) as template phase. These structures are very interesting since they are able to self-assemble into a variety of macromolecular architectures and their properties are easily tunable [180, 181].

The most prominent examples for soft-templating are the silica materials MCM-41 and MCM-48 [182]. Beck et al. [183] suggested the formation pathway of surfactant templated silica. A cooperative mechanism occurs at low surfactant concentrations, whereas at high concentrations the surfactant liquid crystals serve as template.

(2) Hard-templating: This approach is employed with a fixed structure. The fixed structure does not change throughout the process. Therefore, hard-templating has the great advantage of a relatively easy control compared to soft-templating. The synthesis of mesoporous carbons by templating of a phenol-hexamine mixture with spherical solid gels was reported by Knox et al. [184].

In general, the hard-templating process includes four main steps: 1) template synthesis; 2) impregnation or infiltration with the precursor; 3) network formation of the precursor; 4) template removal.

Although the production of samples could lead to an extremely high surface area (up to  $4100 \text{ m}^2 \text{ g}^{-1}$ ), most of templates have a major drawback that is the pore collapse of the templated material either during solidification of the precursor or after template-removal. In particular, the necessity of removing the template employing hazardous or aggressive chemicals such as hydrofluoric acid (HF) makes these synthesis routes not attractive for industrial applications. Another issue is very much time-consuming. Therefore, building a hierarchical porous structure by a template-free method is a big challenge today. The usefulness of hierarchical open-pore structures is also the demand for low costs and sustainability. This is clearly one of the most challenging but also fascinating tasks in the synthesis of porous materials and will be addressed in the present thesis.

#### **2.4.4 Hierarchically Structured Nitrogen-Coated Porous Carbon**

Nitrogen doping in carbon-based nanostructures is an effective way to tailor the properties of carbon-based materials and render their potential applications in environmental issues including fuel cells, catalysis, photocatalysis, and  $\text{CO}_2$  capture etc [185-191]. The nanoporous structures within the bulk of nitrogen-doped carbon have enhanced their performance in such applications because nitrogen-doped carbon shows a high oxidation resistance capability and higher catalytic activity. Maldonado and Stevenson [192] found that N-doped carbon fiber showed an improved catalytic activity by shifting the ORR potential up by 70 mV, and electron transfer number of ORR catalyzed that N-doped carbon fiber was close to four. They discussed that N-doped carbon can catalyze not only  $\text{O}_2$  reduction but also  $\text{H}_2\text{O}_2$  decomposition. The active sites in N-doped carbon are carbon atoms adjacent to the N atom. Using a cluster model, Sidic et al. [193] found that the carbon radical sites adjacent to the substitutional N showed strong bonding ability to adsorbed OOH, favoring the production of  $\text{H}_2\text{O}_2$ , which could improve its catalytic activity.

N-doped mesoporous carbons are often prepared by a nanocasting method using a sacrificial template, typically porous silica. Nitrogen functionality can be incorporated by impregnation with nitrogen-containing organic molecules, followed by carbonization and removal of the silica template, or through post-synthesis treatment of mesoporous carbon using acetonitrile or ammonia chemical vapor deposition. These multi-step processes are costly and time consuming. Other

methods include the co-assembly of a nitrogen-containing monomer, melamine resin or urea-phenol-formaldehyde resin, however, the resulting porous polymers usually exhibit poor thermal stability. To improve the conductivity and stability, the synthesis of nitrogen-containing porous carbons is further promoted by thermal decomposition of ionic liquids.

In the present thesis, hierarchically structured N-containing porous carbons are presented consisting of graphene foams, surface modified graphene and CNT structures for efficient catalyst supports.

This structure has the capability of coating the surface area and would be potentially of great interest for the development of catalytic, electronic, fuel cell, and hydrogen storage systems. The results are discussed in Chapter 5 and Chapter 6.

#### **2.4.5 Catalytic Property of Nitrogen-Containing Carbon**

Introduction of heteroatoms such as nitrogen results in modifications of the chemical as well as physical properties. One can distinguish between surface and structural modifications. In the case of layered edge chemical nitrogen this leads to a Brønsted-basicity. In contrast, if the heteroatoms are structurally incorporated into the carbon, the physical properties of the material drastically change. Structural nitrogen is reported to modify the band structure by lowering the valence band and increasing the electron density at the Fermi-level. Thus, the material becomes chemically more stable and it is sometimes referred to as noble carbons [194, 195]. Another prominent example is the increased electrical conductivity achieved by doping carbon materials with the electron-rich nitrogen [196]. In contrast to surface-bound nitrogen functionalities which introduce Brønsted-basicity, structural nitrogen adds Lewis-basicity to the carbon material. This is of special interest for catalytic applications and among others it was already shown that N-doped carbon possesses superior catalytic activity for the ORR [197, 198]. Besides catalysis, the incorporation of both surface and structural nitrogen in carbon materials increases the performance of the materials as electrodes for energy storage and conversion applications.

Briefly, the preparation methods for doped carbon catalysts can be classified as pyrolysis, annealing, CVD, arc discharge, plasma treatment, etc. More detailed discussion on these preparation methods are presented as follows:

##### **(1) Pyrolysis**

Pyrolysis is mainly used in decomposition of macromolecules, such as metal contained phthalocyanine and porphyrin or other heteroatom-containing precursors to expose their inner active sites. It is one of the most effective approaches to optimize catalysts, as previously reported

[199-202]. Zelenay et al. [200] demonstrated the catalyst of polyaniline (PANI)–Fe–C with outstanding activity prepared by pyrolysis.

## (2) Annealing

Annealing is utilized in post-treatment to enhance the stability of the as-prepared metals and alloys in metallurgy. In the field of chemical preparation, it mostly represents the heat treatment for solids or thin films under specific atmosphere. For instance, Sun et al. [201] reported that a catalyst of N-doped graphene prepared by annealing graphene oxide (GO) in  $\text{NH}_3$  and Ar at 900 °C exhibited higher onset potential and larger kinetic limiting current of ORR.

## (3) Chemical vapor deposition

CVD is a facile controllable process that offers high quality nanocarbon, such as carbon nanotubes [203] and graphene [204]. Typically, the process is often performed on a substrate (e.g. Cu film on a Si substrate) in a quartz tube of a furnace filled with inert gas to prevent side oxidation reaction. By pumping carbon and nitrogen-containing precursors into the gas, the precursors will be decomposed under high temperature and subsequently deposited on the substrate. For instance, Dai et al. reported the preparation of highly active N-doped carbon nanotube arrays (VA-NCNT) for ORR using iron(II) phthalocyanine and  $\text{NH}_3$  as precursors.

## (4) Arc discharge

Arc discharge is the phenomenon of the electrical breakdown of the gas between two electrodes at high voltage accompanied with spraying plasma to the counter electrode. This method has recently been applied to prepare N-doped nanocarbon.

## (5) Plasma treatment

Plasma is commonly a state of matter high energy caused by the ionization of gas, such as electrical induction [205]. It has been widely used for the modification of materials on a large scale [206], including functionalized graphene and its derivatives by replacing carbon with foreign atoms [207]. Moreover, plasma treatment has been used to assist CVD to grow metal free N-doped CNTs which performed good ORR catalytic behavior [208].

For applicability of these approaches, the advantage of pyrolysis and annealing methods is the capability of facilitating the formation of graphitic structures, which likely contributes to the enhancement of the current density. However, the complicated structural variations would result in difficulties to reveal the active site of catalysts. CVD is capable of preparing designed structure of high quality nanocarbon. However, the contradiction is the high cost of instruments that hampers

its large scale application for preparing ORR catalysts. Because of the limitations caused by high costs, scale-up problems, and the use of a complex instrumentation, here, we will introduce a new approach with a simple, scaleable and cheaper process. For applying of the vast potential of N-doped carbons, furthermore, the present work will describe the synthesis of new materials, and its use for fuel cell applications in Chapter 5,6.

#### **2.4.5.1 Different Types of Nitrogen Species**

When a nitrogen atom is doped into graphene, it usually has three common bonding configurations within the carbon lattice, including quaternary-N (or graphitic-N), pyridinic-N, and pyrrolic-N. As shown in Figure 2.8, nitrogen atoms can be doped into the basal plane of a graphitic carbon (graphene) sheet in several different configurations [209, 210]. The characteristic XPS peaks for pyridinic-, pyrrolic-, and quaternary-N are located at about 398.6, 400.5, and 401.4 eV [211, 212], respectively. These different nitrogen configurations could vary the electronic structure of neighbor carbon atoms and then affect physical and chemical properties, such as electrical conductivity and electrocatalytic activity [213]. Previous studies have shown that the edge structure and doped-N near the edge could significantly enhance the ORR activity through the four-electron pathway [214, 215].

In addition, the armchair and zigzag sites located at the edges through the  $sp^2$  hybridization are high energy sites, which could be functionalized with heteroatoms to provide strong electrochemical activities. Several research groups have reported that the pyridinic-N was the active site to enhance the ORR activity of the N-doped carbon materials [216-223], whereas some others suggested that more graphitic nitrogen atoms, rather than the pyridinic ones, are important for the ORR [224, 225]. Therefore, the exact catalytic role for each of the nitrogen forms in nanocarbon ORR catalysts is still a matter of controversy. An interconversion of the quaternary to pyridinic sites through the ring opening of a cyclic C-N bond or vice versa has been proposed to reconcile the controversy over whether the quaternary, pyridinic, or both nitrogens are active sites for ORR [226].

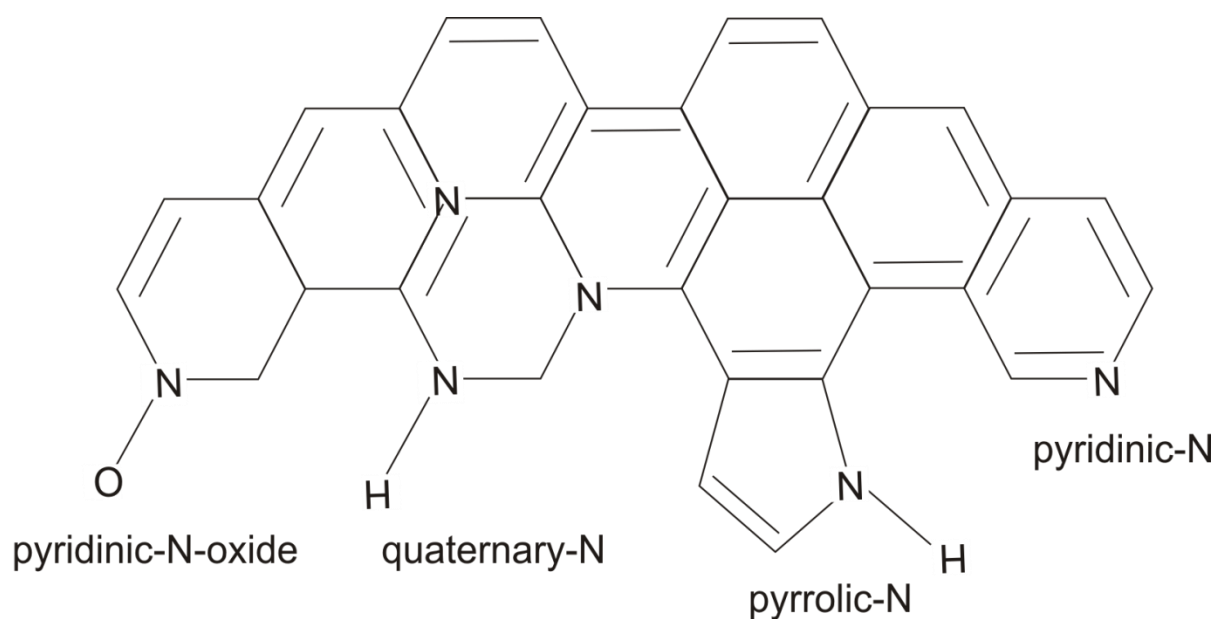


**Figure 2.8** Schematic illustration of nitrogen species in N-containing graphitic carbons. The commonly doped nitrogen species in graphitic carbons with the corresponding reported XPS bonding energies.

One limitation of nitrogen heteroatom is their deletion at high temperature. At very high temperature, carbon becomes more graphitic i.e. the graphene planes become more planar and stacked uniformly with the distance between adjacent graphene layers approaching 3.354 Å. The N also becomes more reactive so that it has energy enough to combine to form N<sub>2</sub> and leave the carbon surface. Hence, nitrogen content and graphiticity are reciprocal properties with respect to the temperature. This has direct consequence during the preparation of N-doped carbon using N containing carbon precursors. Also, the types of N-groups would change during heating process because more thermally reactive N-groups would leave while less thermally reactive N-groups would stay. As the N atoms become mobile at high temperature, one type of N-group can also transform into another more stable N-group. So the amount and type of N-groups would also change with temperature.

#### 2.4.5.2 Oxygen Reduction Reaction

Several typical ORR processes with their corresponding thermodynamic electrode potentials at standard conditions are listed in Table 2.3. The mechanism of the electrochemical O<sub>2</sub> reduction reaction involves many intermediates, primarily depending on the natures of the electrode material, catalyst, and electrolyte.

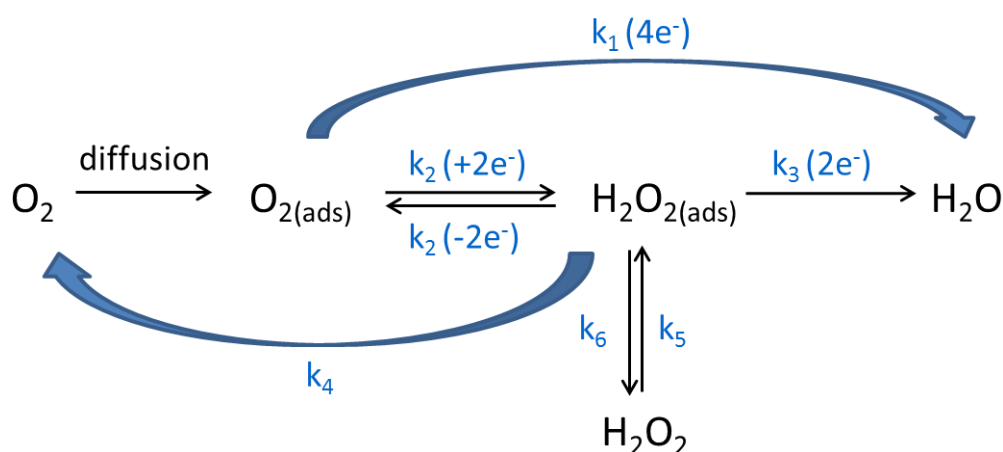
**Table 2.3** Thermodynamic electrode potentials of electrochemical O<sub>2</sub> reductions [227, 228].

Electrolyte	ORR reactions	<sup>a</sup> E <sup>0</sup> , / V
Acidic aqueous solution	$O_2 + 4H^+ + 4e^- \rightarrow 2H_2O$	1.229
	$O_2 + 2H^+ + 2e^- \rightarrow H_2O_2$	0.695
	$H_2O_2 + 2H^+ + 2e^- \rightarrow 2H_2O$	1.76
Alkaline aqueous solution	$O_2 + 2H_2O + 4e^- \rightarrow 4OH^-$	0.401
	$O_2 + H_2O + 2e^- \rightarrow HO_2^- + OH^-$	-0.065
	$HO_2^- + H_2O + 2e^- \rightarrow 3OH^-$	0.867
Non-aqueous aprotic solvents	$O_2 + e^- \rightarrow O_2^-$	b
	$O_2^- + e^- \rightarrow O_2^{2-}$	c

\* a: Thermodynamic electrode potential at standard conditions

b, c: The thermodynamic potentials for the 1-electron reduction reaction to form a superoxide, and its further reduction to O<sub>2</sub><sup>2-</sup>, are not listed in Table 2.3 because their values are strongly dependent on the solvent used.

In Table 2.3, the reduction pathways such as the 1-, 2-, and 4-electron reduction pathways have unique significance, depending on the applications. In fuel cell processes, the 4-electron direct pathway is highly preferred. The 2-electron reduction pathway is used in industry for H<sub>2</sub>O<sub>2</sub> production. The 1-electron reduction pathway is of importance in the exploration of the ORR mechanism. The generalized scheme for the ORR is shown in Figure 2.9 [229].



$k_1$  = rate constant for 4e<sup>-</sup> direct reduction to H<sub>2</sub>O or OH<sup>-</sup>

$k_2$  = 2e<sup>-</sup> reduction to H<sub>2</sub>O<sub>2</sub> or HO<sub>2</sub><sup>-</sup>

$k_3$  = electrochemical reduction of H<sub>2</sub>O<sub>2</sub> to water or OH<sup>-</sup>

$k_4$  = catalytic decomposition of H<sub>2</sub>O<sub>2</sub> or HO<sub>2</sub><sup>-</sup> yielding reducible product

$k_5$  = desorption of adsorbed H<sub>2</sub>O<sub>2</sub> or HO<sub>2</sub><sup>-</sup>

$k_6$  = adsorption of  $H_2O_2$  or  $HO_2^-$

**Figure 2.9** Schematic presentation of ORR pathway.

### 2.4.5.3 Chemical Stability

Carbon corrosion is one of the major issues in carbon-based electrochemical devices. It takes place through the formation of surface oxides which eventually come out as  $CO_2$  and  $CO$  [230]. Hence, carbon stability can be increased just by removing these oxygen containing surface groups. Heat treatment ( $>600$  °C) is often carried out during N-doping. Thus, oxygen content by heating increases which decreases resistance towards corrosion. Also, there are other beneficial effects of heating such as replacement of thermally unstable acidic oxygen containing species (e.g. carboxyl and hydroxyl groups) and increase in surface homogeneity of graphene plane which also increases stability as corrosion starts at defects. In addition, graphitic-N might not affect the carbon corrosion as they are not located at defect sites.

This indicates that the N-doped carbon is thermodynamically more stable than the non-doped carbon. The basic N-doped carbon is reductive in nature due to delocalized  $\pi$  electrons of graphitic-N. It is proposed that N-doped carbon reduces adsorbed  $O_2$  molecules to superoxide radical ( $O_2^{\cdot-}$ ) which can react with water to form  $H_2O_2$  instead of surface oxides [231].  $H_2O_2$  decomposes 10 to 100 times faster on the N-doped carbon than on the non-doped carbon [232]. Thus, reduction of  $O_2$  in the presence of water is more kinetically favorable than formation of surface oxides, which are intermediates during carbon corrosion. Hence, the N-doped carbon shows higher resistance towards corrosion.

### 2.4.5.4 Electronic Conductivity

N-doping creates various nitrogen functional groups on the carbon surface. The surface properties of carbon depend on the type of nitrogen functional groups. The most common nitrogen functional groups found in N-doped graphene are pyrrole, pyridine and quaternary or graphitic-N groups (as shown in Figure 2.8). In an ammonia molecule, the nitrogen atom has four  $sp^3$  hybridized orbitals. Three of the orbitals have one electron involved in  $\sigma$  bonds with the hydrogen atoms while the remaining orbital has two electrons.

The lone pair of electrons make ammonia molecule basic as these can be donated or shared with an electrophilic species such as  $H^+$  to form  $NH_4^+$ . In pyrrole, the nitrogen atom has three  $sp^2$  orbitals, each containing one electron that forms  $\sigma$  bonds with neighboring carbon and hydrogen atoms. The remaining pair of electrons resides in  $\pi$ -orbitals of the aromatic system. Hence pyrrole

does not have electron donating properties. In pyridine, two of the three  $sp^2$  orbitals occupy one electron each forming  $\sigma$  bonds with the adjacent carbon atoms. The third  $sp^2$  orbital has a lone pair of electrons which are localized and can be donated, similar to ammonia. Hence, pyridine is basic. The remaining electron is located in a  $\pi$ -orbital and contributes to the aromatic structure of pyridine. In graphitic-N, three  $sp^2$  orbitals have a single electron forming three  $\sigma$  bonds with the carbon atoms. One  $\pi$ -electron orbital is donated to the aromatic system. The remaining  $\pi$ -electron is located in an antibonding  $\pi$ -orbital and is delocalized. Therefore, pyrrole does not impart basic character to the carbon, and pyridine and graphitic-N groups play the biggest role in the surface properties of N-doped carbon. Fuertes et al. [233] demonstrated that N-doping increases the basic nature of the carbon which can be attributed to the pyridinic and/or graphitic-N.

### **3. Characterization Techniques**

The catalytic activities of carbon-supported materials are strongly dependent on their size, composition, morphology, and surface properties. Various characterization techniques have been applied to their structural analyses. Moreover, detailed structural characterizations are needed for deeply understanding the structure–property–catalytic activity correlations, which further provide the fundamental basis for structural optimization and synthesis of carbon materials for applications in electrocatalysts. For instance, it has been found that the electrocatalytic activities of metal nanoparticles are dependent on their structures such as modified surface, the crystalline size, coated thickness, etc. In this section, we briefly summarize the commonly used techniques for structural characterization of carbon-supported platinum catalysts, mainly including X-ray (XRD, XPS, EDX) spectroscopy, electron microscopy (TEM, SEM), BET-nitrogen sorption, elemental analysis and Raman spectroscopy.

#### **3.1 Electron Microscopy Techniques**

##### **3.1.1 Scanning Electron Microscopy (SEM)**

Electron microscopy has traditionally been used to directly obtain the morphology information of the used materials. SEM images were taken with a JXA-840A (Jeol, Akishima-Shi, Japan) and Helios NanoLab™ 600 microscope (FEI, Eindhoven, The Netherlands). Samples were fixed in the dry, powder state on the sample holder with a diameter of 2.5 mm.

##### **3.1.2 Transmission Electron Microscopy (TEM)**

TEM pictures were taken with a JSM 6400 F instrument (Jeol, Munich, Germany). Samples were suspended in ethanol and applied on a TEM grid.

##### **3.1.3 Energy Dispersion X-ray spectroscopy (EDX)**

The chemical composition of carbon supports and platinum nanoparticles were determined by EDX using a JXA-840A with Helios NanoLab™ 600 microscope. EDX was operated at an accelerating voltage of 20 kV, a beam current of 0.4 nA and a working distance of 20 mm. The sample was prepared on a Cu grid covered carbon tab (PLANO, Germany).

## 3.2 Structural Characterization

### 3.2.1 Powder X-ray Diffraction (XRD)

XRD analysis is usually used to study the crystal structure and evaluate the crystal size of nanomaterials based on the Debye–Scherrer equation. By XRD characterization, the formation of used supports and catalysts can be identified. XRD measurements were carried out with a X'Pert Pro diffractometer (Panalytical B.V., Almelo, Nederland) using CuK $\alpha$ -radiation ( $\lambda = 1.54056 \text{ \AA}$ ) operating at 40 kV and 40 mA. A  $2\theta$ -range from 10 to 80 degree was measured with a step size of  $0.5^\circ/\text{min}$ . In the center of the sample holder, the powder sample was positioned. The powder was carefully flattened and flushed to form a smooth surface. All XRD profiles were analyzed with using the X'pert HighScore Plus program developed by PANalytical B.V. The deposited platinum catalysts were characterized in order to verify the crystallinity and the size of the particles. The crystallite size could be estimated by evaluating the line width of the platinum (111)-peak by the Scherrer equation [234],

$$d_v^{XRD} = \frac{0.9\lambda}{\Delta 2\theta \cos\theta} \quad \text{Eq.2.1}$$

where  $d_v^{XRD}$  is the averaged particle diameter,  $\lambda$  is the wavelength of the X-ray wavelength (1.54  $\text{\AA}$ ),  $\Delta (2\theta)$  is the full-width at half-maximum (FWHM) of the diffraction peak and  $\theta$  is the Bragg angle.

## 3.3 Chemical and Physicochemical Characterization

### 3.3.1 CHN analysis

The elemental analysis was carried out on a CHNS Vario EL3 (Elementar Anlysen Systeme GmbH, Germany) instrument using the CHN combustion method. The samples were combusted in a pure oxygen atmosphere and the resulting products were analyzed by TCD analysis (thermal conductivity detection) with respect to  $\text{NO}_2$ ,  $\text{CO}_2$  and  $\text{H}_2\text{O}$ .

### 3.3.2 Inductively Coupled Plasma – Optical Emission Spectroscopy (ICP-OES)

The platinum loadings of the catalysts were determined by ICP-OES measurements with a Varian 720-ES analyzer (Varian Inc., Palo Alto, California). First the samples were weighed and heated up to  $180^\circ\text{C}$  for 120 min; then for 360 min at  $450^\circ\text{C}$ , and finally 60 min at  $800^\circ\text{C}$ . The residue was boiled and dissolved in nitrohydrochloric acid at  $120^\circ\text{C}$  for 4 h. The final solution for the ICP-OES

analysis was prepared by adding a diluted nitric acid ( $\text{HNO}_3$ , 1 wt%) to a volume of 100 mL. The platinum contents of the GDE were also measured by ICP-OES analysis.

### 3.3.3 Brunauer-Emmett-Teller Surface Area Analysis (BET)

The surface area of the catalysts supports was performed by BET on an ASAP 2010 volumetric adsorption analyzer (Micromeritics, Norcross, USA) at 77.3 K.  $\text{N}_2$  adsorption–desorption–measurements were used for determination of the pore size distributions. The sample was degassed at 100 °C for 10 h under vacuum before the test. The specific surface area and the pore size distributions were determined according to the BET method in the relative pressure range of 0.05–0.2. The pore size distribution was determined from the desorption data.

The gas adsorption and desorption branches do not coincide with each other, forming a hysteresis loop with a specific shape. The characteristic of a hysteresis loop are dependent on the pore structure. IUPAC proposes four classification standard loops (H1, H2, H3, H4) and its corresponding pore type (Figure 3.1).

According to this classification, type H1 is often associated with porous materials exhibiting a narrow distribution of relatively uniform (cylindrical-like) pores. Materials that give rise to H2 hysteresis contain a more complex pore structure in which network effects (e.g., pore blocking/percolation) are important. Isotherms with type H3 hysteresis do not exhibit any limiting adsorption at high  $P/P_0$ . This behavior can for instance be caused by the existence of non-rigid aggregates of plate-like particles or assemblages of slit-shaped pores and in principle should not be expected to provide a reliable assessment of either the pore size distribution or the total pore volume. H4 hysteresis loops are generally observed with complex materials containing both micropores and mesopores. Both, types H3 and H4 hysteresis contain a characteristic step-down in the desorption branch associated with the hysteresis loop closure.

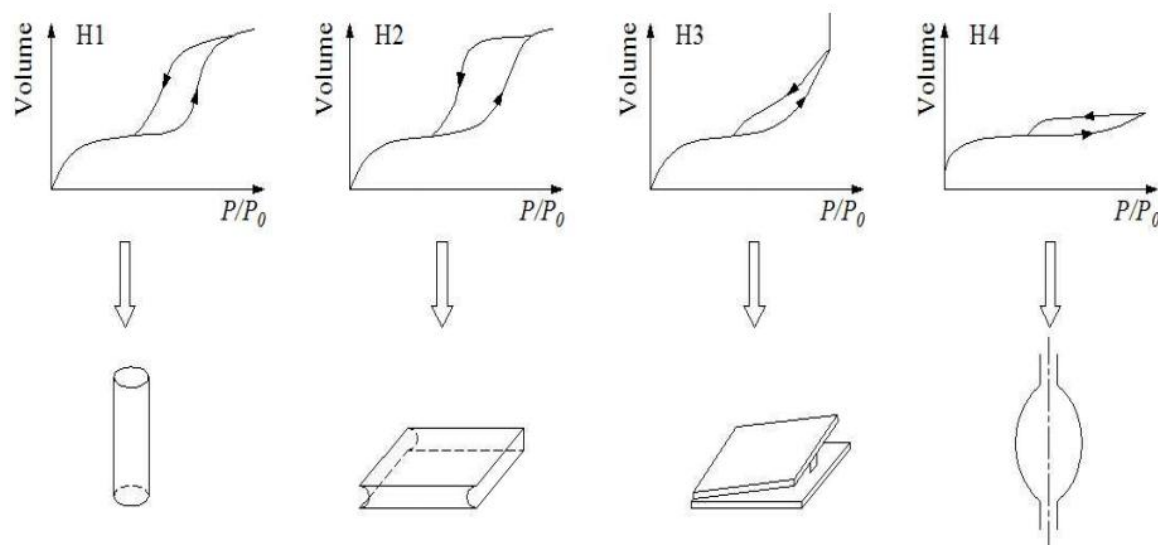


**Figure 3.1** Classification of hysteresis loops and pore types [235].

## 3.4 Spectroscopic Characterization

### 3.4.1 X-ray Photoelectron Spectroscopy (XPS)

XPS measurements can provide valuable information about the chemical composition and bond structure of carbon supports and the surface interaction between atoms. The XPS spectra were taken by means of a Thermo Scientific VG ESCALAB250 spectrometer (Thermo Scientific VG, East Grinstead, UK) with a monochromatic  $\text{AlK}_{\alpha 1/2}$ -source (1486.6 eV, 15 kV, 250 W). The XPS energy scale was calibrated by setting the binding energy of the carbon support to exactly 284.6 eV referenced to the Fermi level. The deconvolutions of the XPS spectra were carried out using CasaXPS software. The relative concentrations of the surface species are equal to the corresponding deconvoluted peak areas divided by the total XPS signal area extracted from the experimental XPS core level regions of N 1s.

### 3.4.2 Raman Spectroscopy

Raman spectroscopy is a powerful tool for characterizing ordered/disordered crystal structures of carbon materials. There are three main peaks, which are the G band at around  $1580\text{ cm}^{-1}$ , the D band at around  $1350\text{ cm}^{-1}$ , and the 2D band at  $2700\text{ cm}^{-1}$  [236]. The G band is from  $\text{sp}^2$  carbon atoms domains, corresponding to the first-order scattering of the  $E_{2g}$  mode. The D-mode is a disorder-activated Raman mode and is related to the vibrations of  $\text{sp}^3$  carbon atoms of disordered graphene nanosheets. The D band is usually observed at graphene edges. Previous studies showed that the position and shape of the second-order 2D-band are sensitive to the layers of graphene sheets [217, 218]. On the basis of this, the 2D band can be used to evaluate the number of layers of a multilayer graphene. Also, the intensity ratio of the D- and G-bands ( $I_D/I_G$ ) has been widely used to evaluate the quality of graphene nanosheets.

The Raman spectra were recorded with a Renishaw InVia Reflex micro-Raman system (Renishaw, Gloucestershire, UK) with a frequency doubled He:Ne laser (633 nm) as excitation source. The laser power measured on the sample surface is 17mW.

## 3.5 Electrochemical Characterization

### 3.5.1 Rotating Disk Electrode (RDE) Measurement

The oxygen reduction reaction can be observed in the kinetic and mixed diffusion-kinetic regions using the RDE technique. The kinetic current density can be derived from the Koutecky-Levich equation [237]:

$$\frac{1}{j} = \frac{1}{j_k} + \frac{1}{j_d} = \frac{1}{j_k} + \frac{1}{B\omega^{1/2}} \quad \text{Eq. 3.1}$$

$$j_k = n F k c \quad \text{Eq. 3.2}$$

$$B = 0.62 n F c D^{2/3} \nu^{-1/6} \quad \text{Eq. 3.3}$$

$j$ : measured current density,

$j_k$ : kinetic limiting current density,

$j_d$ : diffusion limiting current density,

$\omega$ : electrode rotation rate,

$n$ : the number of transferred electrons,

$F$ : Faraday constant,

$c$ : bulk concentration of O<sub>2</sub> dissolved in the electrolyte (1.26·10<sup>-6</sup> mol cm<sup>-3</sup>),

$D$ : diffusion coefficient for O<sub>2</sub> (1.93·10<sup>-5</sup> cm<sup>2</sup> s<sup>-1</sup>),

$\nu$ : kinematic viscosity in 0.1 M HClO<sub>4</sub> solution (1.01·10<sup>-2</sup> cm<sup>2</sup> s<sup>-1</sup>),

$k$ : rate constant

This equation has been widely used for analysing steady state reaction kinetics which is of first order with respect to the diffusing reactant.

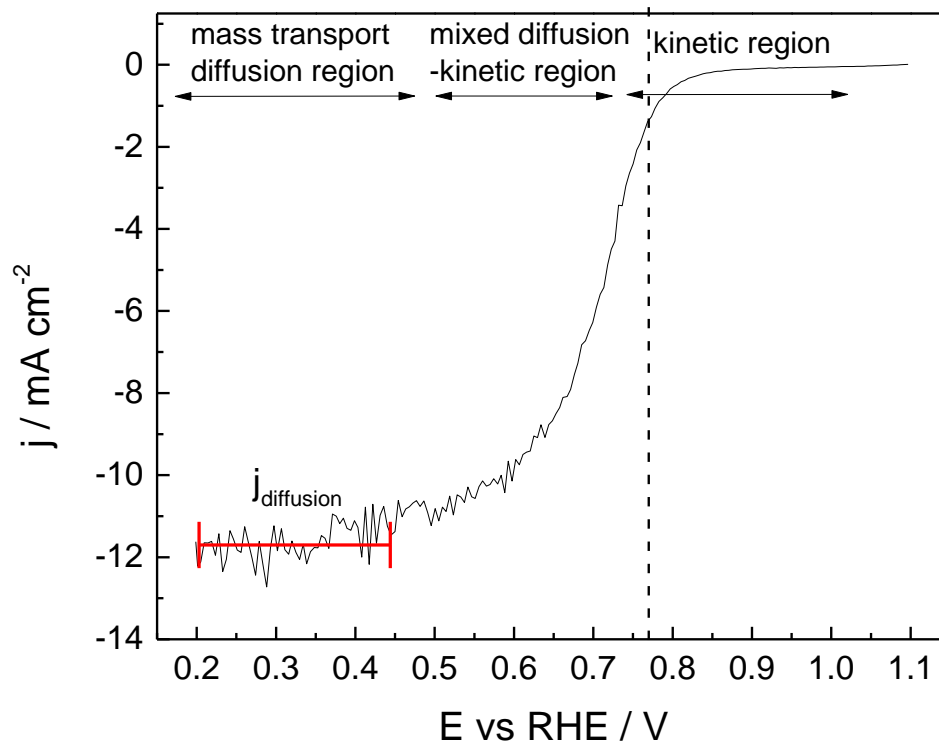


**Figure 3.2** Linear sweep voltammogram of Pt@C (0.2 – 1.1 V vs. RHE,  $5 \text{ mV s}^{-1}$ , 1600 rpm, saturated- $\text{O}_2$ , 0.1M  $\text{HClO}_4$ ).

The RDE measurements for the catalytic activity were performed in an oxygen-saturated 0.1M perchloric acid ( $\text{HClO}_4$ ) at  $25 \text{ }^\circ\text{C}$  with rotation speeds between 200 and 2000 rpm (cathodic scan speed:  $20 \text{ mV s}^{-1}$  between 1.08 and 0.1 V vs. RHE). A three-compartment electrochemical cell was used as a three electrode setup with a platinum wire as counter electrode and  $\text{Hg}/\text{Hg}_2\text{SO}_4/\text{sat. K}_2\text{SO}_4$  (Radiometer Analytical Ref621, Hach Lange GmbH Headquarter, Düsseldorf, Germany) as reference electrode. For the preparation of working electrodes, catalyst inks were prepared consisting of 24.2 mg carbon-supported platinum with 8.4 mL DI water, 3.6 mL ethanol and 1.2 mL of 10-times with DI water diluted 5 wt% Nafion<sup>®</sup> (Alfa Aesar GmbH & Co KG, Karlsruhe, Germany). Then their mixture was sonicated 3 times for 10 min at 5W with a Digital Sonifier<sup>®</sup> (Branson Ultrasonics, Danbury, USA).  $3 \text{ } \mu\text{L}$  of the ink was dropped onto the glassy carbon electrode ( $d = 3 \text{ mm}$ ) and dried at  $80 \text{ }^\circ\text{C}$  for 5 min. The measured reference electrode potential vs. NHE is 0.680 V. The measured ohmic resistance of the electrolyte between the working and reference electrode is 50 Ohm.

### 3.5.2 Electrochemical Impedance Spectroscopy (EIS)

EIS measurements were performed at a potential of -0.2 V to measure the interfacial processes and kinetics of electrode reactions of carbon supports in electrochemical system. Nyquist plots are shown in the form of imaginary ( $\text{Im } Z$ ) vs real ( $\text{Re } Z$ ) plots based on a frequency response analysis of frequencies ranging from 10 kHz to 100 Hz.

#### 3.5.2.1 Ex-Situ EIS Measurement

Ex-situ EIS measurements were performed to characterize the electronic conductivity of the prepared samples. The overall electronic resistance measured by EIS consists of a series of resistors located along the electron conduction path (Figure 3.3). Catalyst support particles are fixed with Nafion<sup>®</sup> on the surface of a glassy carbon sheet. The samples do not contain any platinum catalysts. The resulting ohmic resistance of the working electrode can be divided in two groups: transition resistances (among the catalyst support each other and catalyst supports-glassy carbon) and bulk resistances (glassy carbon, electrolyte, cable). Whereas the bulk resistance depends only on the material, the transition resistances depend as well on the used material as on some experimental parameters, like film thickness and Nafion amount. For these reasons the determination of the absolute catalyst support resistance is very challenging but a relative comparison of samples prepared in the same manner should allow the comparison of uncoated-/coated samples. In the present EIS measurement  $R_{CA}$ ,  $R_{CE}$ ,  $R_{EL}$ ,  $R_{NL}$  and  $R_{WE}$  are constant and the observed difference in resistance could be related to the ohmic resistance of the catalyst support ( $R_{CS}$ ).

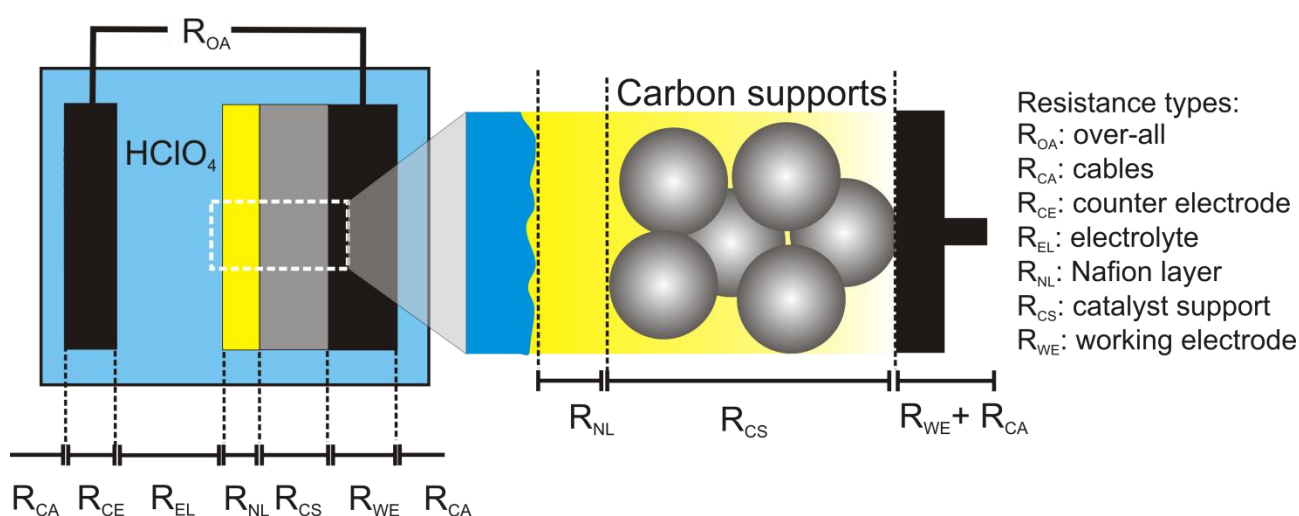
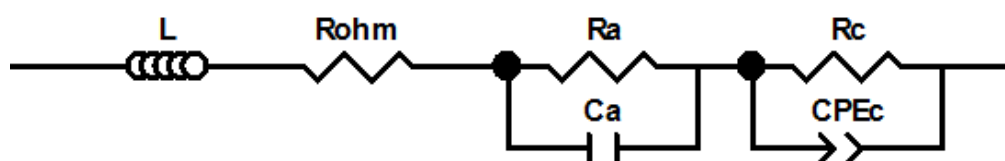


**Figure 3.3** Scheme of ex-situ electrochemical impedance spectroscopy.

### 3.5.2.2 In-situ EIS Measurement

In-situ EIS measurement in PEM fuel cells was performed under fuel cell conditions (AC amplitude:  $0.2 \text{ A cm}^{-2}$ ). Radov et al. [238] report that the overall electronic resistance is shown fitted with the model (Figure 3.4) which indicates the ohmic resistance of wires, electrodes, contacts and electrolyte. The anode and cathode reactions are described by charge transfer resistances in parallel with capacitances  $R_a/C_a$  and  $R_c/CPE_c$  (kinetic arcs), respectively. Constant phase element (CPE) is used accounting the distortion of the capacitance due to the electrode porous structure.



L – inductivity of wires

$R_{ohm}$  – ohmic resistance

$R_a$  – anode charge transfer resistance

$C_a$  – anode capacitance

$R_c$  – cathode charge transfer resistance

$CPE_c$  – cathode capacitance using constant phase element

**Figure 3.4** The equivalent circuit used for fitting of the EIS plots.

### 3.5.3 Cyclic Voltammetry (CV)

The ECSA was determined by hydrogen adsorption/desorption CV-measurements in  $N_2$ -saturated  $0.1 \text{ M HClO}_4$ . A platinum wire was used as counter electrode; and a hydrogen reference electrode (HydroFlex<sup>®</sup>, Gaskatel) as reference electrode. Working electrodes were prepared as follows: Before each experiment a glassy carbon disk electrode (diameter: 1.5 mm) was polished with 0.05 mm alumina suspension and cleaned with deionized water. For the preparation of catalyst inks, 2 mg of carbon-supported catalyst was first mixed in a 1 mL water:2-propanol mixture (1:2). Then 0.2 mg of Nafion<sup>®</sup> 117 (DuPont, Delaware, USA) was added and ultrasonicated for 30 min. 20  $\mu\text{L}$  of the ink was dropped onto the glassy carbon electrode and dried in the vacuum oven at  $50^\circ\text{C}$  for 1 h. Before electrochemical measurements were taken,  $N_2$  gas was purged in  $0.1\text{M HClO}_4$  electrolyte solution for 30 min. CV was then carried out for the detection of electrochemical process. It was performed in the range of 0.05 - 1.1 V (vs. RHE) at a scan rate of  $20 \text{ mV s}^{-1}$ .

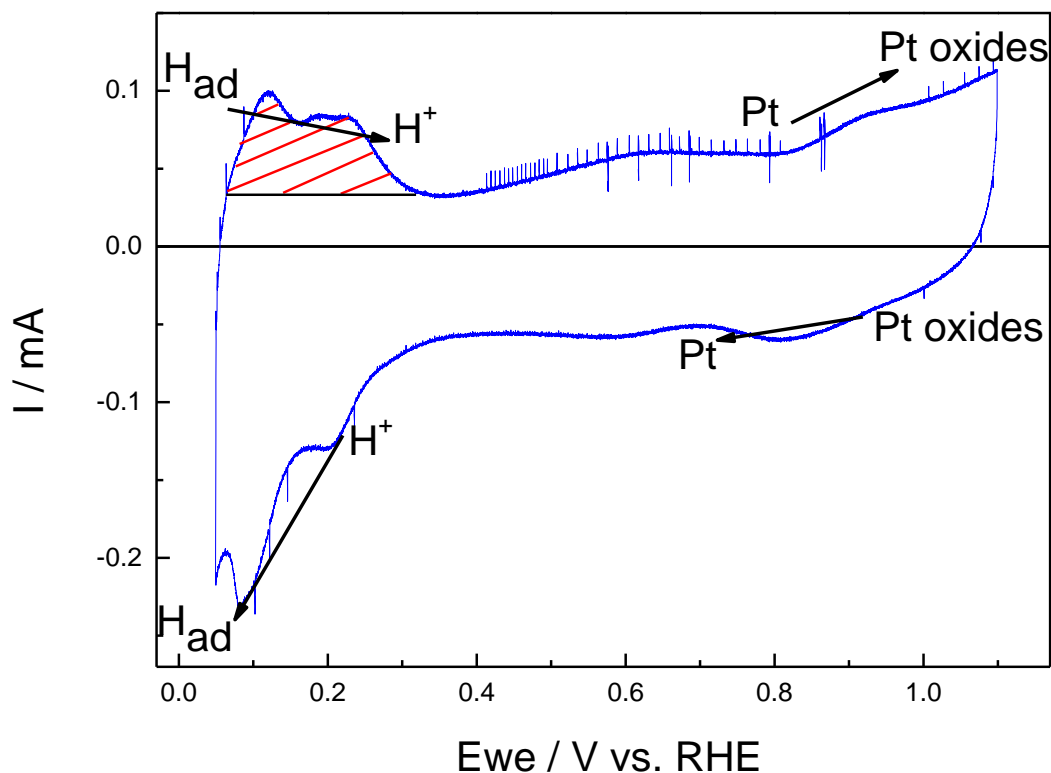


**Figure 3.5** CV of Pt@N-GF (0.05 – 1.1 V vs. RHE, 20 mV s<sup>-1</sup>, 0.1 M HClO<sub>4</sub>).

The platinum ECSA was calculated using the mean integral charge of the hydrogen adsorption/desorption area related to the platinum loading of the electrode. The specific platinum areas were determined by the integration of the hydrogen desorption peak related to the platinum loading of the electrode. The standard charge of 210 μC for 1 cm<sup>2</sup> platinum is assumed for the calculation of the specific platinum surface area by using Eq.3.2.

$$ECSA = \frac{Q_H}{210 \frac{\mu C}{cm^2} \cdot A \cdot l_{cat}} \quad \text{Eq.3.2}$$

ECSA – Electrochemically active surface area / cm<sup>2</sup>·mg<sup>-1</sup>

Q<sub>H</sub> – H-desorption charge / mC

A – electrode area / cm<sup>2</sup>

*l<sub>cat</sub>* – catalyst loading / mgPt·cm<sup>-2</sup>

### 3.5.4 Electrochemical Long-Term Stability Experiments

Two different CV test modes were used for electrochemical stability testing. These long-term stability tests are accelerated degradation tests to simulate the long-term behavior of fuel cell electrocatalysts. All experiments were conducted in N<sub>2</sub>-purged 0.1 M HClO<sub>4</sub> under air atmosphere at room temperature. The long-term behaviour of supported platinum catalysts was measured by an electrochemically accelerated degradation method according to Meier et al. [239]. This method characterizes the electrochemical active surface area by hydrogen adsorption/desorption CV measurements (0.05-1.1 V, 20 mV s<sup>-1</sup>, 0.1M HClO<sub>4</sub>).

In a multi-step CV test protocol carbon supported Pt catalysts were cycled in the following way:

1. 10 cycles (20 mV s<sup>-1</sup>) between 0.05 to 1.1 V (vs. RHE)
2. 500 cycles (100 mV s<sup>-1</sup>) between 0.4 to 1.4 V (vs. RHE)
3. 10 cycles (20 mV s<sup>-1</sup>) between 0.05 to 1.1 V (vs. RHE)
4. 500 cycles (100 mV s<sup>-1</sup>) between 0.4 to 1.4 V (vs. RHE)
5. 10 cycles (20 mV s<sup>-1</sup>) between 0.05 to 1.1 V (vs. RHE)
6. 500 cycles (100 mV s<sup>-1</sup>) between 0.4 to 1.4 V (vs. RHE)
7. 10 cycles (20 mV s<sup>-1</sup>) between 0.05 to 1.1 V (vs. RHE)

After 500, 1000 and 1500 voltage cycles the CV measurements were reformed in order to determine the platinum ECSA. It is expected to provide a guideline for developing a time-efficient and reliable test protocol for screening durable candidate support materials for PEMFC catalysts. The results of the CV measurements can be transferred to the specific platinum areas by the integration of the hydrogen desorption peak. A value of the platinum surface area is calculated by using Eq.3.2.

### 3.5.5 Membrane Electrode Assembly Testing

The MEAs were tested in a Biologic fuel cell test station (Bio-Logic, Claix, France). All measurements were carried out in hydrogen/oxygen mode at 60 and 80 °C with a constant hydrogen lambda of 1.2 and a constant oxygen lambda of 1.5. In conventional PEMFC, the operating temperature is kept at temperatures < 90 °C because the proton conductivity of the Nafion<sup>®</sup> membrane is strongly dependent on the membranes's water content.

Water content of the MEA and the GDL has an effect on overpotentials and loss mechanisms, and the cell performance could be affected negatively by both drying and flooding. Water is also produced during the electrochemical reaction at the cathode. Without proper water management, liquid water may accumulate in the porous materials and block the reactant gases from reaching

the catalyst sites. Due to the influence of water management the present experiments were tested at different conditions of humidification. The relative humidity for the anode and the cathode was set to 95% and 70%.

Polarisation curves were taken in galvanostatic mode with a hold time of 5 min per step.

## 4. Experimental

### 4.1 Materials

Several of the support materials used in this thesis are listed: carbon black (Ensaco<sup>®</sup> 150G), commercial graphene (AO-2) and CNT (Buytubes<sup>®</sup>), self-prepared multilayer graphene foams (GF), nitrogen-coated multilayer graphene foams (N-GF), nitrogen-coated graphene (N-G) and nitrogen-coated CNT (N-CNT). Table 4.1 summarizes the suppliers, dimensions and the BET surface areas of the catalyst supports.

**Table 4.1** Carbon supports for Pt catalyst.

Support	Supplier	Diameter / nm	BET / m <sup>2</sup> g <sup>-1</sup>
Ensaco <sup>®</sup> 150G	Timcal	45 (μm)	50
Graphene AO-2	Graphene Supermarket	3.2	77.1
CNT baytubes <sup>®</sup> C150 P	Bayer	4.1	172.3
GF	Self-prepared	1.6	477
N-GF	Self-prepared	1.6	833
N-G	Self-prepared	1.6	182.9
N-CNT	Self-prepared	1.4	392

For preparation of carbon supports, sodium ethoxide (95%, Sigma-Aldrich, Munich, Germany), commercial graphene (AO-2, Graphene Supermarket, Calverton, New York) and multi-walled carbon nanotubes (Baytubes C150 P, Bayer, MaterialScience AG, Germany) were used as a carbon-precursor. 1-Ethyl-3-methylimidazolium dicyanamide (EMIM-dca, BASF AG, Ludwigshafen, Germany) was used as a nitrogen source for a thermal decomposition process.

The catalysts were prepared by electrochemical reduction of hexachloroplatinic acid (40 wt% Pt, H<sub>2</sub>PtCl<sub>6</sub>·6H<sub>2</sub>O, Umicore, Hanau, Germany) dissolved in a Nafion<sup>®</sup> solution (20 wt%, DuPont, Delaware, USA) containing polytetrafluoroethylene particles (PTFE, Sigma-Aldrich, Munich, Germany). The prepared gas diffusion electrodes (GDE) with a platinum loading of 0.4 mg Pt cm<sup>-2</sup> were used as anode. A commercial cathode (type ELE 0162, Johnson Matthey, London, UK), a Nafion<sup>®</sup> 212 (DuPont, Delaware, USA) membrane and the self-made anode were used for the MEA.

## 4.2 Preparation Methods

### 4.2.1 Preparation of GF

The hierarchical structured GF was prepared by a thermal decomposition of sodium ethoxide, illustrated in Figure 4.1. In a first step NaOEt was decomposed at 800 °C for 1 min in the box furnace. The result powder, subsequently, was crushed, ultrasonicated and washed in deionized water to remove residual sodium oxides. Finally the samples were dried in an oven at 80 °C.

### 4.2.2 Preparation of N-GF

As a nitrogen source EMIM-dca was used for N-GF formation. In step 2 the prepared GF was impregnated with EMIM-dca followed by a second heating process at 600 °C for 1 min in air (step 3).

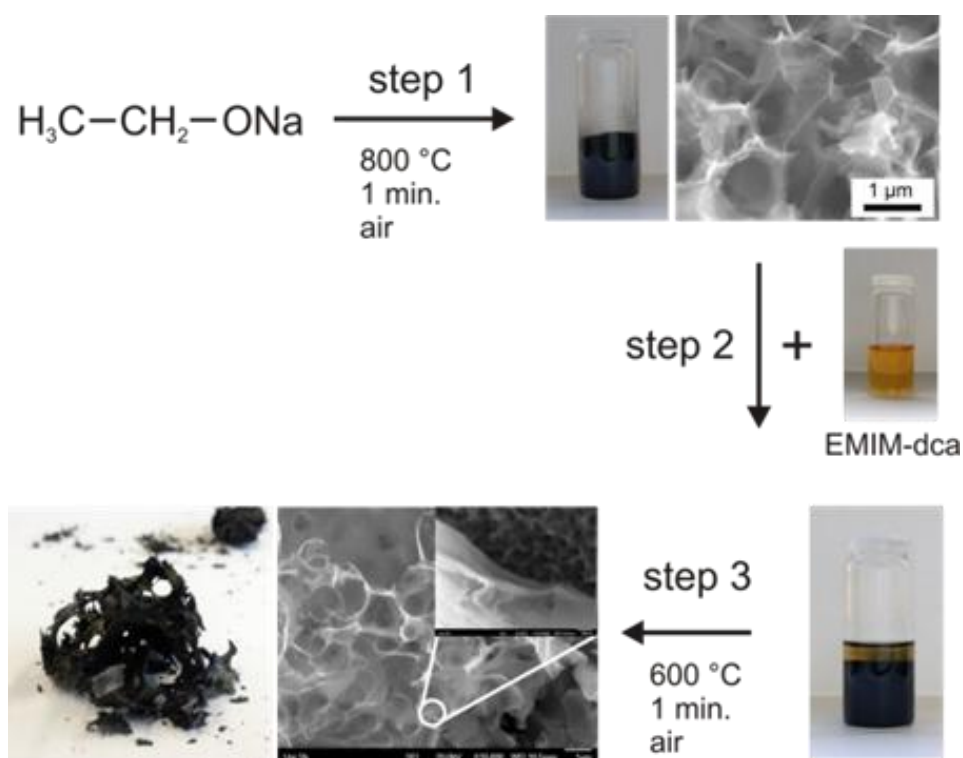


**Figure 4.1** Illustration for the synthesis of hierarchical structured multilayer graphene foams coated with N-containing carbon layers.

### 4.2.3 Preparation of N-G and N-CNT

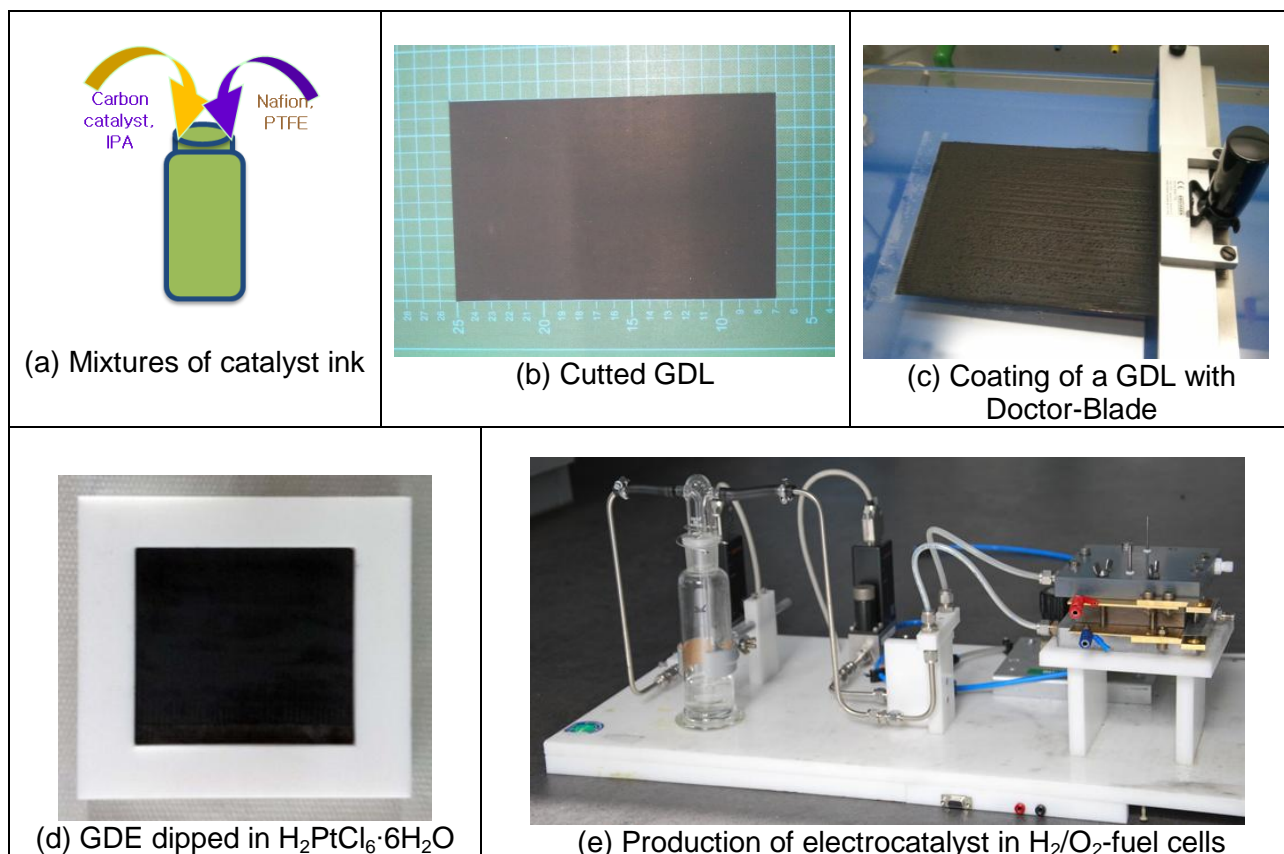
Nitrogen coated-graphene (N-G) and –CNT (N-CNT) samples were prepared by thermal surface modification using nitrogen containing ionic liquids. For coating the carbon structures graphene or CNT was first mixed with EMIM-dca and heated up to 600 °C for 1 min. Different ratios of graphene/CNT to ionic liquids (5, 10 and 15 wt%) were used for the surface coating process.

### 4.2.4 Chemical Preparation of Catalysts

The carbon-supported platinum catalyst was prepared by thermally-induced chemical reduction. 0.49 g hexachloroplatinic acid (40 wt% Pt,  $\text{H}_2\text{PtCl}_6 \cdot 6\text{H}_2\text{O}$ , Umicore, Hanau, Germany) was dissolved in 140 mL  $\text{H}_2\text{O}$ . This solution was added to an aqueous suspension of 1.26 g GF, N-GF, pure graphene, pure CNT, N-G, or N-CNT in 560 mL ethylene glycol under vigorous stirring. The resulting mixture was heated at 120 °C for 24 h. The resulting product was washed with ethanol and centrifuged at 4500 rpm for 30 min. The residue was dried in an oven. The final product was analyzed with respect to its exact platinum content by inductively coupled plasma - optical emission spectroscopy (ICP-OES). The platinum loading of Pt@GF, Pt@N-GF, Pt@G, Pt@CNT, Pt@N-G or Pt@N-CNT powders is 32.2 wt%, 7.7 wt%, 35.5 wt%, 12.6 wt% and 2.5 wt%, respectively.

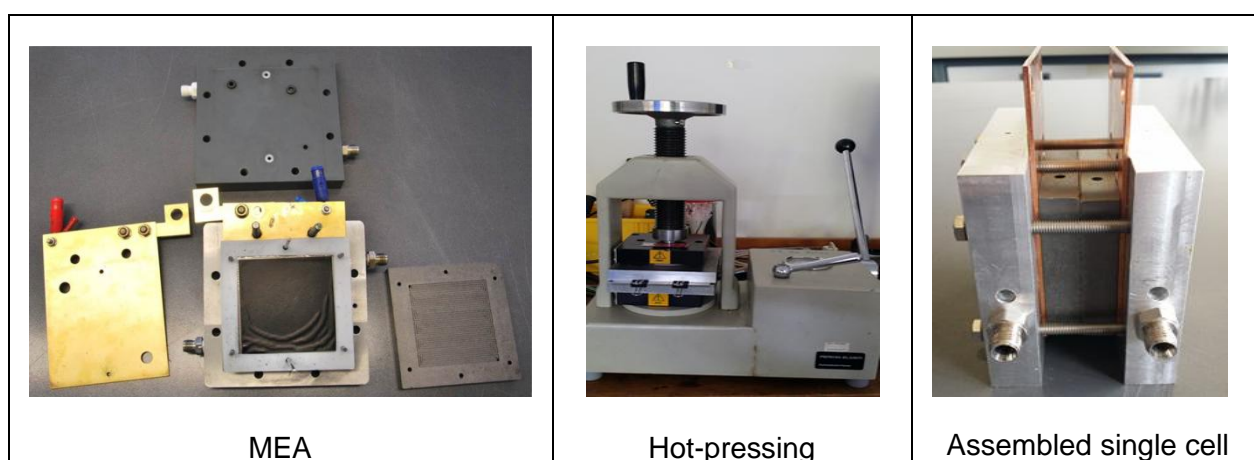
### 4.2.5 Electrochemical Preparation of Catalysts

The supported catalysts were prepared by electrochemical reduction. 450 mg of carbon precursor, 0.24 mL of Nafion<sup>®</sup> solution (20 wt%, DuPont, Delaware, USA) and 0.204 mL of polytetrafluoroethylene particles (PTFE, Sigma-Aldrich, Munich, Germany) in 20 mL of 2-propanol were mixed (a) under ultrasonication for 1 h. A commercial GDL (TGP-H-090, Toray Industries Inc, Shiga Plant, Japan) was coated on a geometric area of 400 cm<sup>2</sup> (10 cm x 40 cm) (b) with 20.69 mL of the resulting carbon ink using a 180 μm doctor blade (speed: 5 mm s<sup>-1</sup>) (c). The electrodes were dried overnight at 60 °C and cut to the electrode size of 50 cm<sup>2</sup> (71 cm x 71 cm). The prepared GDE was dipped in a solution of 66.6 mg  $\text{H}_2\text{PtCl}_6$  in 2 mL 2-propanol (d) and dried in a vacuum oven at 40 °C. The platinum precursor was reduced electrochemically with SP150 potentiostat with a VMP3B-10 amplifier 10A/20V (Bio-Logic, Claix, France) (e) according to a procedure reported elsewhere [240].



#### 4.2.6 Preparation of MEAs

The resulting MEAs consist of the self-made anode, a commercial cathode (ELE0162, Johnson Matthey Royston, London, UK) with a platinum loading of  $0.4 \text{ mgPt cm}^{-2}$  and a Nafion<sup>®</sup> 212 (DuPont, Delaware, USA) membrane. The final geometric area is  $12 \text{ cm}^2$  ( $35 \text{ cm} \times 35 \text{ cm}$ ). The MEAs were prepared by hot-pressing at  $125 \text{ }^\circ\text{C}$  with a pressure of  $0.5 \text{ kN cm}^{-2}$  for 6 min.



## **5. Hierarchical Structured Multilayer Graphene Foams (GF) Coated with Nitrogen-Containing Carbon Layers (N-GF)**

Hierarchical structured multilayer graphene foams coated with nitrogen-containing carbon layers [242] have recently been explored as a promising support material for improving the performance of electrocatalytical processes. Figure 5.1 illustrates the structure of the new catalyst support architecture. This special structural material design is very suitable for processes in which the diffusion of educt/products and also the electronic conductivity are the limiting reaction steps (e.g. catalyst supports for fuel cell applications). The architecture of the composite system promises four main advantages:

1. The 3D-structures of the macro-/microporous GF and the meso-/microporous N-GF enable a very good transport of educts and products from and to the reaction sides. Therefore mass transport problems were decreased.
2. The microstructured N-GF surface enables a highly dispersed distribution of nanoparticles, like catalysts or other auxiliary materials.
3. The microstructure of the GF surface increases the adhesion of the N-GF coating and decreases the ohmic resistance between the coating and the base material.
4. The electronic conductivity of the microporous N-containing carbon coating is beneficial for all kinds of reactions in which electron transport processes are involved.

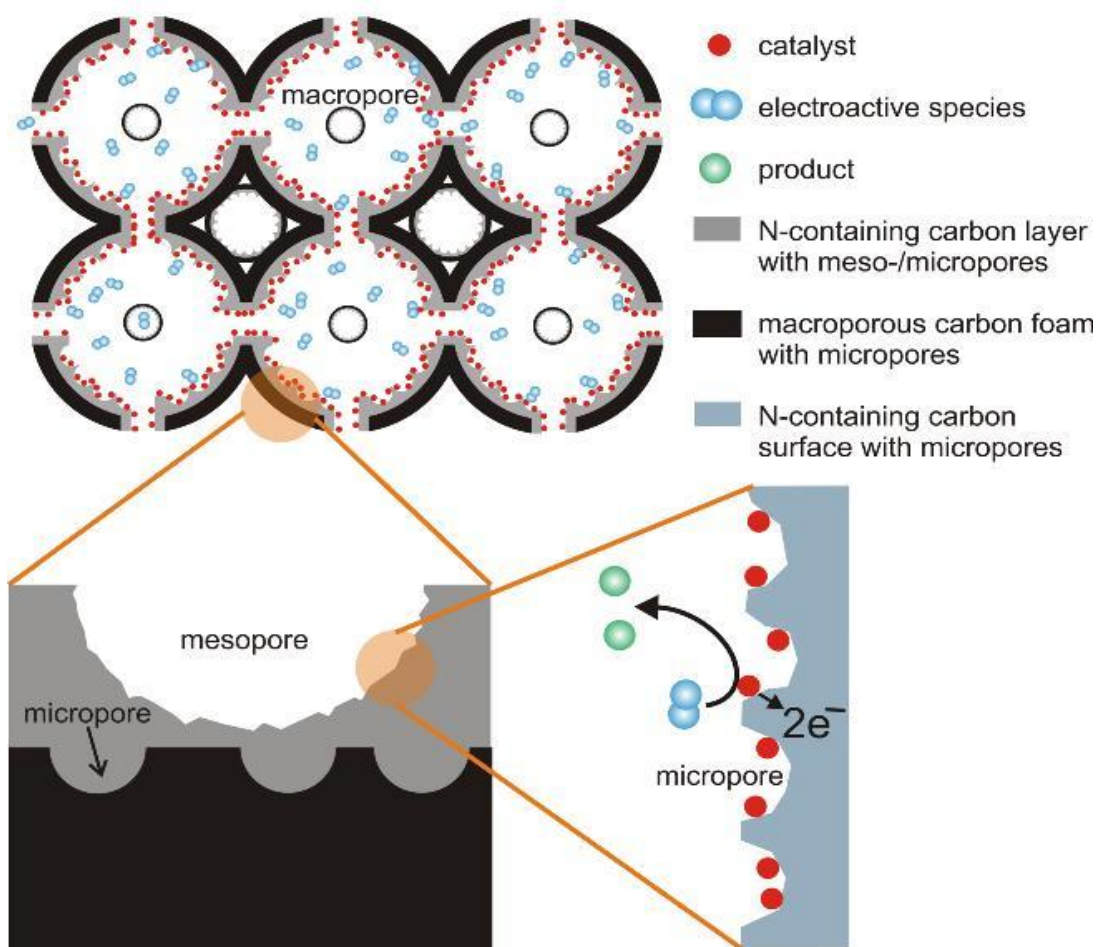


**Figure 5.1** Scheme of the new hierarchically structured carbon foam concept used for electrocatalytical processes.

## 5.1 Results

### 5.1.1 Chemical Composition of GF and N-GF

The influence of the heating temperature and the IL content on the product composition was optimized in a temperature range between 550 and 800°C (Table 5.1). It was found that 600°C is the optimal temperature for the thermal decomposition: below this temperature yellow reaction products are observed and above the IL decompose and forms gaseous products. The resulting product was characterized by CHN analysis to determine its exact nitrogen content.

The nitrogen content of the N-GF system should be controlled by the chemical composition of the used IL that means the given atom ratio of carbon to nitrogen. EMIM-dca consists of 33.4 at% (54.2 wt%) carbon, 20.8 at% (39.5 wt%) nitrogen and 45.8 at% (6.3 wt%) hydrogen, respectively.

The amount of nitrogen in the final product depends on the proper choice of the process parameters (e.g. T, pyrolysis time, IL-content) shown in Figure 5.2 and Table 5.1.

The GF prepared at 800 °C has a carbon content of 84.96 wt%, negligible H and N contents and an oxygen content of 14.98 wt%. This relatively high oxygen amount results from the pyrolysis process in air. The CHN analysis of pure IL pyrolysed at different temperatures shows decreased N-contents (Figure 5.2b), and nearly constant carbon (Figure 5.2a) and oxygen contents by increasing temperatures. For this reason low temperatures are preferred for the synthesis of the coated foams. The optimization of the IL:GF-ratio ( $IL_R$ ) was done by pyrolysing samples with  $IL_R$  values of 5, 10 and 15 (Table 5.1). It can be seen that the N content of the N-GF samples increases with increasing  $IL_R$ . A  $IL_R$  of 15 generates coatings with a N content which is very close to the theoretical value (39.5 wt%). The N content of N-GF prepared at different temperatures shows the same behaviour like the pyrolysed pure ILs, but the carbon content of the products increases. An explanation for these results are an enhanced reaction of oxygen with the N containing parts of the IL molecule which could be caused by a thin film formation of the IL on the pores surface. An IL film thickness of about 100 nm results from an estimation assuming a uniform pore size and uniform IL distribution in the pores. From this optimization of the synthesis it could be shown that N-GF with a nitrogen content of 35.31 wt% was obtained at 600 °C with an  $IL_R$  of 15. Lower synthesis temperature leads to incompletely reacted yellowish products. To the best of our knowledge, this is the first synthesis of a hierarchical structured porous N-GF with a very high nitrogen amount.

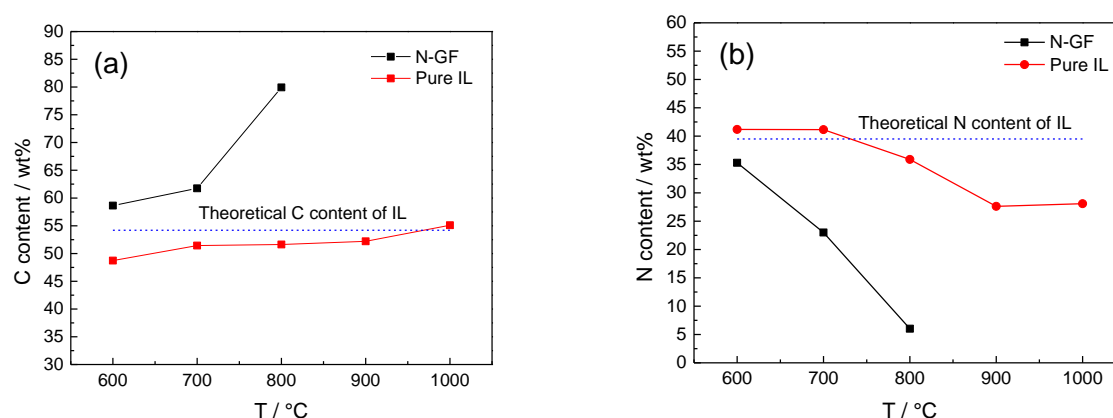


**Figure 5.2** Element compositions of the pure IL and N-GF prepared with different EMIM-dca contents and temperatures.

**Table 5.1** Element compositions of the GF and N-GF prepared with different EMIM-dca contents and temperatures.

Sample	GF:IL ratio	Temperature [°C]	C content [wt%]	H content [wt%]	N content [wt%]
GF	-	800	84.96	0.01	0.05
N-GF	1:5	600	72.49	0.01	21.93
N-GF	1:10	600	65.34	0.01	28.95
N-GF	1:15	600	58.64	1.23	35.31
Pure IL	-	600	48.72	2.11	41.18
N-GF	1:15	700	61.75	0.01	23.01
N-GF	1:15	700	51.43	1.57	41.15
N-GF	1:15	800	79.94	0.01	6.02
Pure IL	-	800	51.62	0.01	35.89
Pure IL	-	900	52.19	1.30	27.62
Pure IL	-	1000	55.10	0.01	28.08

### 5.1.2 Morphology and Structure of GF and N-GF

An overview scanning electron micrograph of the resulting GF and N-GF samples is displayed in Figure 5.3. Figure 5.3a,b show the morphologies of GF. As shown in Figure 5.3b the pore size of the macro pores is about 800 nm to 1  $\mu\text{m}$ . The final N-GF product is shown in Figure 5.3c,d. It can be seen that the initial pore structure of GF remains intact without any structural changes (Figure 5.3c). The mesoporous structure of the N-GF is given in Figure 5.3d. The diameter of the mesopores is 60 to 100 nm.

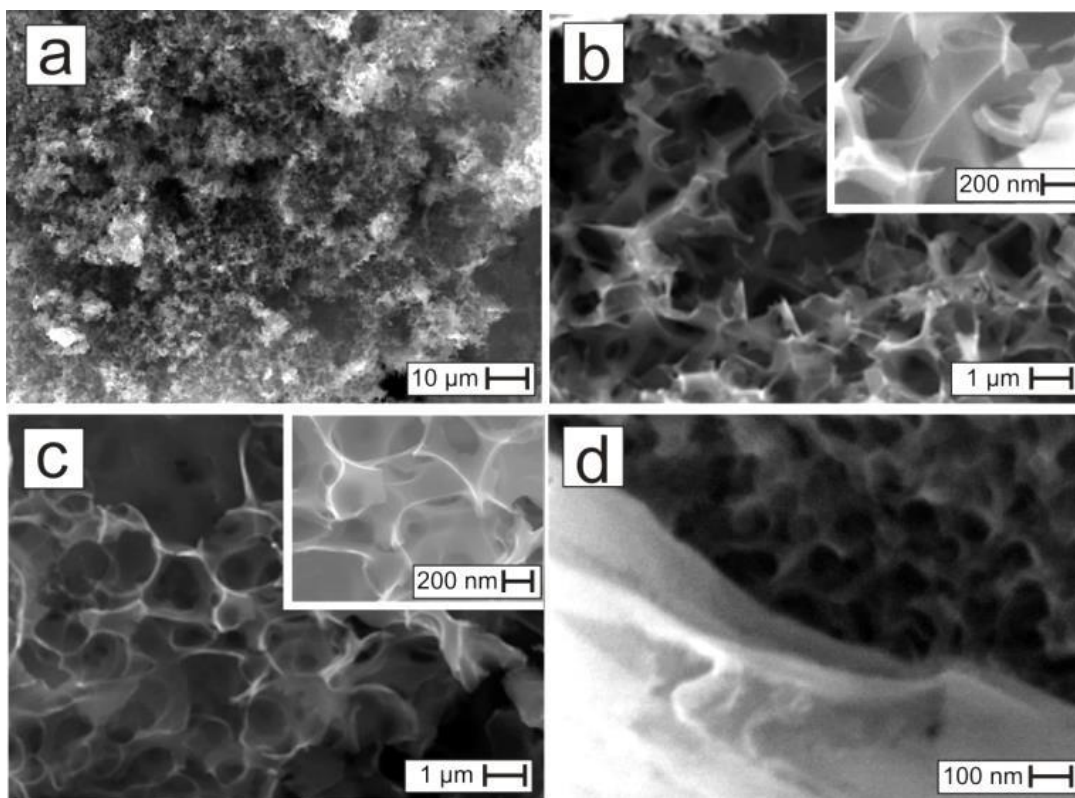


**Figure 5.3** Morphology and structures of GF and N-GF. (a,b) SEM images of GF (scale bars: 10 μm, b: 1 μm and insert 200 nm); (c) SEM images of N-GF (scale bars: 1 μm, insert: 200 nm); (d) SEM image of N-GF (scale bar: 100 nm).

An examination of the GF and N-GF structure was done by TEM and EDX analysis. TEM images (Figure 5.4) for the GF and N-GF samples show a thickness of the foam wall of ~5 nm which corresponds to 13-15 mono layers. High-resolution TEM (Figure 5.4a) reveals a microporous structure with a very narrow pore size distribution. The diameter of the pores is about 1 to 2 nm. A higher magnification of the mesoporous N-GF surface shows a uniformly microporous structure (Figure 5.4b) with a pore diameter of about 0.5 to 1 nm. Cross section of N-GF pore lamella (Figure 5.4c) and high-resolution topview of the coated GF lamella are presented (Figure 5.4d). The pore wall thickness of the GF is about 11.4 nm and the thickness of the N-GF is about 4 to 6 nm. A nitrogen content of 30.4 wt% and an oxygen content of 1.2 wt% were measured by EDX analysis.

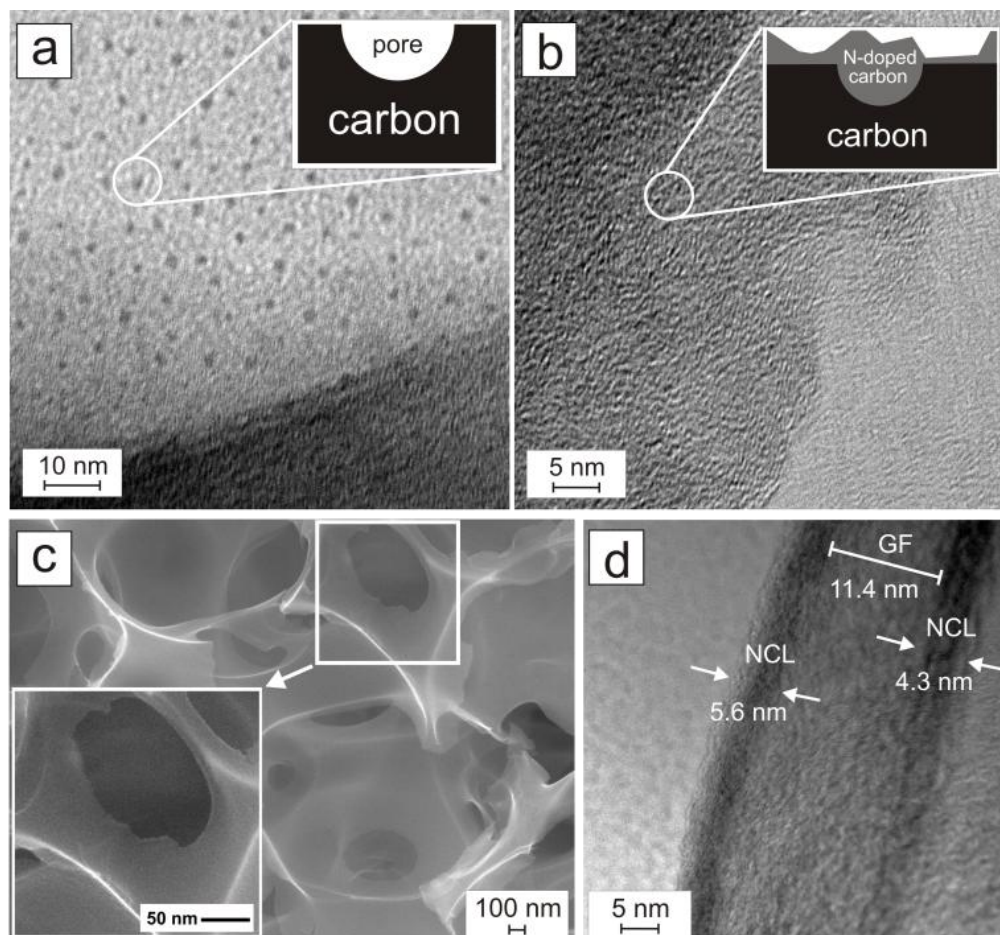


**Figure 5.4** TEM images of the surfaces of GF (a) and N-GF (b) show the microporous structure. The inserted schemes illustrate their surface structures before and after the coating process. Cross section of a N-GF pore lamella (c) and a high-resolution TEM of the coated GF (d).

### 5.1.3 Characterization of GF and N-GF

#### 5.1.3.1 BET Characterization

The specific surface area and pore size distribution were calculated by BET nitrogen gas adsorption. The BET surface has  $477 \text{ m}^2 \text{ g}^{-1}$  of GF and  $833 \text{ m}^2 \text{ g}^{-1}$  of N-GF. In the pore size distribution plot of micro pores (Figure 5.5d), the majority of pores in these materials have a diameter of  $\sim 1 \text{ nm}$ , which are classed as micro pores. The specific surface areas of GF and N-GF are significantly higher than that of commercial graphene samples, like AO-2 (Graphene supermarket, Calverton, New York) with a flake diameter of  $5.3\text{--}8.0 \mu\text{m}$  [241]. It has a BET surface area of  $100 \text{ m}^2 \text{ g}^{-1}$ , and an averaged pore diameter of  $1.6 \text{ nm}$ . Thus, it is observed that the large surface area of N-GF (Figure 5.5c) can lead to a large ORR triple-phase boundary.

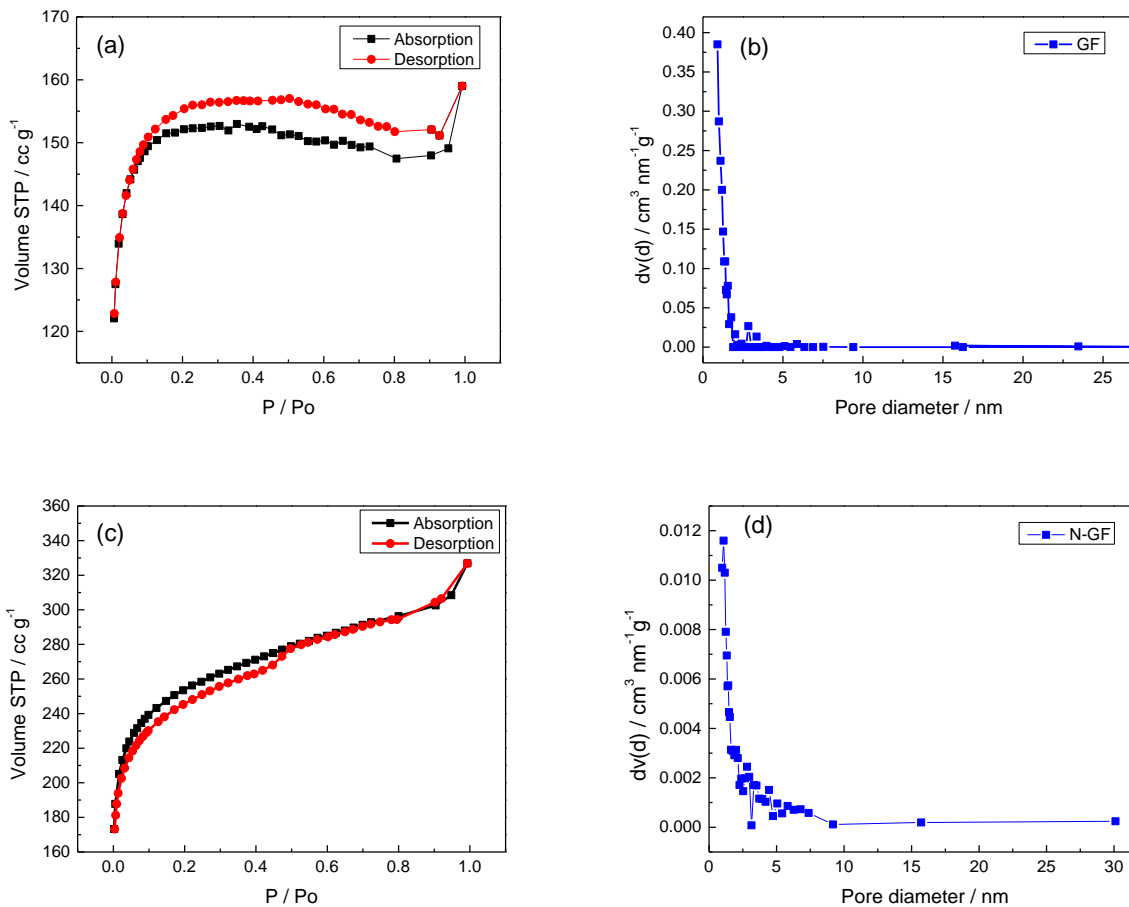


**Figure 5.5** The specific surface area and pore size distribution of GF and N-GF. BET isotherms of GF (a) and N-GF (c); Pore-size distribution of the GF (b) and N-GF (d) measured by nitrogen adsorption–desorption.

### 5.1.3.2 XPS Characterization

XPS measurements were performed to determine the chemical composition of GF and N-GF and to characterize the carbon, nitrogen, and oxygen species. The XPS overview spectrum (Figure 5.6a) of the GF sample shows signals of C 1s, O 1s and a small one of Na 1s, Na KLL and O KLL whereas the N-GF sample has an additional signal of N 1s. The small amount of detected sodium results from sodium hydroxide (side product resulting from sodium ethoxide pyrolysis) which is located in closed pores and could not be washed out.

The C 1s spectrum of GF (Figure 5.6b) can be described with three different signals at 284.5, 285.3 and 288.9 eV. The main peak at 284.5 eV can be attributed to sp<sup>2</sup> carbon of the graphene-like GF carbon matrix, and the two smaller ones with a higher binding energy to C-OH (285.3 eV) and C=O (288.9 eV) species. Compared with the spectrum of the GF sample the C 1s spectrum of

N-GF is more complex. Additional to the main  $sp^2$  carbon peak at 284.5 eV we observe three further carbon species at binding energies of 285.9, 286.9 and 288.5 eV. Well known species of N-containing carbon materials [243-245], like pyridinic-N (398.7 eV), pyrrolic-N or oxidized pyridinic-N (400.3 eV), and graphitic-N (401.4 eV) are not sufficient to explain the high nitrogen content of 35.31 wt%. For this reason we assume the existence of a nitrogen rich compound, like  $C_3N_4$  as reported by Chen et al. [246]. The remaining C 1s signals of N-GF (Figure 5.6d) can be attributed to C-N (284.7 eV), C=N (285.9 eV) and N-C=N (288.5 eV) species resulting from the structure of  $C_3N_4$ . The N 1s spectrum of N-GF (Figure 5.6e) can be fitted with four individual peaks at 398.39, 400.10, 401.11 and 404.47 eV. The signal with the lowest binding energy could be attributed to two different N species: the aromatic C=N-C bonds of the  $C_3N_4$  structure and the pyridinic-N. Due to the very close peak position it is not possible to separate the corresponding N species without further information. One additional signal at 400.1 eV matches the N-(C)<sub>3</sub> species and another signal at 401.11 eV the C-N-H groups of the  $C_3N_4$  structure [245, 247]. One remaining peak with a low intensity was observed at 404.47 eV. Ong et al. found this typical signal in  $C_3N_4$  heterocycles and attribute it to positive charge localizations [246]. The pyrolysis product of EMIM-dca should have a carbon content of 54.1 wt% and a nitrogen content of 39.5 wt%. For the formation of standard N species (pyrrolic-, pyridinic- or graphitic-N) nitrogen contents between 4 and 11 wt% were reported in the literature [248, 249]. For this reason the prepared coating is supposed of consisting of a nitrogen rich compound or a mixture of different nitrogen containing compounds. The pyrolysis product of the IL molecule with the molecular formula of  $C_8H_{11}N_5$  could be theoretically split in  $C_5N$  and  $C_3N_4$ . The  $C_3N_4$  compound consist of a carbon content of 39.13 wt% and an nitrogen content of 60.87 wt%, and the  $C_5N$  compound of a carbon content of 81.13 wt% and a nitrogen content of 18.87 wt%. According to the carbon and nitrogen ratio we assume that the two compounds occur in the product with a ratio of about 50:50, corresponding to a nitrogen content of 41.40 wt% and a carbon content of 57.14 wt%. This result is quite similar to the present CHN analysis (N: 35.31 wt%, C: 58.64 wt%). The remaining difference in C-content of 1.46 wt% can be attributed to oxygen species which were formed during the pyrolysis in air. For this reason we measured the oxygen species by XPS. Both, GF and N-GF samples show signals in the O 1s spectrum (Figure 5.6c, f). The peaks originate from oxygen species (531.6 eV: C=O, 535.1 eV: C-OH, C-O-C) formed during the pyrolysis process in air. The existence of N-C=N, N-(C)<sub>3</sub>, and C=N-C as components of heptazine which are subunits of  $C_3N_4$  confirms our assumption of  $C_3N_4$  formation. In combination with the CHN analysis we postulate a coexistence of pyridinic-N and  $C_3N_4$  species. From the structural point of view, we assume that the two species are arranged in disordered domains because the two species were formed simultaneously and not one by one.

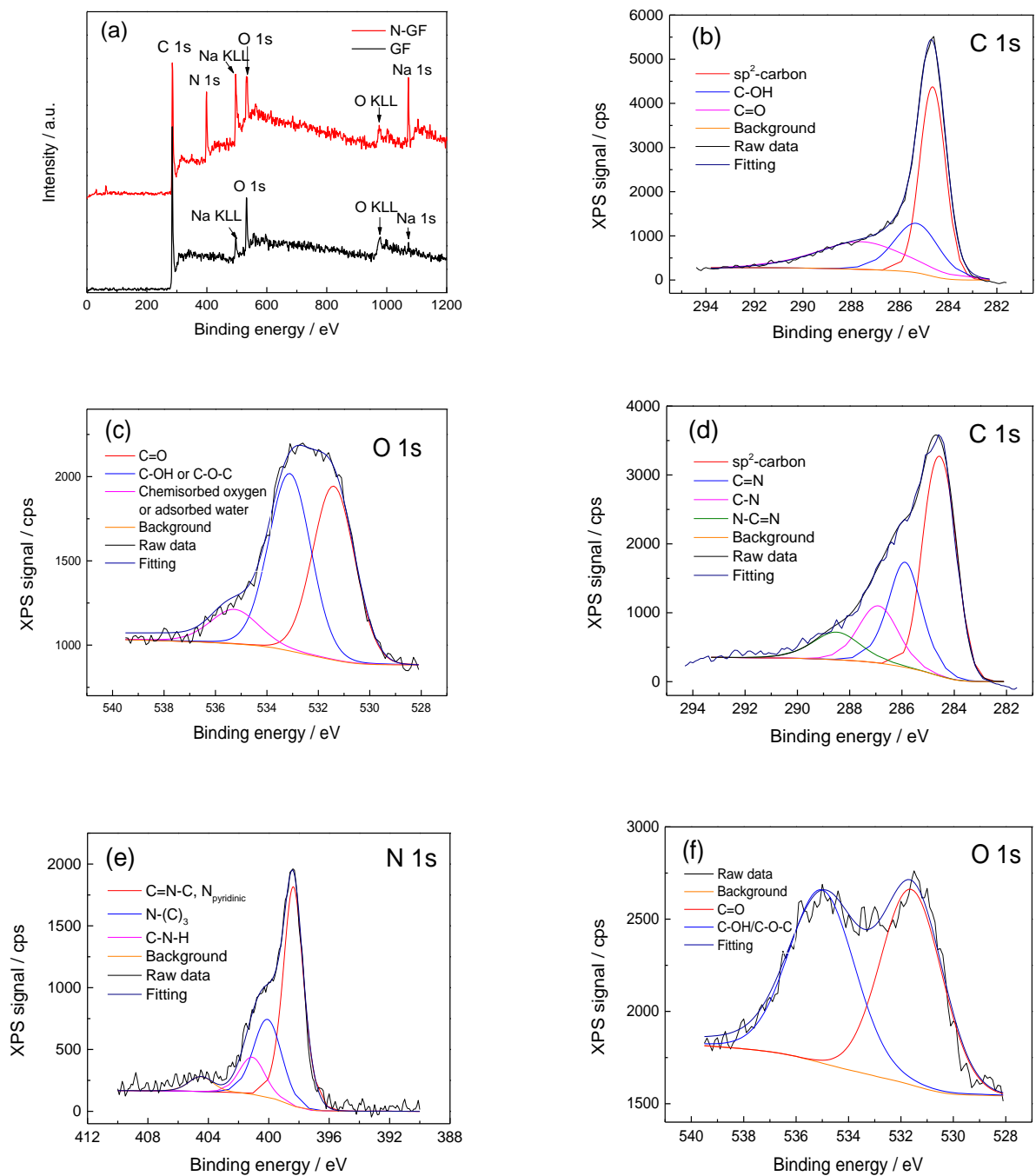


**Figure 5.6** Characterization of GF and N-GF by XPS. (a) XPS survey spectra of GF (black curve) and N-GF (red); (b,c) High-resolution of C 1s XPS spectra (b) and O 1s spectra (c) of the GF; (d-f) High-resolution C 1s XPS spectra (d), N 1s spectra (e) and O 1s spectra (f) of the N-GF.

### 5.1.3.3 XRD Characterization

The crystallinity, the domain size and the structure were measured by XRD (Figure 5.7). For the GF sample we found broad Bragg reflections around 24.9 and 42.3 degree ( $2\theta$ ). The occurrence of such broad peaks indicates the presence of very small crystalline domains in the range of less than 10 nm. Standard diffraction angles of 26.228 (002), 42.214 (100) and 44.365 (101) degree were reported in the literature (powder diffraction file data base, file 75-1621). The (002)-reflection corresponds to the interlayer spacing (c-axis) and the (100) reflection to the interplanar atomic distance in the a- and b-axis. Although the peak positions are difficult to determine it can be clearly seen that the (002)-reflection of GF is slightly shifted to smaller angles whereas the (100)- and (101)-peak are not shifted (Figure 5.7a). The slight shift of the (002)-peak could be explained by the nanocrystalline and also by the porous structure [250, 251] of the GF. The large content of grain boundaries with amorphous structure leads to an expansion of the interplanar distance in (002)-direction whereas the microporous structure leads to the formation of small nanocrystalline domains. Compared to the GF sample the XRD pattern of N-GF shows several remarkable differences: the (002)-peak width is about 31% smaller, shifted to higher angles and the shape is asymmetric on the left side. For the polycrystalline compounds diffraction angles of 24.2 and 43.6 were reported for  $C_5N$  [252] and 26.505 and 46.191 for  $C_3N_4$  [253], respectively (Figure 5.7b). Similar peak positions for  $C_3N_4$  (27.4 and 44.5 degree) were reported by Yuan et al. [252]. In the present XRD data, the diffraction pattern of N-GF has to be considered, that means the measured data are a convolution of  $C_5N$ ,  $C_3N_4$  and GF. The radius of incorporated nitrogen causes a reduction of the graphitic interlayer spacing because the nitrogen atom (67 pm) is slightly smaller than that of carbon atoms (70 pm). For this reason graphitic structures with high nitrogen content cause a high angle shift of the corresponding Bragg reflection. The existence of a second nitrogen containing species,  $C_5N$ , can be used to explain the asymmetry on the left side of the (002)-peak at a diffraction angle of 22.7 degree. The increased crystallinity may result from the pyrolysis- and crystallization behaviour of the used IL. It could be shown for the pyrolysis of a pure IL that very crystalline products are formed at relatively low temperatures around 600 °C. A similar behaviour was also reported in literature [254, 255] but could not yet be explained in detail.

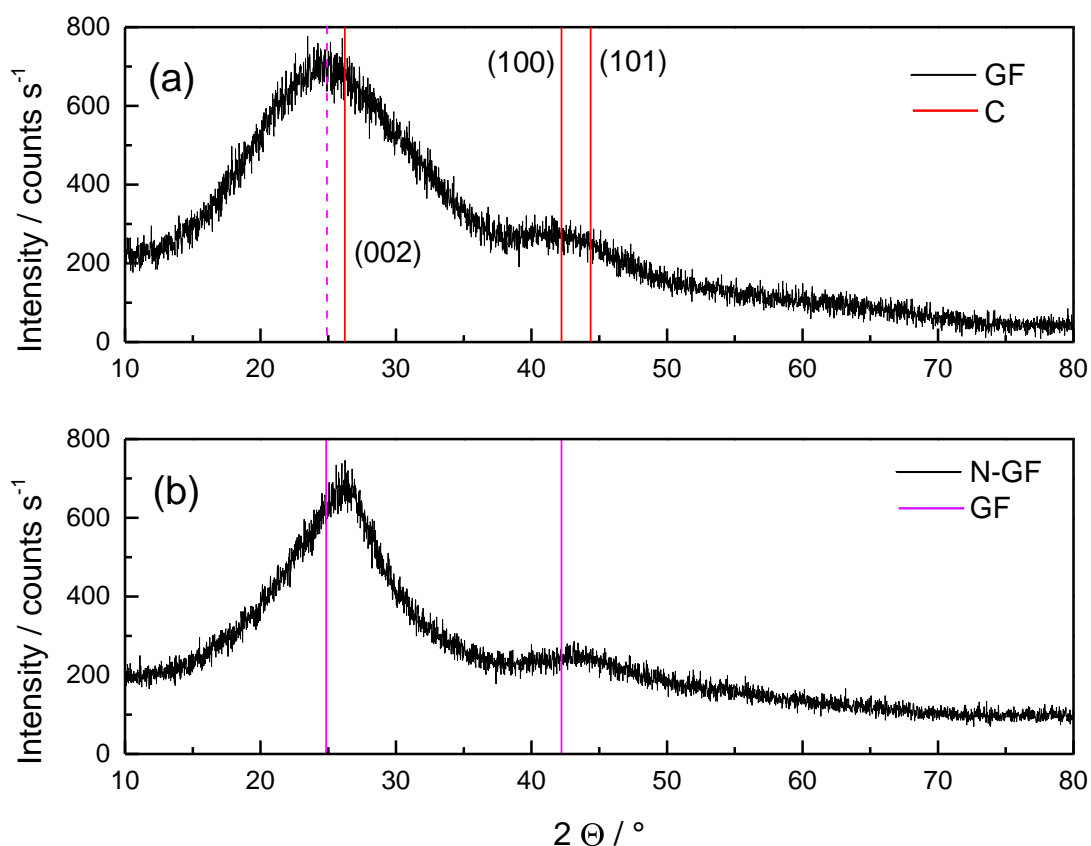


**Figure 5.7** XRD patterns of the (a) GF and (b) N-GF structures.

### 5.1.3.4 Raman Spectroscopy Characterization

Raman spectroscopy, a powerful tool for identifying electronic structure and degree of disorder, was applied to characterize the unmodified and the modified carbon structure [256]. The Raman measurements of the porous GF and N-GF are given in Figure 5.8 and Table 5.2. The spectrum shows three main features in the region between 1000 and 3000  $\text{cm}^{-1}$  as follows; (1) the D band is related to the breathing mode of the  $\text{sp}^2$  aromatic rings [257, 258] and is activated by structural defects and disordered structures; (2) the G band is associated with the  $E_{2g}$  vibration mode of  $\text{sp}^2$  carbon domains [259], which can be used to measure the degree of graphitization/order and (3) the 2D band is an overtone of the D peak. In Figure 5.8, the D band of GF was indicated at 1363  $\text{cm}^{-1}$ , whereas the D band of N-GF was observed at 1346  $\text{cm}^{-1}$  because of the disordered carbon structures caused by incorporated nitrogen atoms [260]. Compared to the G band of GF at 1586  $\text{cm}^{-1}$ , the G band of N-GF was slightly shifted to a lower wavenumber at 1575  $\text{cm}^{-1}$ . This result

corresponds to the model of incorporated atoms in a graphite lattice and was observed in the literature for many N-, and P-doped carbon systems [261, 262].

The appearance of a relatively weak 2D band at  $2743\text{ cm}^{-1}$  suggests that the N-GF contain mainly few-layered sheets due to  $sp^2$ -hybridised carbon atoms [263]. This result is in accordance with the electron microscopy data reported in Figure 5.4d. Tuinstra and König [264] noted that the intensity ratio of D to G peak ( $I_D/I_G$ ) gives information about the in-plane crystallite domain size, and therefore extent of order or disorder. The present  $I_D/I_G$  ratio for N-GF (Figure 5.8a) is 1.4 compared to 0.9 for GF, indicating a remarkably higher degree of disorder in the nitrogen containing N-GF sample, resulting from nitrogen species detected by XPS measurements and from lattice defects [256, 265]. Moreover, the full-width-at-half-maximum of the G peak ( $FWHM_G$ ) is a further indicator of lattice modification/disorder. Compared to the pure carbon sample (GF) the  $FWHM_G$  of N-GF is highly increased from  $92$  to  $145\text{ cm}^{-1}$ , confirming a higher degree of disorder.

In Figure 5.8b and Table 5.2, an increase of the synthesis temperature from  $600\text{ °C}$  to  $1000\text{ °C}$  leads to a remarkable decrease of the  $FWHM_G$ . As mentioned above, a very small  $I_D$  to  $I_G$  ratio indicates the existence of a highly ordered network of six-fold aromatic carbon rings. In the present measurements a decreasing  $I_D/I_G$  ratio of N-GF samples was observed with increasing synthesis temperature. From this behavior we assume a strong temperature dependence of incorporation of nitrogen atoms in the carbon lattice. At relatively low decomposition temperatures ( $600\text{ °C}$ ) the IL was fragmented in carbon and nitrogen species which built-up a nitrogen rich carbon lattice. By the fact that the nitrogen content of N-GF and the disorder in the lattice decreases at higher temperatures ( $700, 1000\text{ °C}$ ) we assume that a part of the formed nitrogen fragments reacts with oxygen and is not integrated in the carbon matrix. The results of the temperature dependence for the decomposition of nitrogen containing IL suggest that  $600\text{ °C}$  is an optimum temperature. From the XRD experiments we conclude the existence of very small crystalline areas in the range of some nanometres. According to Tuinstra and König [264] the crystalline domain size can be estimated from Raman measurements by

$$L_a = 4.4 / (I_D/I_G). \quad (1)$$

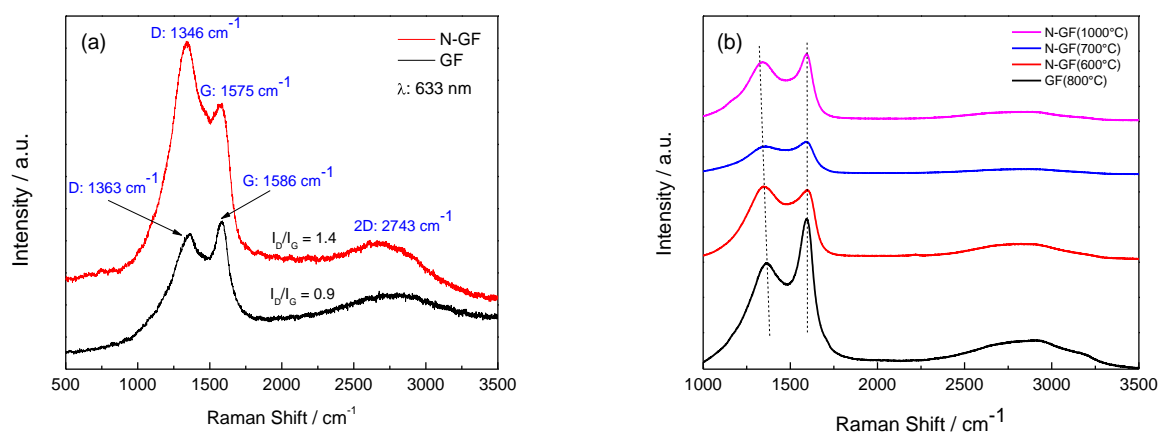


**Figure 5.8** Raman spectroscopy of the GF and N-GF measured with a wavelength of 633 nm (a) and temperature dependence of N-GF between 600 °C and 1000 °C (b).

**Table 5.2** Evaluation of Raman spectra measured on GF and N-GF samples prepared at different temperatures. P indicates the position, I the intensity,  $FWHM_G$  the peak breath of a Lorentzian fitting function, and  $L_a$  the size of undistorted carbon domains.

	$P_D$ ( $cm^{-1}$ )	$P_G$ ( $cm^{-1}$ )	$I_D$	$I_G$	$I_D/I_G$	$FMHW_G$ ( $cm^{-1}$ )	$L_a$ (nm)
<b>GF 800 °C</b>	1363	1593	79084	102911	0.76	92	5.8
<b>N-GF 600 °C</b>	1348	1597	167360	158427	1.05	145	4.2
<b>N-GF 700 °C</b>	1347	1596	18932	22324	0.84	115	5.2
<b>N-GF 1000 °C</b>	1348	1596	37109	41879	0.88	80	5.0

#### 5.1.4 Characterization of Supported Pt Catalysts

The XRD pattern of the Pt@N-GF is shown in Figure 5.9. Pt@N-GF has a broad (002) peak, reflecting the graphitic interlayer spacing, as well as the highly porous nature; very few layers are stacked together. The diffraction peak at  $2\theta = 39^\circ$  corresponds to Pt(111) planes of the face-centered cubic structure of crystalline platinum [PDF data base No. 98-002-199]. Pt@N-GF shows the typical Pt(111) peak, showing the smaller Pt nanoparticle size, which was derived using the Scherrer equation to be  $\sim 3.5$  nm. The resulting of Pt@N-GF shows much a better dispersion of Pt and an increased number of defects in the N-GF, due to the presence of nitrogen atom, or the higher binding energy between Pt and pyridinic N-doped carbon, compared with a pure graphene surface. Approximately 32 wt% platinum particles were decorated on the N-GF.

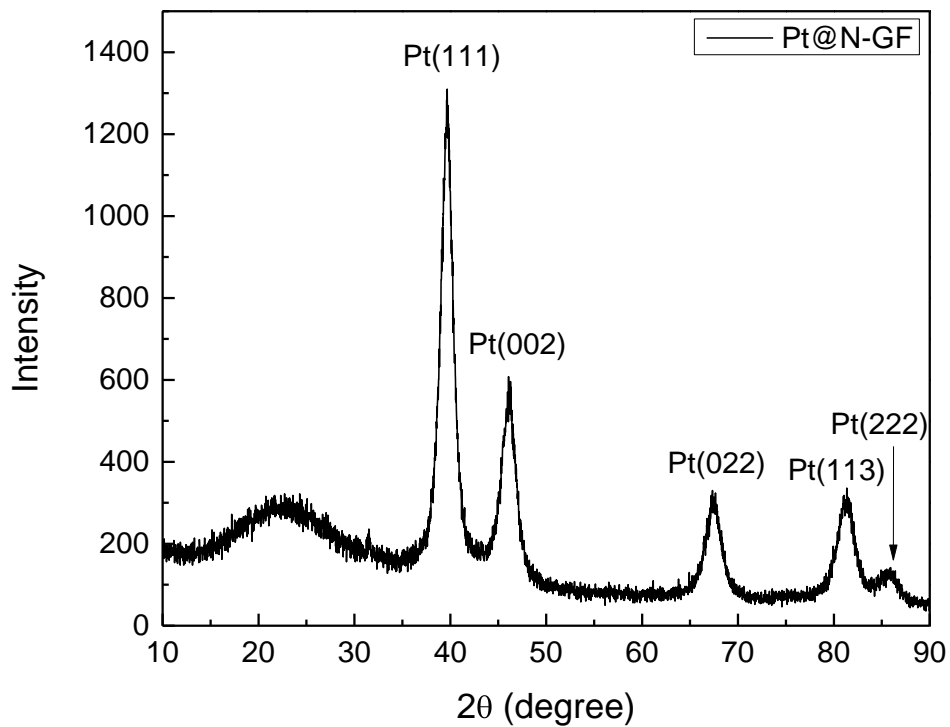


**Figure 5.9** Structure characterization of Pt@N-GF.

TEM images of the N-GF supported platinum (Figure 5.10) show that the catalyst particles are bonded onto the GF surface. The particles are homogeneously distributed between the foams, and the particle size is in the range of 2–5 nm.

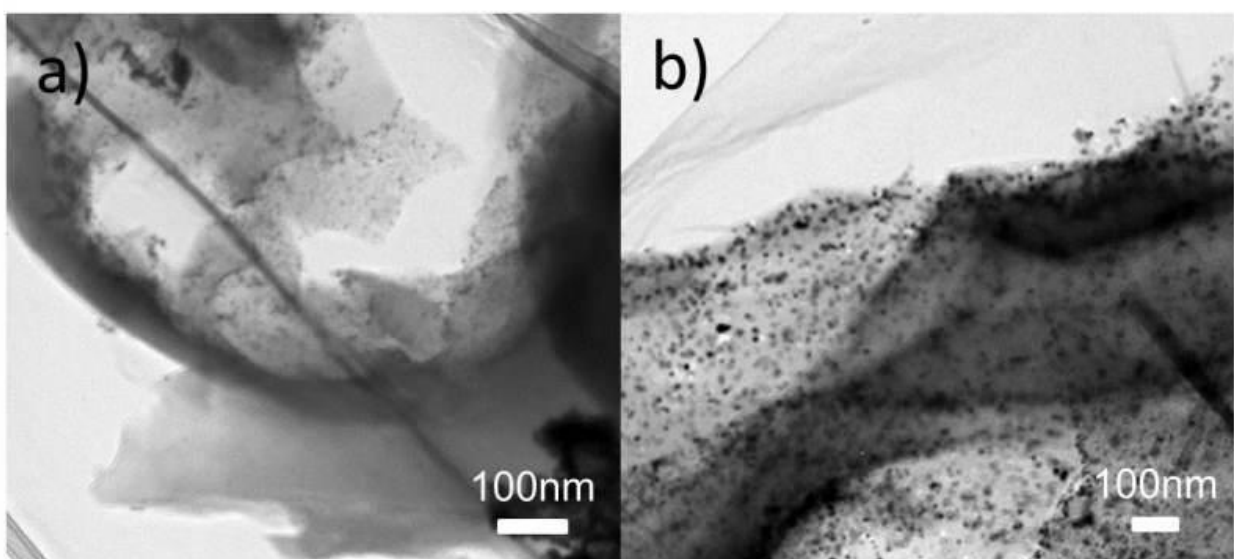


**Figure 5.10** TEM images of Pt catalysts deposited on the inner side of the N-GF mesopores.

To determine the ratio of Pt@N-GF, the EDX measurement was analyzed (Figure 5.11). The value of the used samples was: C: 77.45 at%, N: 13.18 at%, O: 4.57%, Cu: 3.57 at% and Pt: 1.24 at%. Copper element was detected by using a Cu grid substrate.

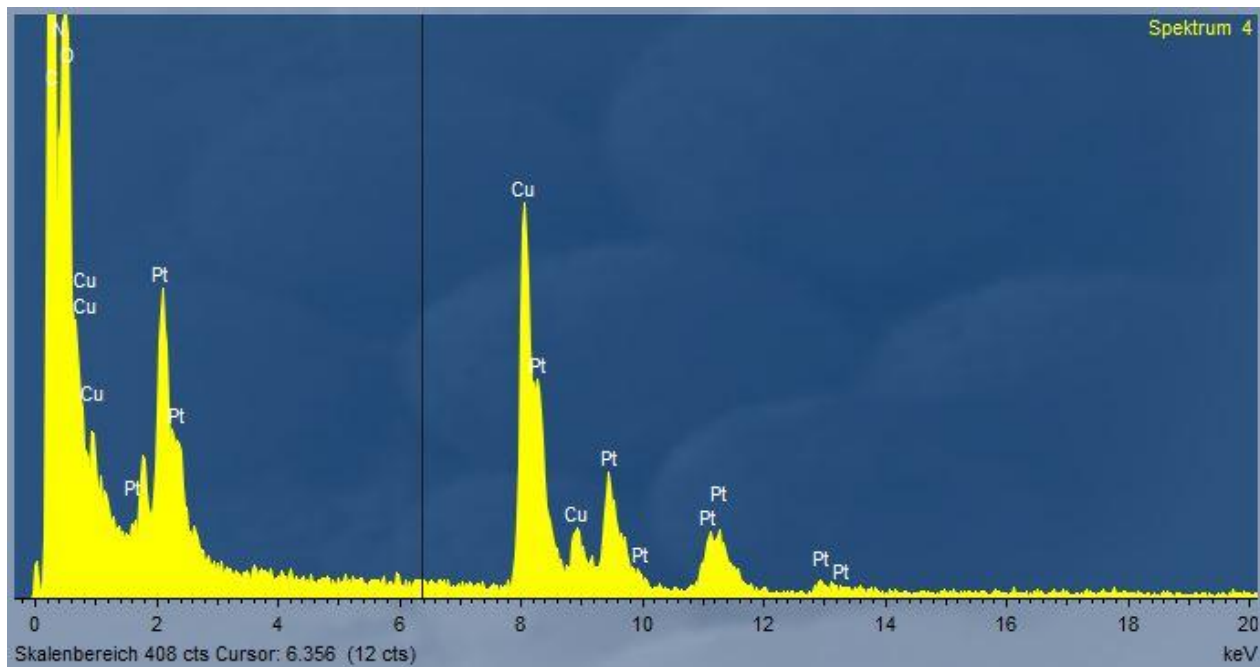


**Figure 5.11** EDX measurement of Pt@N-GF.

## 5.1.5 Electrochemical Characterization of the Foam Structures

### 5.1.5.1 Electronic Conductivity of the GF and N-GF

On applying a new material as catalyst support electrochemical characterization should confirm an improvement of the PEMFC performance. We analyzed the electronic conductivity of the new supports and interfacial processes, and the electrode kinetics of carbon supported platinum catalysts. Ex-situ EIS measurements were performed to characterize the electronic conductivity of the prepared samples. The series of resistors of overall electronic resistance are located along the electron conduction path (Figure 3.3). In the present EIS measurement, the observed difference in resistance could be related to the ohmic resistance of the catalyst support ( $R_{CS}$ ) by keeping the other factors ( $R_{CA}$ ,  $R_{CE}$ ,  $R_{EL}$ ,  $R_{NL}$  and  $R_{WE}$ ) constant.

Figure 5.12 shows the Nyquist plot of two identically prepared samples (GF, N-GF) measured by RDE experiments. Compared to the black glassy carbon electrode the measured ohmic resistance of the N-GF sample is three times lower than the resistance of the unmodified GF system. This

relative comparison indicates a decreased ohmic resistance, caused by a decreased interparticular (among the catalyst support particles and from the catalyst supports to the GDL) contact resistance and by a reduced intraparticular resistance of the NCL.

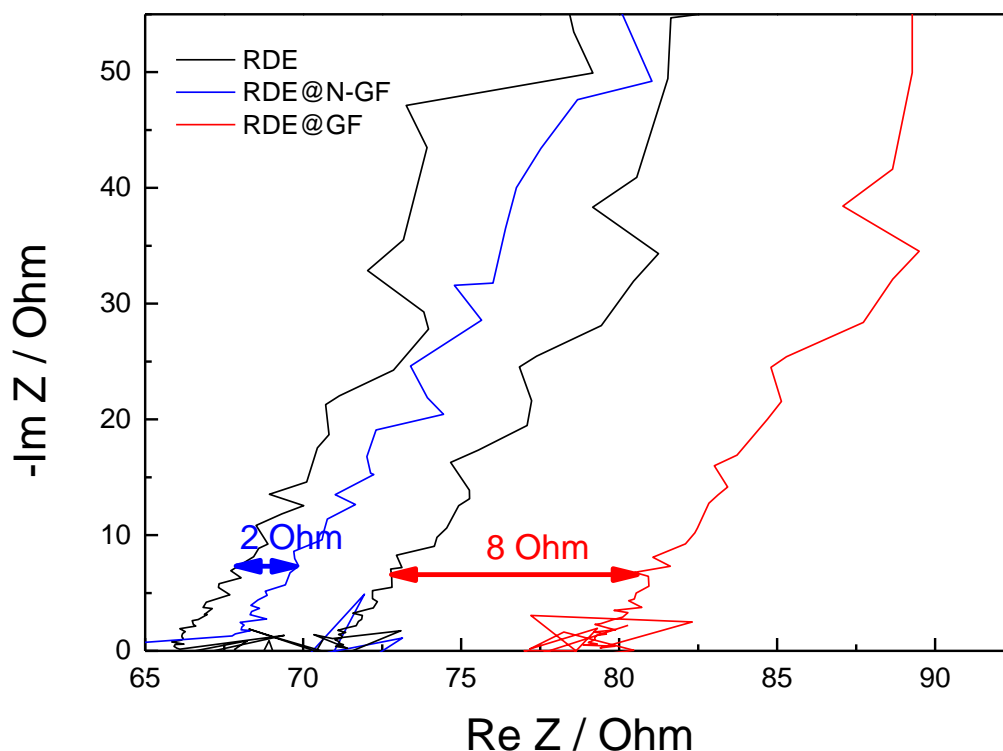


**Figure 5.12** Electrochemical impedance spectroscopy of GF and N-GF.

### 5.1.5.2 Electrochemical Activity towards the ORR

The as-synthesized Pt@GF and Pt@N-GF catalysts were examined comparing its activity with a commercial Pt@C. Figure 5.13 shows the polarization curves for Pt@GF and Pt@N-GF at rotation speeds of 200 – 2000 rpm in  $\text{O}_2$ -saturated 0.1 M  $\text{HClO}_4$  using RDE measurement. All polarization curves were recorded between 0.1 – 1.08 V vs.RHE, comprising the mass transport diffusion region. The current density increases with increasing rotation speed. Thereby, the oxygen diffusion to the catalytic reaction center is the rate limiting process and in consequence dependent on the rotation rate. The mass transport diffusion region turns into a mixed diffusion – kinetic region at higher voltages. Finally from about 0.76 V vs. RHE, the reaction rate is only kinetically controlled, as judged by the independence of the rotation rate.

ORR curves of the Pt@GF and Pt@N-GF have relatively high current densities in RDE measurement at the very low Pt loading.

In the ORR potential window the limiting current density at 1600 rpm of Pt@GF and of Pt@N-GF is ca.  $4.02 \text{ A cm}^{-2}$  and ca.  $1.66 \text{ A cm}^{-2}$ , respectively, and the theoretical value should be ca.  $6 \text{ A cm}^{-2}$ . In the mixed kinetic-diffusion potential window (0.8 - 0.6 V vs. RHE) the current densities of both Pt@GF and Pt@N-GF should not rise with the rotation because of a very small Pt surface/loading.

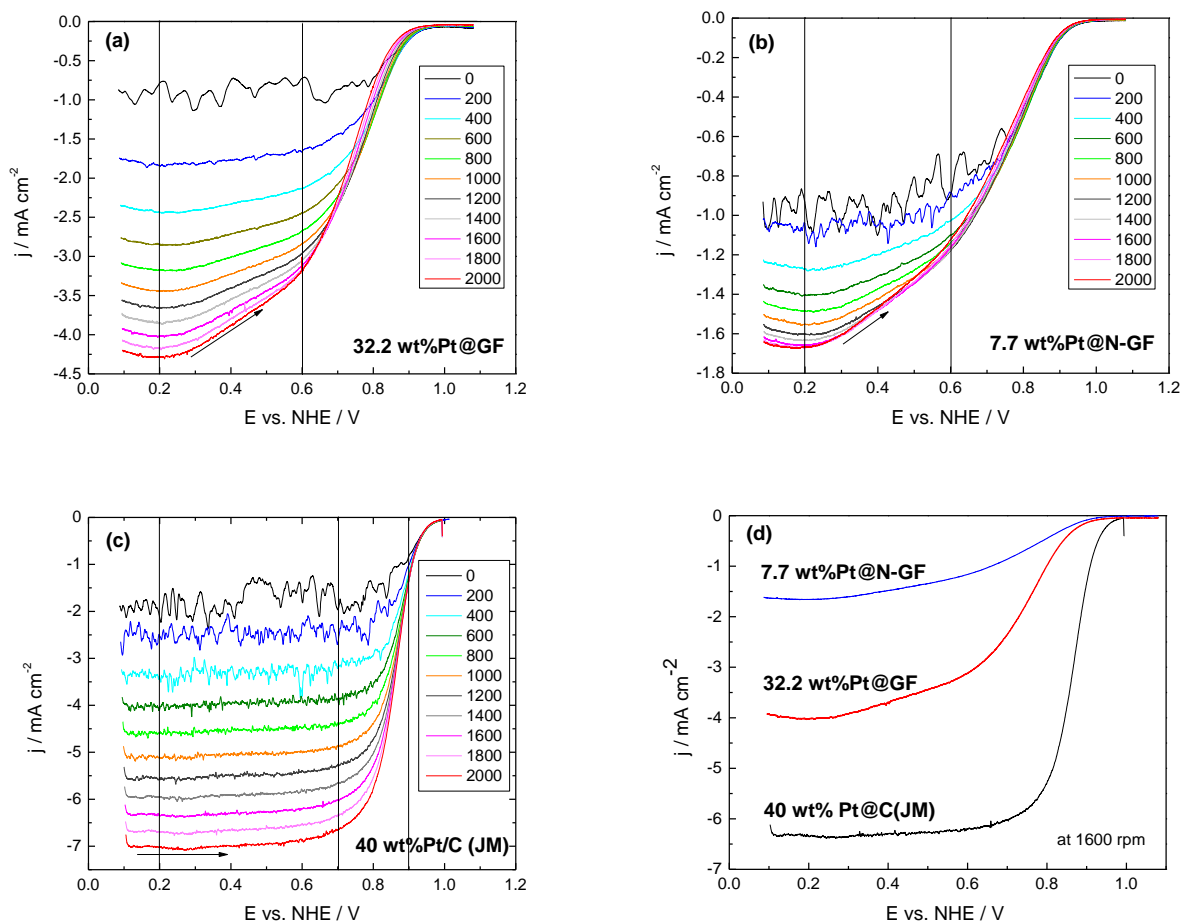


**Figure 5.13** Oxygen reduction reaction of the (a) Pt@GF, (b) Pt@N-GF and (c) Pt@C at rotation speeds of 200 – 2000 rpm in  $\text{O}_2$ -saturated 0.1 M  $\text{HClO}_4$ . (d) Compared ORR polarization curves of 32.2 wt%Pt@GF, 7.7 wt%Pt@N-GF and 40 wt%Pt@C measured by RDE experiments at 1600 rpm.

The kinetic current density can be derived from the Koutecky-Levich (K-L) equation [266]. The slopes of K-L plots of 40 wt% Pt@C (ca.  $6670 \text{ cm}^2 \text{ A}^{-1} \text{ min}^{-0.5}$ ) reveals that the ORR proceed via 4e- mechanism; the calculated K-L value is  $6622 \text{ cm}^2 \text{ A}^{-1} \text{ min}^{-0.5}$  [267]. The K-L slopes at 0.6 V vs. NHE (Figure 5.14) are  $5826 \text{ cm}^2 \text{ A}^{-1} \text{ min}^{-0.5}$  for 32.2 wt% Pt@GF and  $6365 \text{ cm}^2 \text{ A}^{-1} \text{ min}^{-0.5}$  for 7.7 wt% Pt@N-GF. It indicates a direct ORR mechanism, confirming the electron transfer number near

4e-. All results obtained from electrochemical half-cell measurements are summarized in Table 5.3.

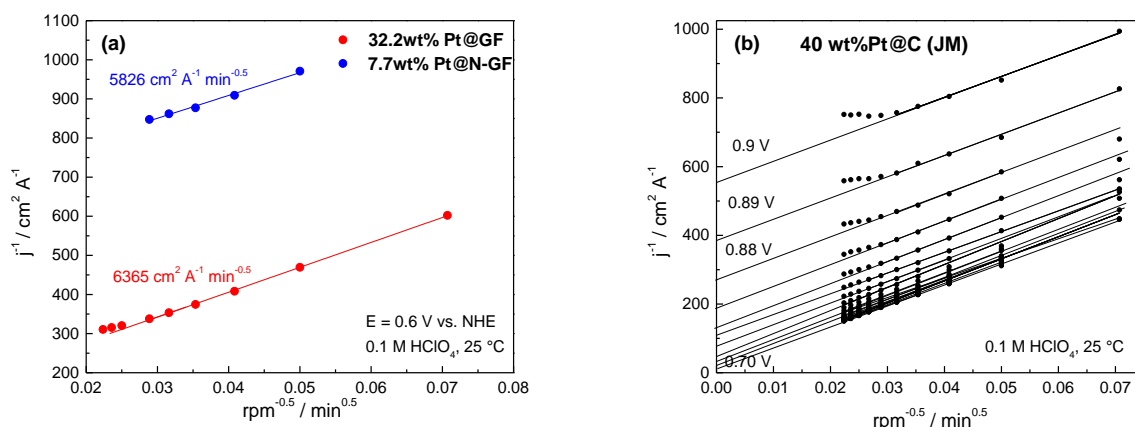


**Figure 5.14** (a) Koutecky – Levich plots of 32.2 wt%Pt@GF and 7.7 wt%Pt@N-GF measured by RDE experiments at 0.6 V vs NHE in 0.1M HClO<sub>4</sub> at 25 °C. (b) The K-L plots of 40 wt%Pt@C (JM) was recorded between 0.9 V and 0.7 V.

**Table 5.3** Summary of the results obtained by RDE experiments in 0.1M HClO<sub>4</sub>.

	Pt (mg cm <sup>-2</sup> )	<sup>a</sup> $j \cdot 10^{-3}$ (A cm <sup>-2</sup> )	<sup>b</sup> $j_k \cdot 10^{-3}$ (A cm <sup>-2</sup> )	K-L (cm <sup>2</sup> A <sup>-1</sup> min <sup>-0.5</sup> )
<b>Pt@C(JM)</b>	0.031	-1.33	-1.68	6622
<b>Pt@GF</b>	0.030	-0.140	-0.145	5826
<b>Pt@N-GF</b>	0.021	-0.0876	-0.0925	6365

<sup>a</sup> corrected current measured at 0.9 V at 1600 rpm

<sup>b</sup> kinetic current density at 0.9 V,  $j_k = (j_d \cdot j) / (j_d - j)$

### 5.1.5.3 Stability of the Catalysts

For electrochemical stability testing, the long-term behaviour of supported platinum catalysts was measured by an electrochemically accelerated degradation method according to Meier et al. [239]. The platinum loading of the samples prepared by electrochemical reduction is 0.077 mg Pt/cm<sup>2</sup> for Pt@N-GF and 0.322 mg Pt/cm<sup>2</sup> for Pt@GF, respectively. The ECSA results are given in Figure 5.15c. The progression of two measurement series is quite different. GF shows relatively high initial ECSA which decreases with increasing cycling number whereas N-GF reveals a kind of activation process followed by the degradation. The differences of degradation are remarkable:

within 1500 cycles the ECSA decreases by 96.3 % for GF and by 41.8 % for N-GF, respectively. The initial activation process of N-GF sample could be attributed to the smaller pore size and hierarchical structure which influence diffusion and wetting processes. After 500 cycles the ECSA of N-GF increases because of good catalytic activation in N-containing catalyst supports. It shows two times better stability compared to the GF after 1500 cycles. This measurement demonstrates the increased stability of N-containing catalyst supports.

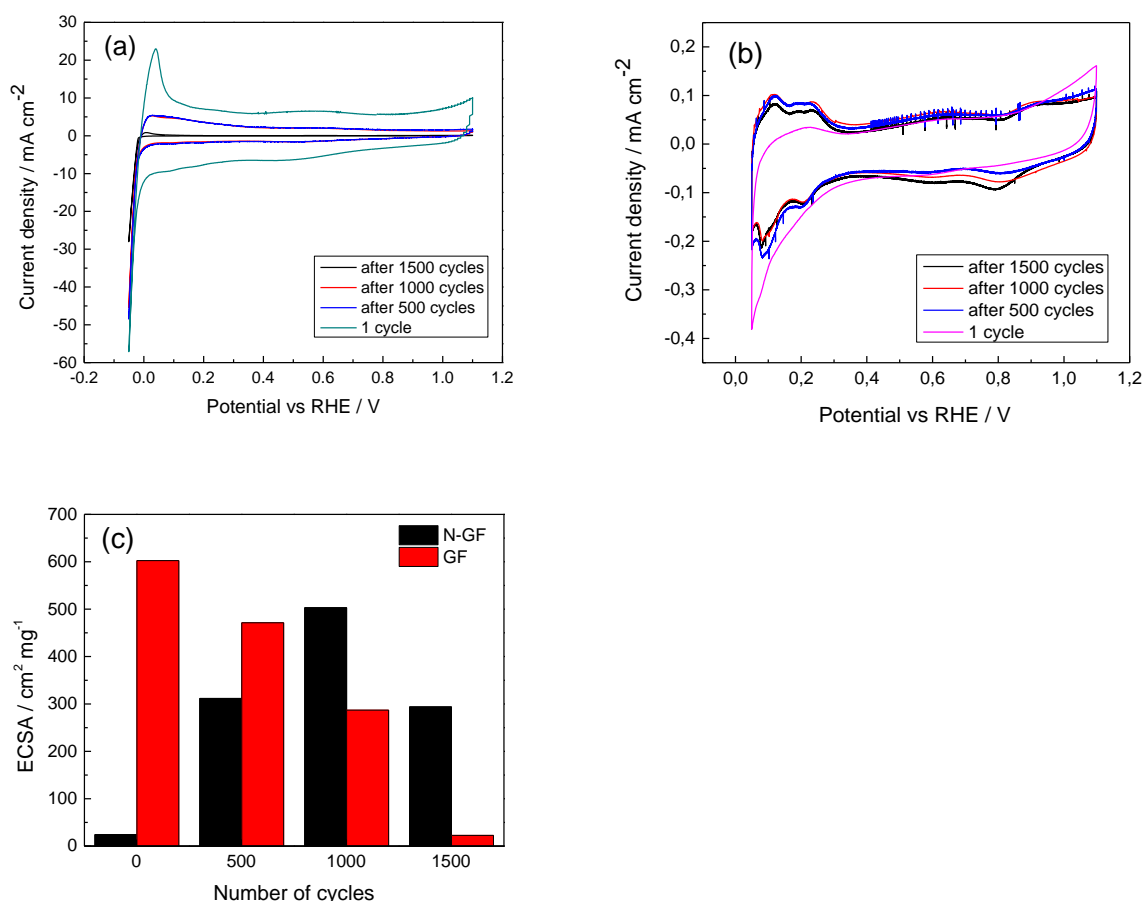


**Figure 5.15** CVs of (a) Pt@GF and (b) Pt@N-GF were taken at a scan rate of 20 mV s<sup>-1</sup> in N<sub>2</sub>-saturated HClO<sub>4</sub>. (c) ECSA of Pt@GF (red column) and Pt@N-GF (black column) calculated from H<sub>2</sub>-desorption regions of CV measurements.

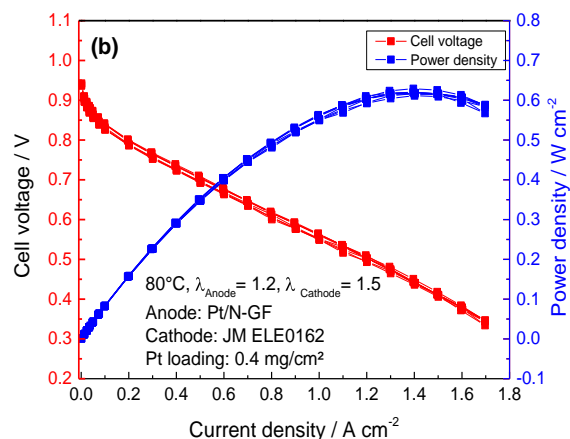
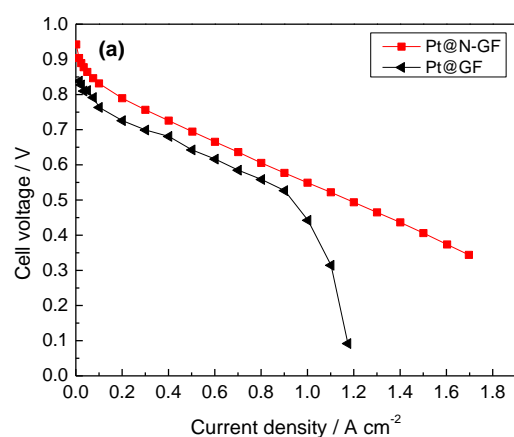
#### 5.1.5.4 Polarization Curves on MEA

The performance of MEAs consisting of an anode coated with self-made platinum catalysts supported on different carbon supports (N-GF, GF, G, CNT and carbon black (C)) were measured in a fuel cell test station. A catalyst loading of 0.077 mg cm<sup>-2</sup> was used for Pt@N-GF, whereas

loadings of 0.322 and 0.350 mg cm<sup>-2</sup> were used for Pt@GF and Pt@commercial supports, respectively. The polarization curves and power density measurements of the MEAs are presented in Figure 5.16.

The polarization curves of Pt@N-GF (Figure 5.16a) show a current density of 0.85 A cm<sup>-2</sup> at 0.6 V whereas the unmodified GF sample has a current density of 0.66 A cm<sup>-2</sup>. In addition, the N-GF sample was compared to platinum catalysts supported on commercial carbons. A comparison of Pt mass activity measured at 0.85 V (Figure 5.16d) shows a decrease in the following sequence: N-GF (0.910 A mg<sup>-1</sup>) > CNT (0.091 A mg<sup>-1</sup>) > GF (0.057 A mg<sup>-1</sup>) > C (0.036 A mg<sup>-1</sup>) > G (0.01 A mg<sup>-1</sup>), that means the mass normalized performance of N-GF is about ten-times higher than the sample prepared with carbon nanotubes. Furthermore, the shape of the N-GF polarization curve differs from the other ones. It has an extended ohmic region without a sharp bend, indicating very good mass transport behavior of products and educts. The results confirm that the new catalytic system influences the electronic conductivity, the catalytic activity and therefore the performance of the electrocatalytic process. These results demonstrate that the optimized catalyst support leads to a reduction of the noble metal amount which could enable the production of cheaper fuel cell membrane electrode assemblies.

The very good performance of the new nitrogen doped catalyst support originates from an improved mass transport of products and educts caused by the hierarchical structure, and by an improved conductivity of the support material as demonstrated in the electrochemical characterization section. For this reason the presented hierarchical carbon support is a promising material for electrocatalytical applications.



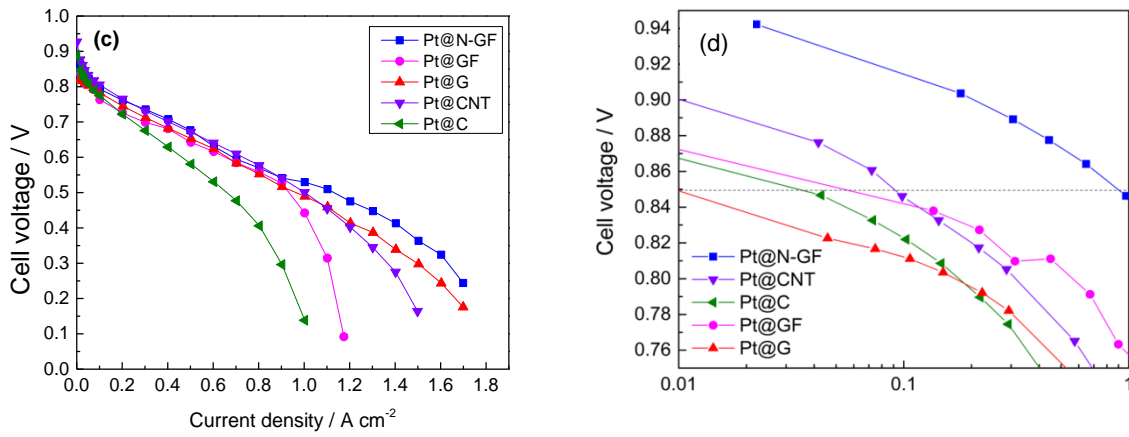


**Figure 5.16** Fuel cell test station measurement for self-prepared anodes. (a) current density of an anode coated with GF (Pt loading: 0.322 mg cm<sup>-2</sup>) or N-GF (Pt loading: 0.077 mg cm<sup>-2</sup>) at 80 °C; (b) current density and power density of Pt@N-GF; (c) polarization curves of MEAs prepared with different catalyst supports; and (d) Tafel representation of cell voltage (V) vs Pt mass activity (A/mg<sub>Pt</sub>).

## 5.2 Discussion

Hierarchical structured multilayer graphene foams coated with a N-containing carbon layer have been successfully fabricated by decomposition of EMIM-dca. It could be seen that the 3D hierarchical carbon system consists of an undoped macro-/microporous GF with a nitrogen rich meso-/micro- porous carbon coating.

Coatings with a very high nitrogen coating level up to 35.3 wt% were achieved. Compared to uncoated GF it shows that the N-GF has an increased electronic conductivity caused by a high nitrogen coating. The prepared coating has to be consisting of a nitrogen compound or a mixture of different nitrogen containing compounds. It could be demonstrated that the  $C_5N$  and  $C_3N_4$  compounds of N-GF occur in the product with a ratio of about 50:50, corresponding a nitrogen content of 41.40 wt% and a carbon content of 57.14 wt%. This result is similar to the present CHN analysis (N: 35.31 wt%, C: 58.64 wt%).

Structural characterization by XRD analysis reveals that the two different nitrogen containing species,  $C_3N_4$  and  $C_5N$ , were formed after the coating process. This coating process not only can be used for any carbon material, but it also represents a suitable approach for sustainable and clean energy sources.

Electrochemical characterization of PEMFC prepared with the new material shows that the N-GF supported Pt catalysts lead to an increased performance combined with a low polarization loss. It could be demonstrated that the hierarchical design improves the mass transport in PEMFC MEAs by the formation of a very porous gas diffusion network. In comparison to a commercial MEA it shows that the Pt@N-GF MEA has a ten times better mass activity that means comparable power densities can be generated with 90% lower platinum loading. Furthermore, EIS experiments also reveal that the NCL system has an increased electronic conductivity, which indicates a relatively 4-times decrease of electronic resistance than uncoated GF catalyst support systems. These results demonstrate that the optimized catalyst support leads to a reduction of the noble metal amount which could enable the production of cheaper fuel cell membrane electrode assemblies.

## 6. Different Carbon Morphologies Coated with Nitrogen-Containing Carbon Layers

A new, facile and green method was developed to prepare nitrogen-coated graphene- and CNT-based materials with a mesoporous surface structure. Highly conductive catalyst supports with different morphologies were synthesized by surface modification using a nitrogen containing IL. The surface modification was done by impregnating the carbon materials in nitrogen containing ILs followed by a thermal treatment under air. The nitrogen-containing graphene- and CNT- structures as new carbon supports promise three advantages:

1. The homogeneous modified surface enables a highly dispersed deposition of catalyst particles with a strong adhesion between the platinum catalyst and the carbon surface.
2. The electronic conductivity of the carbon support was increased by nitrogen coating.
3. A mixture of graphene/CNT reduces the mass transport limitations of educt/products from and to the catalyst sites by formation of a very porous carbon network.

For electrocatalytic applications, a scheme of the different sample structures is shown in Figure 6.1. The graphene flakes (Figure 6.1a) form a dense roof tile structure. The CNT sample (Figure 6.1b) forms an interconnected CNT network. A mixture of graphene and CNT (Figure 6.1c) can create new functions and complementary properties as retaining the advantages of each material. In addition, these materials are useful in optimizing the porous structure, since the incorporation of graphene flakes and CNT frustrates the strong  $\pi$ - $\pi$  interactions. Therefore, the formation of aggregation or tightly stacked structure is prevented and this structure can lead to the improvement of mass transport.

The mixture of N-coated graphene with uncoated CNT (Figure 6.1d) causes a further reduction of resistance. This improvement is due to the N-coating with its higher conductivity than the cross-plane conductivity of graphene. The mixture of uncoated graphene and N-coated CNT (Figure 6.1e) has a stronger influence on the conductivity than coated graphene. Due to the different interconnecting areas of the two carbon morphologies, the electrons move very fast in the in-plane direction of the graphene flakes which are interconnected with very well conducting spacer. It demonstrates that the surface modification is responsible for a significantly enhanced catalytic efficiency and therefore improved electrochemical performance in the previous work. For this reason we propose the application of these materials as a catalyst support for PEMFC applications.

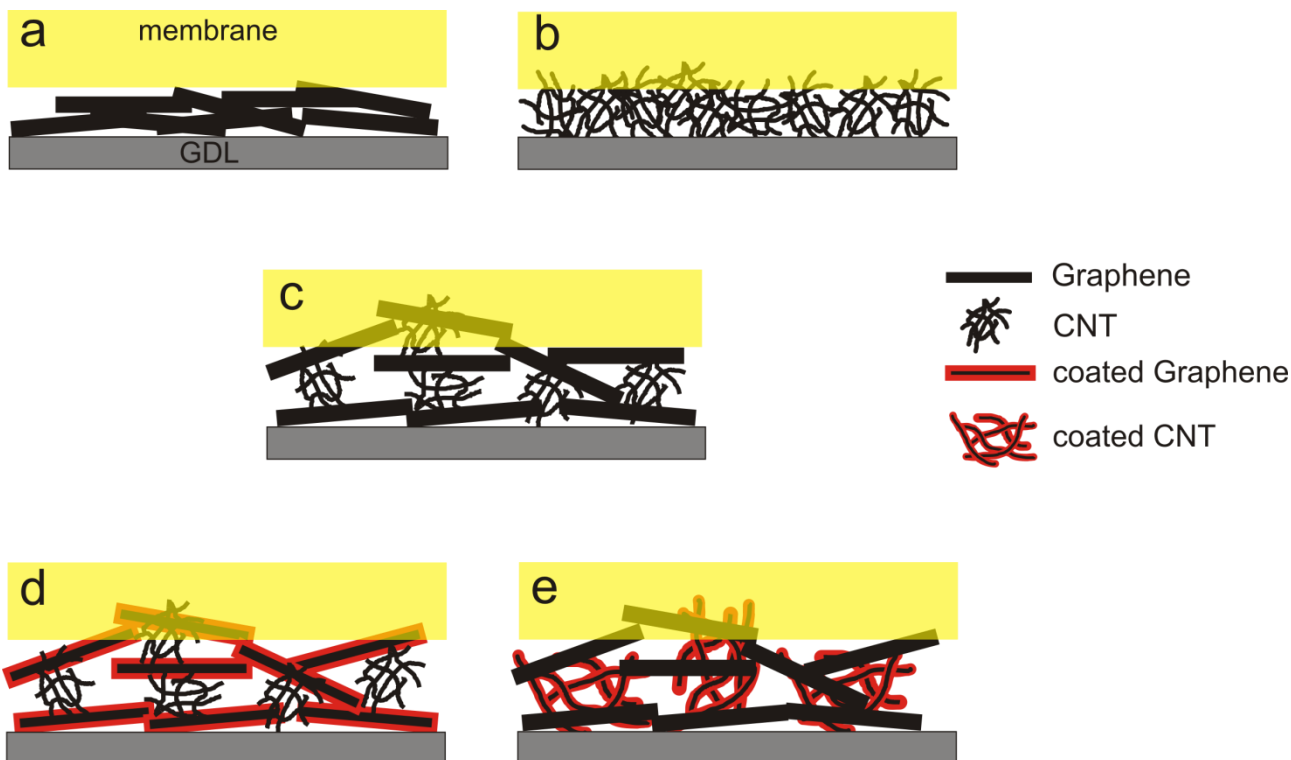


**Figure 6.1** Scheme of different carbon morphologies: (a) graphene, (b) CNT, (c) G/CNT, (d) N-G/CNT and (e) G/N-CNT.

## 6.1 Results

### 6.1.1 Elemental Analysis

The resulting product was characterized by CHN analysis to determine its exact element contents. It is known from literature that the nitrogen content and the surface area of thermally decomposed ILs depend strongly on the used IL-precursor and on the carbonization temperature [268-270]. For this reason the carbonization temperature of EMIM-dca-graphene and EMIM-dca-CNT was measured in a temperature range between 600 and 800 °C. It was found that 600 °C is the optimal temperature for the thermal decomposition: below this temperature yellow reaction products are observed and above the IL decomposes completely to gaseous products.

Table 6.1 shows the element compositions of N-G and N-CNT after impregnating with EMIM-dca and thermal decomposition. It could be confirmed that the nitrogen doping level can be varied by the amount of added IL and by the decomposition temperature. The nitrogen content was derived from the atom ratio of carbon to nitrogen ( $IL_R$ ).

**Table 6.1** Element compositions of the N-G and N-CNT prepared with different EMIM-dca contents and temperatures.

<b>Carbon substrate / IL amount / Temperature</b>	<b>C content [wt%]</b>	<b>H content [wt%]</b>	<b>N content [wt%]</b>
IL <sub>R</sub> = 5 (N-G, 600 °C)	72.497	0.0169	21.931
IL <sub>R</sub> = 10 (N-G, 600 °C)	65.920	0.0172	24.040
IL <sub>R</sub> = 15 (N-G, 600 °C)	64.123	0.0143	27.469
IL <sub>R</sub> = 5 (N-CNT, 600 °C)	72.512	2.0448	21.036
IL <sub>R</sub> = 10 (N-CNT, 600 °C)	64.464	2.4356	23.124
IL <sub>R</sub> = 15 (N-CNT, 600 °C)	62.937	2.3927	29.761
IL <sub>R</sub> = 15 (N-G, 800 °C)	79.938	0.0084	6.0259
IL <sub>R</sub> = 15 (N-CNT, 800 °C)	89.471	0.5191	6.2124

### 6.1.2 Morphology Characterization

The morphology of carbon samples was measured by SEM analysis. Commercial graphene (AO-2) samples show an average flake diameter of 5.3–8.0 μm (Figure 6.2a). The flakes consist of 44–52 monolayers. CNT (Baytubes C150P<sup>®</sup>) have a typical length distribution between 1 and 4 μm (Figure 6.2b). Figure 6.2c and Figure 6.2d show that the coating process does not change the structure and morphology of the initial products.

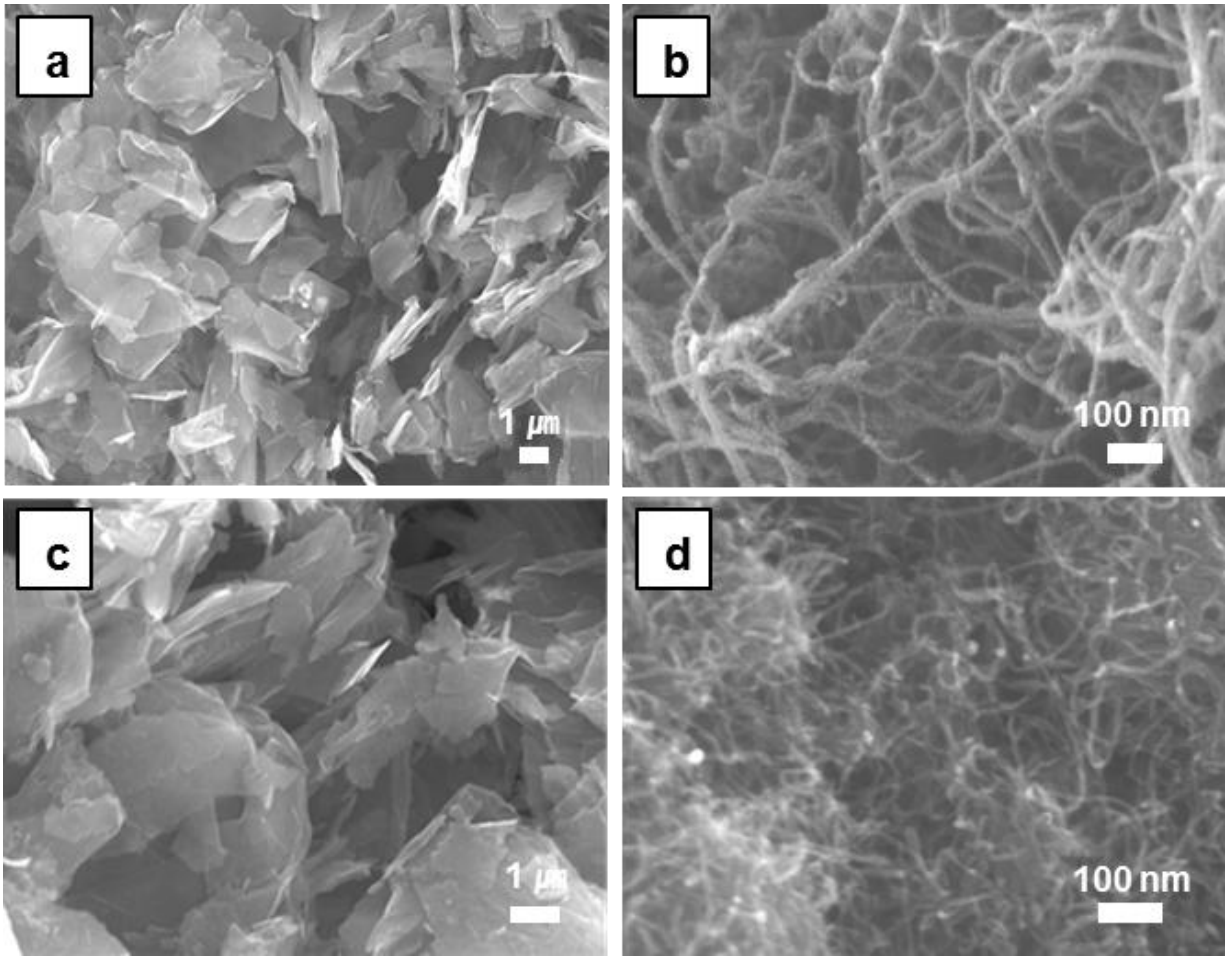


**Figure 6.2** SEM images of commercial (a) AO-2 graphene, (b) C150P nanotubes and nitrogen-coated (c) N-G, (d) N-CNT.

An examination of the coated samples was done by TEM and EDX analysis. The coating onto the graphene structure shows a thickness between 11 and 13 nm (Figure 6.3a). The CNT (Figure 6.3b) has an inner diameter of about 4 nm, outer mean diameter of 13–16 nm, and a typical length distribution between 1 and 4 μm. TEM images of the N-G and N-CNT (Figure 6.3c,d) show the thickness of each layer wall, approximately 13 nm. EDX analysis was performed for the determination of the sample composition. The results are given in Table 6.2.

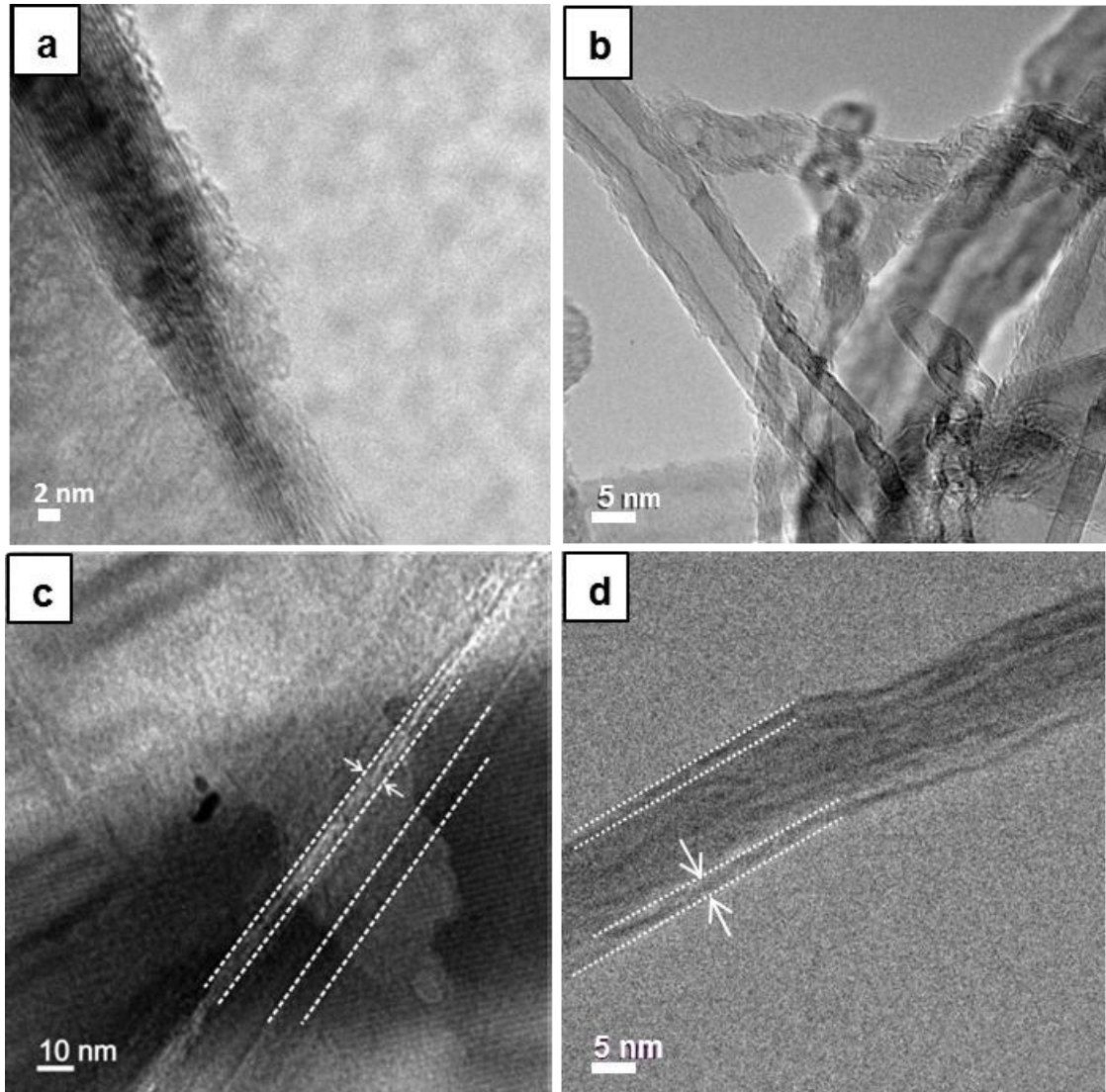


**Figure 6.3** TEM images of (a) AO-2 graphene, (b) CNT, (c) N-G and (d) N-CNT.

**Table 6.2** Element composition of N-G and N-CNT measured by EDX.

Samples	C K [at%]	O K [at%]	O K [at%]
N-G	70.21	23.31	3.2
N-CNT	79.44	15.08	1.6

### 6.1.3 Structure Characterization

To examine the graphitic character, the pure AO-2, N-G, pure CNT and N-CNT were measured by XRD analysis. As illustrated in Figure 6.4, the measured XRD patterns correspond to the hexagonal graphitic structure according to the PDF standard [75-2078]. Because of the very good layer orientation of the pure AO-2, the Bragg reflection of the (111) plane dominates and the others are suppressed or not visible. Compared to uncoated species the N-coated samples show a peak broadening and an increase of the background. The peaks of AO-2 are much narrower and more intensive than the peaks of CNT, which reveals a higher degree of graphitization. As shown in Figure 6.3c, d, the coating of carbon structures has a thickness below 10 nm and for this reason additional peaks resulting from the  $C_3N_4$ ,  $C_5N$  structures could not be observed. We connect peak broadening of the coating structure with existence of N-containing carbon coatings.

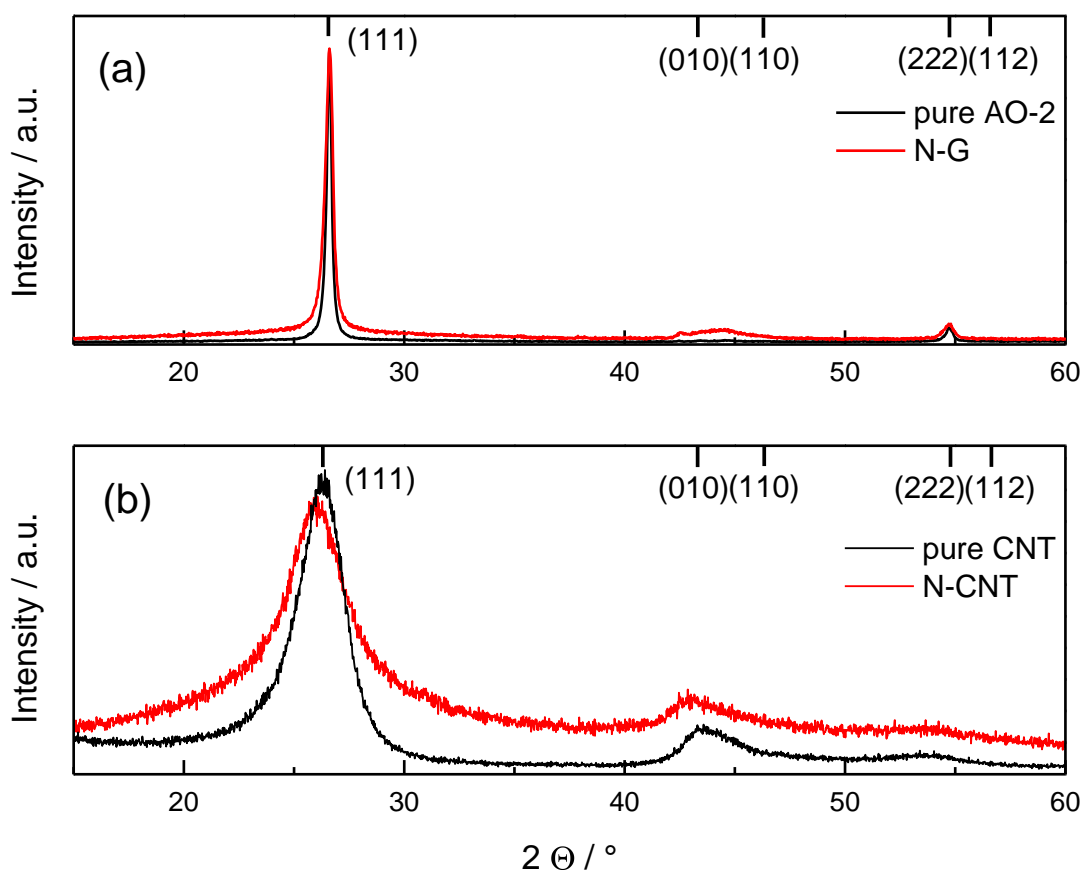


**Figure 6.4** XRD patterns of (a) pure AO-2, N-G and (b) pure CNT, N-CNT.

## 6.1.4 Physical Characterization

### 6.1.4.1 BET Characterization

The specific surface areas ( $S_{\text{BET}}$ ) and pore diameters were calculated by BET nitrogen gas adsorption. The results are given in Table 6.3. We confirm that the specific surface area of N-G and N-CNT is significantly higher than that of uncoated carbon substrates. The results reveal that the coating process increases the specific surface area and reduces the micro-pore diameter.

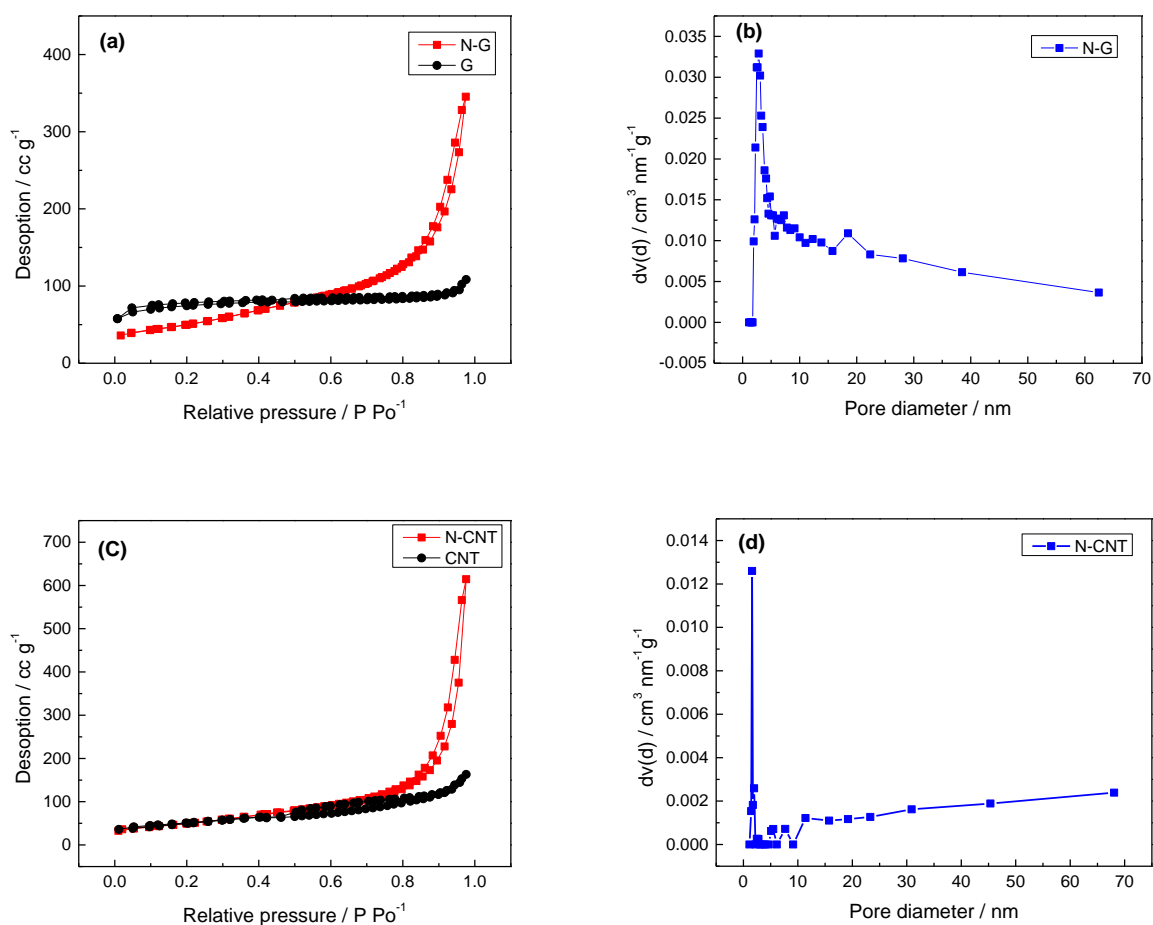


**Figure 6.5** N<sub>2</sub> adsorption-desorption isotherms for (a) the graphene and N-G, (c) CNT and N-CNT; pore diameter for (b) the N-G and (d) N-CNT.

**Table 6.3** Porous properties of graphene, CNT, N-G and N-CNT.

<b>Samples</b>	<b>S<sub>BET</sub> (m<sup>2</sup>g<sup>-1</sup>)</b>	<b>Pore diameter (nm)</b>
<b>Graphene</b> [241]	77.1	3.2
<b>N-G</b>	182.9	1.6
<b>CNT</b> [271]	172.3	4.1
<b>N-CNT</b>	392	1.4

#### 6.1.4.2 Raman Spectroscopy Characterization

Raman spectra, a powerful tool for identifying structure, disorder, doping and the number of graphene layers, were applied to characterize the carbon structure. To prove effects of the nitrogen coating, the as-prepared porous materials were measured by Raman spectroscopy measurement (Figure 6.6). As the  $I_D/I_G$  ratio increases, the defect structure increases and the degree of graphitization becomes less. It can be seen (Figure 6.6a, b) that the  $I_D/I_G$  ratio of graphene is low and N-coated graphene has a slightly higher degree of graphitization. The  $I_D/I_G$  ratio of N-CNT indicates a higher degree compared with CNT, which has the G-band of graphitic carbon downshifted by  $8\text{ cm}^{-1}$ , caused by the N coating [260]. Also, the shape of the 2D band, in combination with its down shifted peak position, is indicative of a few graphitic layers.

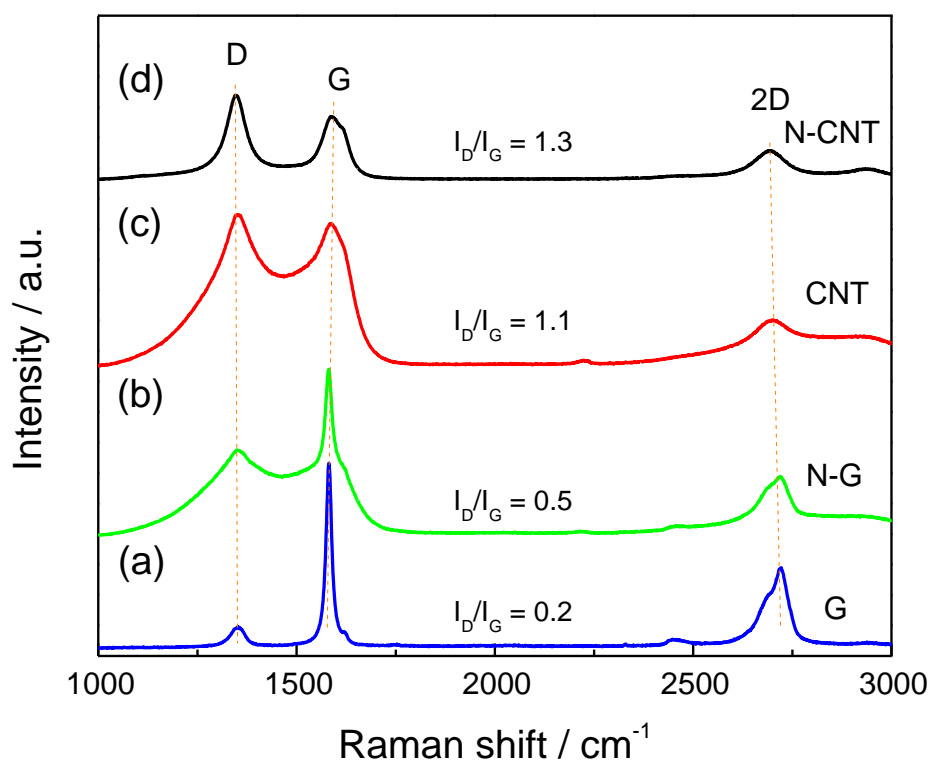


**Figure 6.6** Raman spectra of (a) graphene, (b) N-G, (c) CNT and (d) N-CNT.

**Table 6.4** Evaluation of Raman spectra prepared at different temperatures. P indicates the position, I the intensity,  $FWHM_G$  the peak breath of a Lorentzian fitting function, and  $L_a$  the size of undistorted carbon domains.

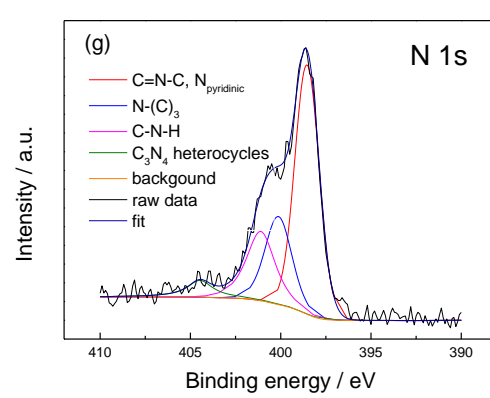
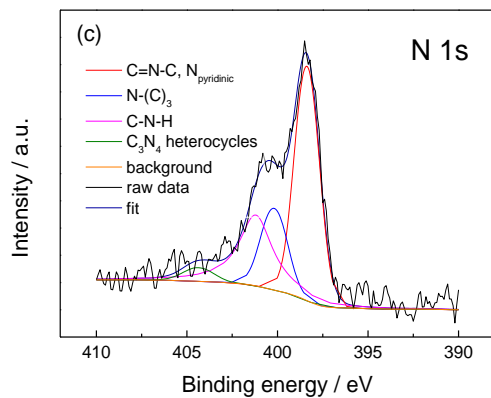
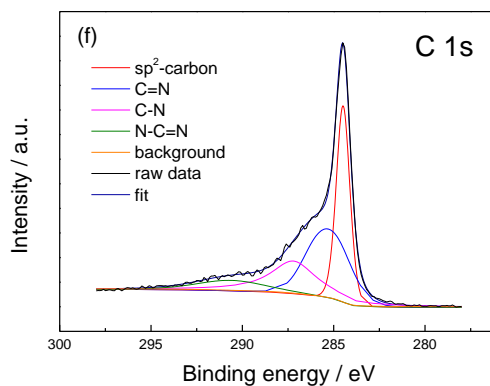
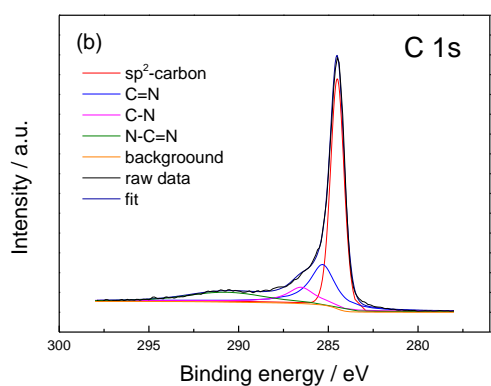
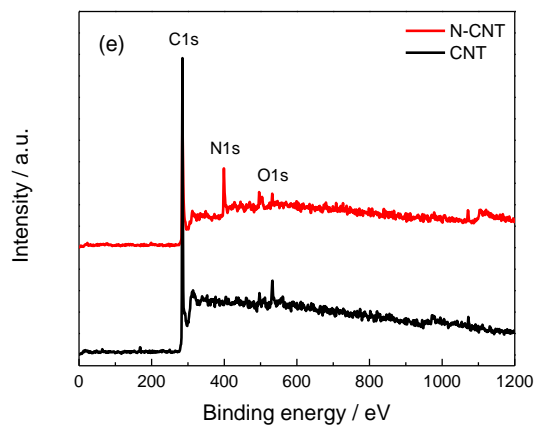
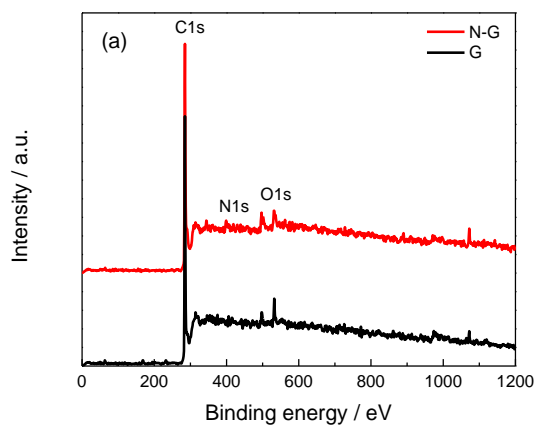
	$P_D$ ( $cm^{-1}$ )	$P_G$ ( $cm^{-1}$ )	$I_D$	$I_G$	$I_D/I_G$	$FMHW_G$ ( $cm^{-1}$ )	$L_a$ (nm)
<b>N-CNT</b>	1348	1580	27484	20605	1.3	106	3.3
<b>CNT</b>	1351	1580	50108	46671	1.1	91	4.0
<b>N-G</b>	1351	1587	27788	54394	0.5	191	8.8
<b>G</b>	1351	1587	6617	60216	0.1	82	44

### 6.1.4.3 XPS Characterization

The elemental composition of the N-G and N-CNT was examined by XPS characterization. The XPS spectrum (Figure 6.7) shows three distinct peaks, which can be explained by the existence of carbon, nitrogen and oxygen atoms. The XPS wide scan signals (Figure 6.7a,e) of the pure graphene, N-G, pure CNT and N-CNT samples show C 1s, O 1s and N 1s. The C 1s spectrum of N-G (Figure 6.7b) shows the  $sp^2$  configuration indicating a majority of carbon (284.4 eV), C=N (285.3 eV), C-N (286.5 eV) and N-C=N (290.6 eV) species resulting from the structure of  $C_3N_4$ . The N 1s spectrum of N-G (Figure 6.7c) can be fitted with four individual peaks at 398.3, 400.1, 401.1 and 404.3 eV. The signal with the lowest binding energy could be attributed to two different N species: the aromatic C=N-C bonds of the  $C_3N_4$  structure and the pyridinic-N. The other signals correspond to the N-(C)<sub>3</sub> species at 400.1 eV and the C-N-H groups of the  $C_3N_4$  structure at 401.1 eV [245, 247]. The lowest peak at 404.47 eV found by Ong et al. [247], represents the typical signal in  $C_3N_4$  heterocycles which attributes to a positive charge localizations. The peaks of O 1s (Figure 6.7d) originate from C=O (531.6 eV) and C-OH or C-O-C (535.0 eV) which indicates the possible formation of pyridine  $N^+-O^-$  during the synthesis [272].

The C 1s spectrum of N-CNT (Figure 6.7f) can be described with three different signals at 284.4, 285.3, 287.2 and 290.6 eV. The main peak at 284.4 eV can be attributed to  $sp^2$  carbon, and the three smaller ones with a higher binding energy to C=N (285.3 eV), C-N (287.2 eV) and N-C=N (290.6 eV) species. The N 1s spectrum of N-CNT (Figure 6.7g) can be attributed to C=N-C, pyridinic-N (398.5 eV), C=N (400.1 eV) and N-C=N (401.0 eV) species resulting from the structure of  $C_3N_4$ . The peaks of O 1s can be attributed to the C=O (531.6 eV) and C-OH/C-O-C (535.1 eV) formed during the pyrolysis process in air. From XPS spectra, total content ratio of the samples exhibit as follows: N-G (C: 68.15 at%, O: 5.9 at%, N: 25.9 at%) and N-CNT (C: 76.3 at%, O: 4.5 at%, N: 19.2 at%).

Therefore, we assume the coexistence of pyridinic-N and  $C_3N_4$  species, resulting from the successfully coated nitrogen into the graphene and CNT.



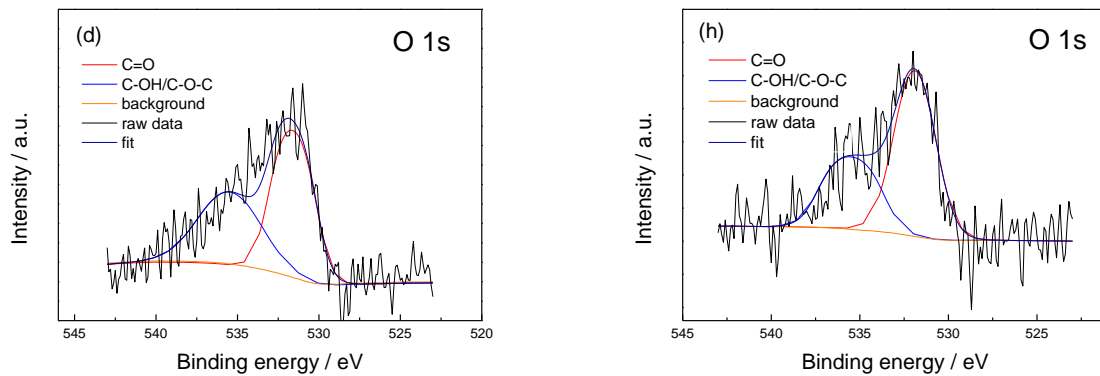


**Figure 6.7** (a) XPS wide scan signals of the pure graphene, N-G, (b) high-resolution C 1s XPS spectra, (c) N 1s spectra of N-G, (d) O 1s spectra. (e) XPS wide scan signals of pure CNT, N-CNT and (f) high-resolution C 1s XPS spectra, (g) N 1s spectra of N-CNT, (h) O 1s spectra.

## 6.1.5 Catalyst Characterization

### 6.1.5.1 SEM Analysis

The SEM images also show the mixtures of nitrogen doped carbon samples (Pt@N-G/CNT, Pt@G/N-CNT). All of samples can be seen to form a loosely packed structure in Figure 5.8. From EDX analysis, nitrogen contents of all samples of 26 ~ 28 wt% result.

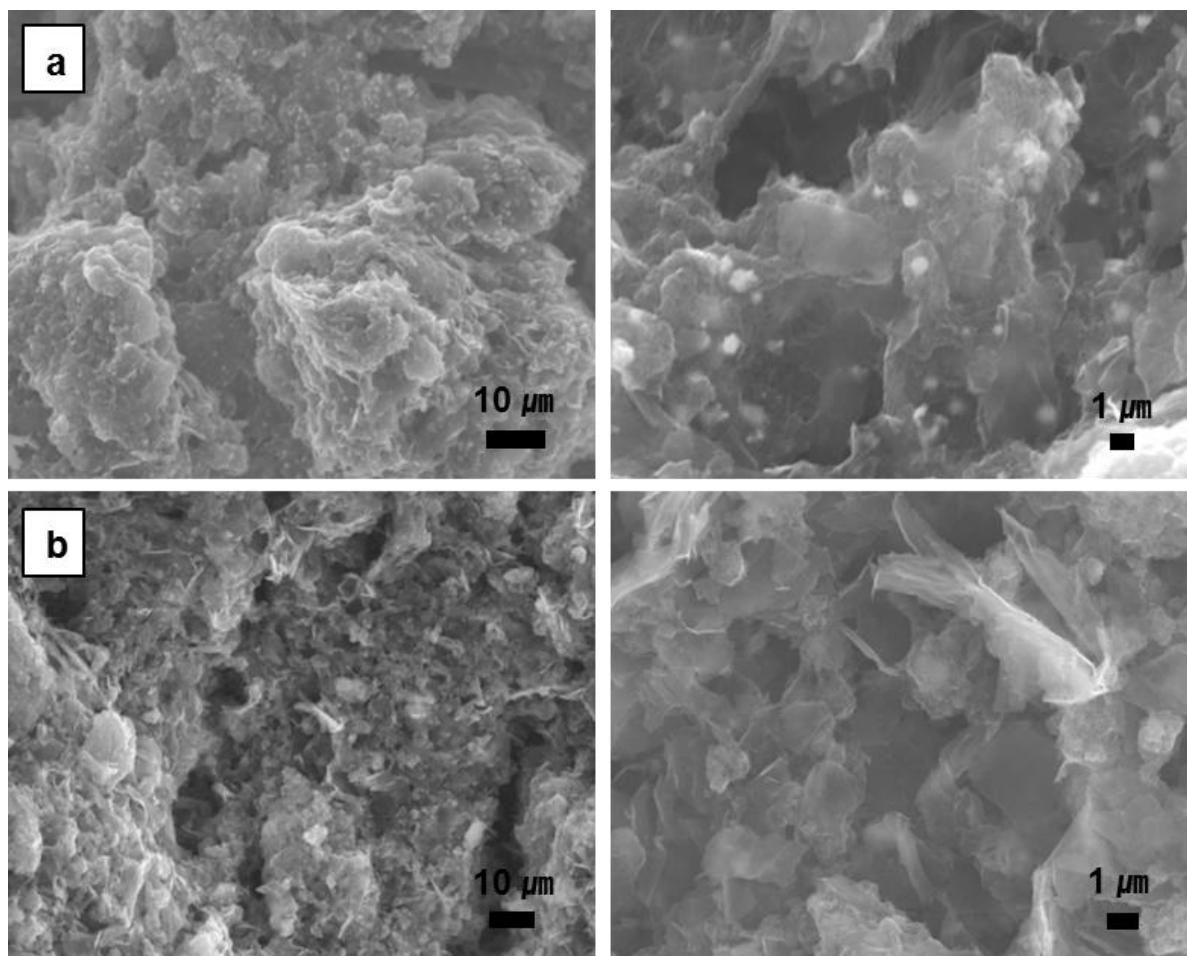


**Figure 6.8** SEM images of (a) Pt@N-G/CNT and (b) Pt@G/N-CNT.

### 6.1.5.2 TEM Analysis

The structure of the resulting electrodes was determined by TEM analysis. The TEM images (Figure 6.9) of Pt@N-G and Pt@N-CNT show that highly dispersed nanoparticles are uniformly distributed on their surface. Because of the presence of an increased number of nitrogen or the higher binding energy between Pt and nitrogen-coated carbon, Pt nanoparticles are well dispersed compared with a pristine graphene or CNT surface. The nitrogen content of the graphene and CNT samples is 22.7 at% and 19.2 at% respectively, as confirmed by EDX analysis.

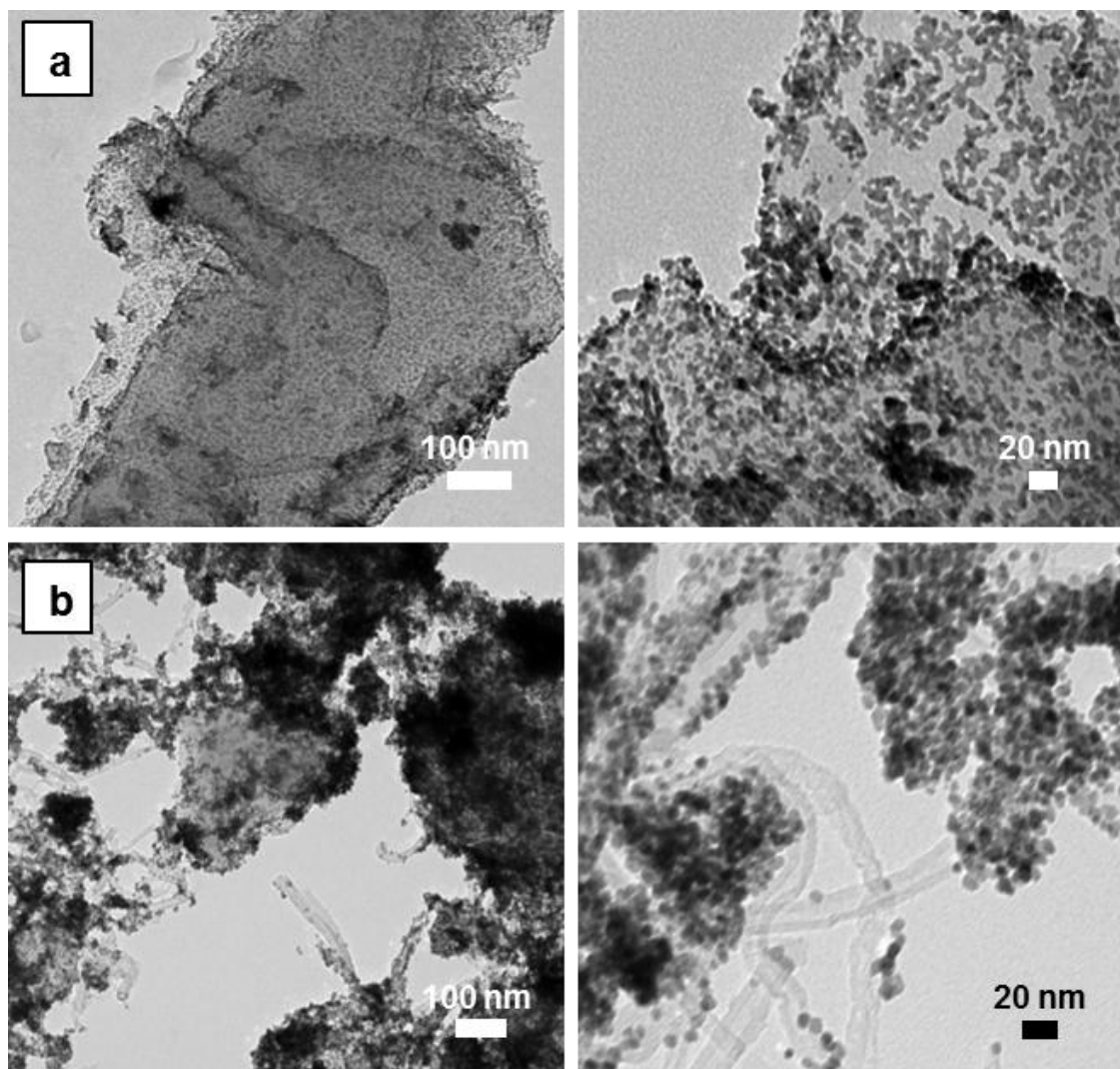


**Figure 6.9** TEM images of (a) Pt@N-G and (b) Pt@N-CNT.

### 6.1.5.3 XRD Analysis

The XRD patterns of (a) Pt@N-G and (b) Pt@N-CNT show that the strong diffraction peaks at  $2\theta = 39.8^\circ$ ,  $46.0^\circ$ ,  $68.1^\circ$  and  $81.2^\circ$  can be assigned to the characteristic (111), (002), (022) and (113) crystalline planes of Pt respectively, which possess a face-centered-cubic (fcc) structure. The size distribution of Pt nanoparticles is between 5 and 6 nm calculated from the Scherrer equation. The content of Pt nanoparticles was measured by ICP-OES (Pt loading:  $0.355 \text{ mg cm}^{-2}$  of Pt@N-G,  $0.126 \text{ mg cm}^{-2}$  of Pt@N-CNT ).

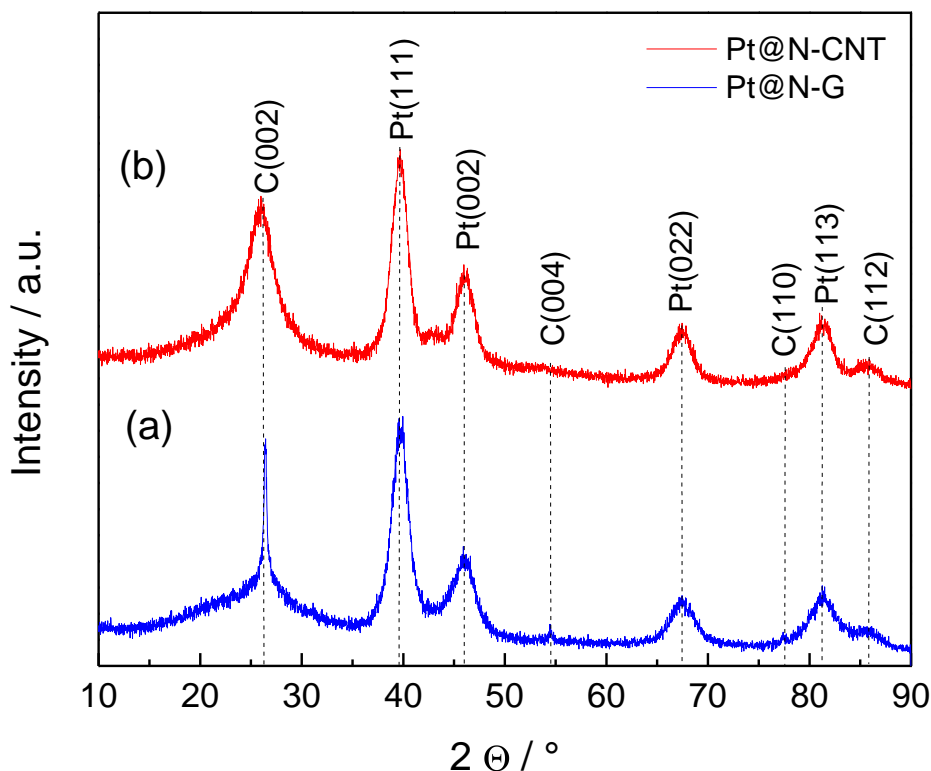


**Figure 6.10** XRD patterns of (a) Pt@N-G and (b) Pt@N-CNT.

### 6.1.6 ORR Activity

The oxygen reduction reaction can be observed in the kinetic and mixed diffusion-kinetic control regimes by performing RDE measurements. To assess their ORR catalytic activity, the Pt@N-G and Pt@N-CNT catalysts were measured by RDE in 0.1M HClO<sub>4</sub>. It is important to consider the high activity of Pt for this reaction in acid solution.

The electron transfer numbers during the ORR were calculated from the slope of the mass transport-corrected current density  $j$  at unlimited rotation rate by the Koutecky-Levich equation [273].

This measurement of the Pt@N-G and Pt@N-CNT reveals an electron transfer number of ~4.0 at 0.60–0.75 V (Figure 6.11). The half-wave potential at 1600 rpm was 0.83 V (Figure 6.11c), similar to that of Pt@C (0.86 V). Compared to the undoped samples the Pt@G and Pt@CNT exhibit high ORR catalytic activity, with an electron transfer number of about 4.0.

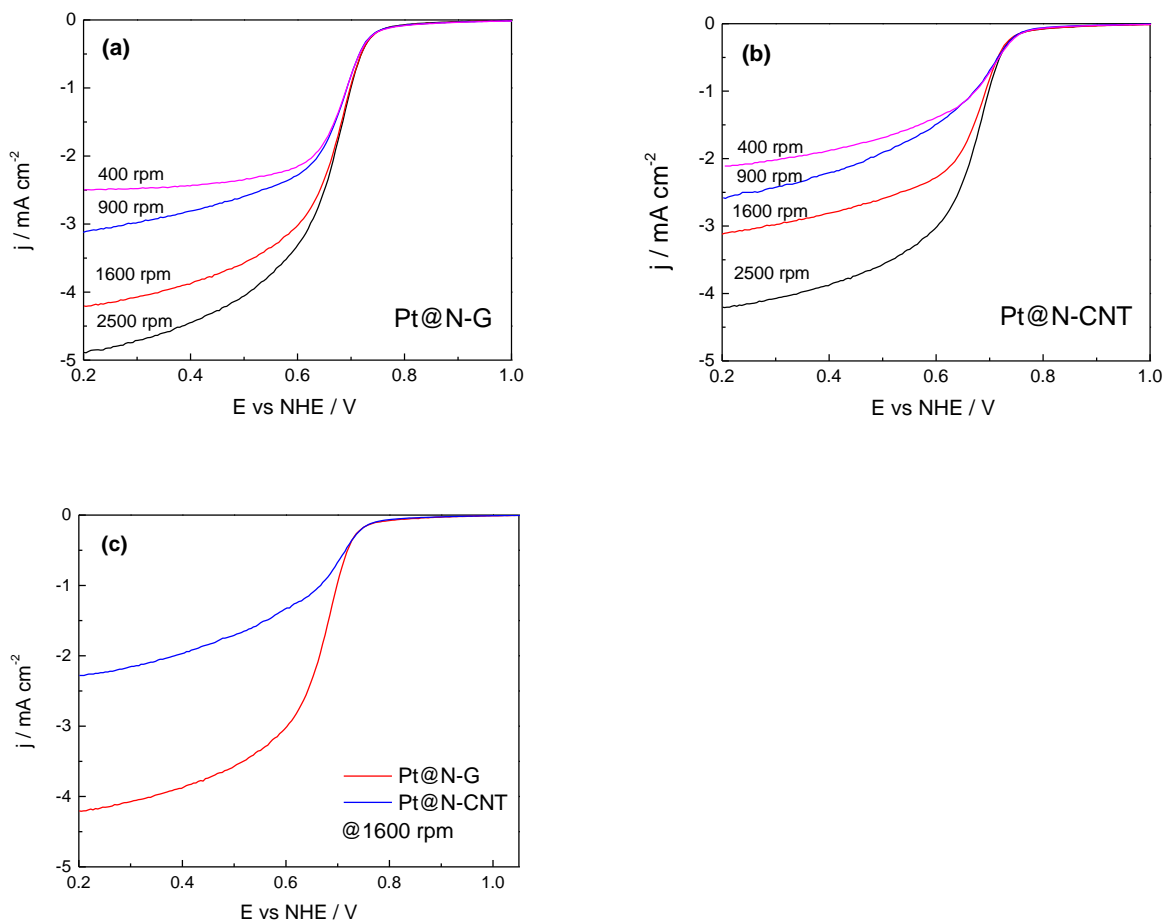


**Figure 6.11** ORR polarization curves of (a) Pt@N-G and (b) Pt@N-CNT. (c) A comparison of the polarization curves of Pt@N-G and Pt@N-CNT for 1600 rpm.

## 6.1.7 Conductivity Test

### 6.1.7.1 Ex-situ EIS with RED measurement

To proof the electronic conductivity of the prepared samples, ex-situ EIS measurements were performed of the electrochemical system. The determination of the conductivity of compressed powders has to be considered very critical due to the irreproducibility of the necessary compaction step that means the contact resistances and the formation of pores influence.

The overall electronic resistance consists of a series of resistors located along the electron conduction path (Figure 3.3). Figure 6.12 shows the Nyquist plot of four identically prepared samples (pure graphene, N-G, pure CNT and N-CNT) measured by RDE experiments. It can be seen that a relatively lower ohmic resistance for the nitrogen-coated carbon supports (N-G and N-CNT) is observed compared to the pure carbons (graphene and CNT). Thus it is demonstrate that

the ohmic resistance of N-G and N-CNT is remarkably lower and therefore it should result in a good conductivity of the electrode in PEMFC.

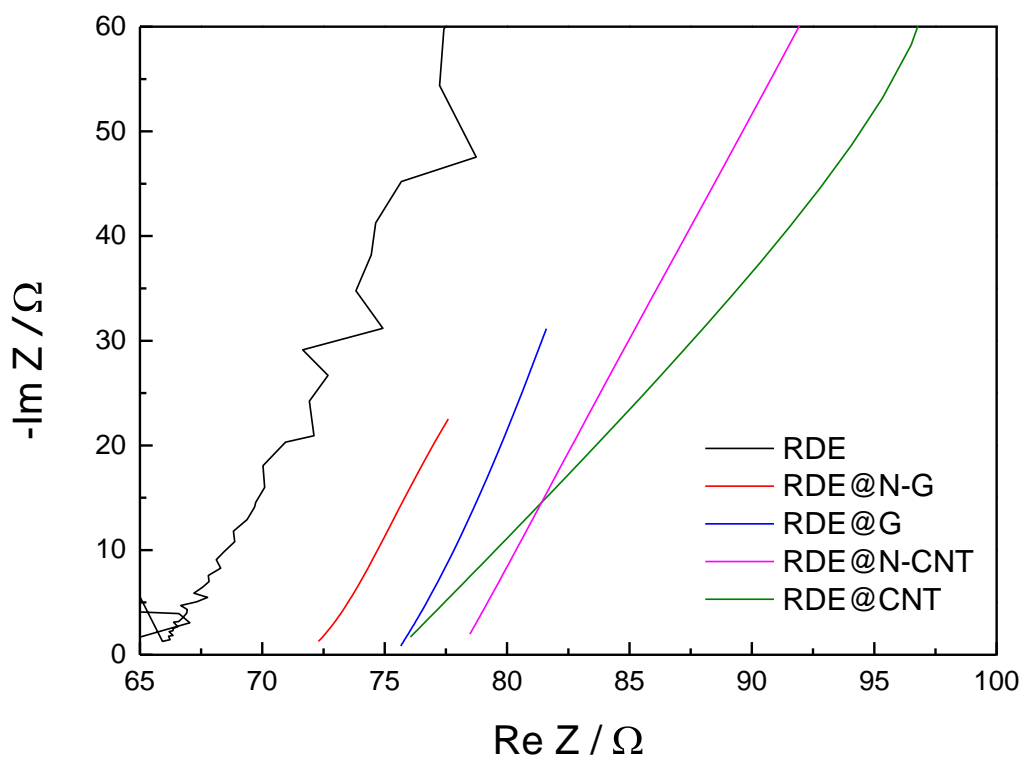


**Figure 6.12** Nyquist plots obtained from ex-situ EIS with RDE measurements in the presence of N-G and N-CNT compared with uncoated graphene (G) and CNT.

### 6.1.7.2 In-situ EIS in PEM fuel cell

In-situ EIS measurements were performed under fuel cell conditions reported in the next section in a frequency range from 10 kHz to 100 Hz (AC amplitude:  $0.2 \text{ A cm}^{-2}$ ). Du et al. report that the overall anode electronic resistance (including all components) is in the range of  $10^{-3} \text{ } \Omega$  [273] whereas the remaining MEA resistances (e.g. cathode ionic resistance, membrane resistance) are much higher ( $10^{-1} \text{ } \Omega$ ). Considering these ohmic resistances, in-situ EIS measurement have been performed and fitted with the model (Figure 3.4) [238].

It can be seen (Figure 6.13) that a well-defined semi-circle at higher frequencies is obtained at the pure carbon (Pt@G and Pt@CNT), the mixture of Pt@G/CNT and a very small semi-circle is observed for nitrogen-coated carbon catalyst supports (Pt@G/N-CNT and Pt@N-G/CNT). The diameter of the high frequency semi-circle is directly related to the hydrogen oxidation charge transfer resistance which rises in the following sequence:

Pt@G/N-CNT < Pt@N-G/CNT < Pt@G/CNT < Pt@CNT < Pt@G.

Since the catalytic activity of the anode catalyst increases with decreasing hydrogen oxidation charge transfer resistance, the catalyst activity is the highest at Pt@G/N-CNT anode. From EIS measurement we could conclude that the different  $R_{ohm}$  in 5 MEAs is caused by the different catalyst supports. The overall  $R_{ohm}$  rises in the following sequence:

Pt@G/N-CNT < Pt@N-G/CNT < Pt@G/CNT < Pt@CNT < Pt@G.

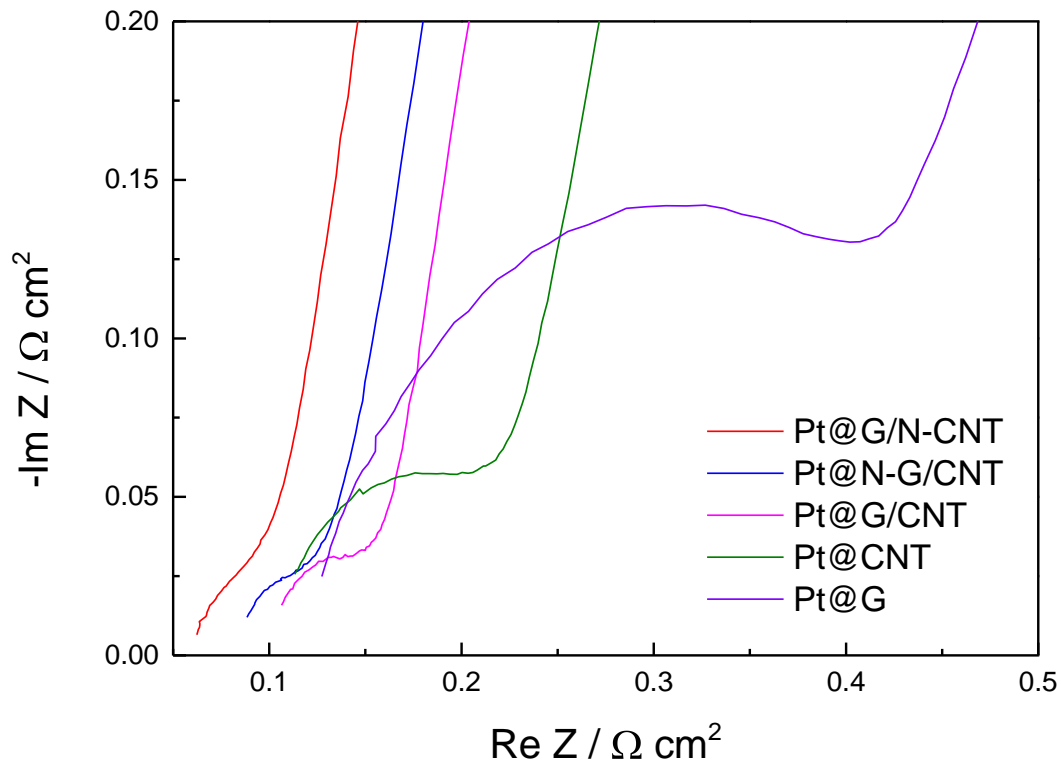


**Figure 6.13** Impedance spectra of different morphology samples measured by in-situ EIS measurement in PEM fuel cell.

The fitted results are shown in Figure 6.14 and Table 6.5. It demonstrates that the ohmic resistance of Pt@G/N-CNT remarkably decreased, and therefore it should result in a good conductivity of the electrode in PEMFC.

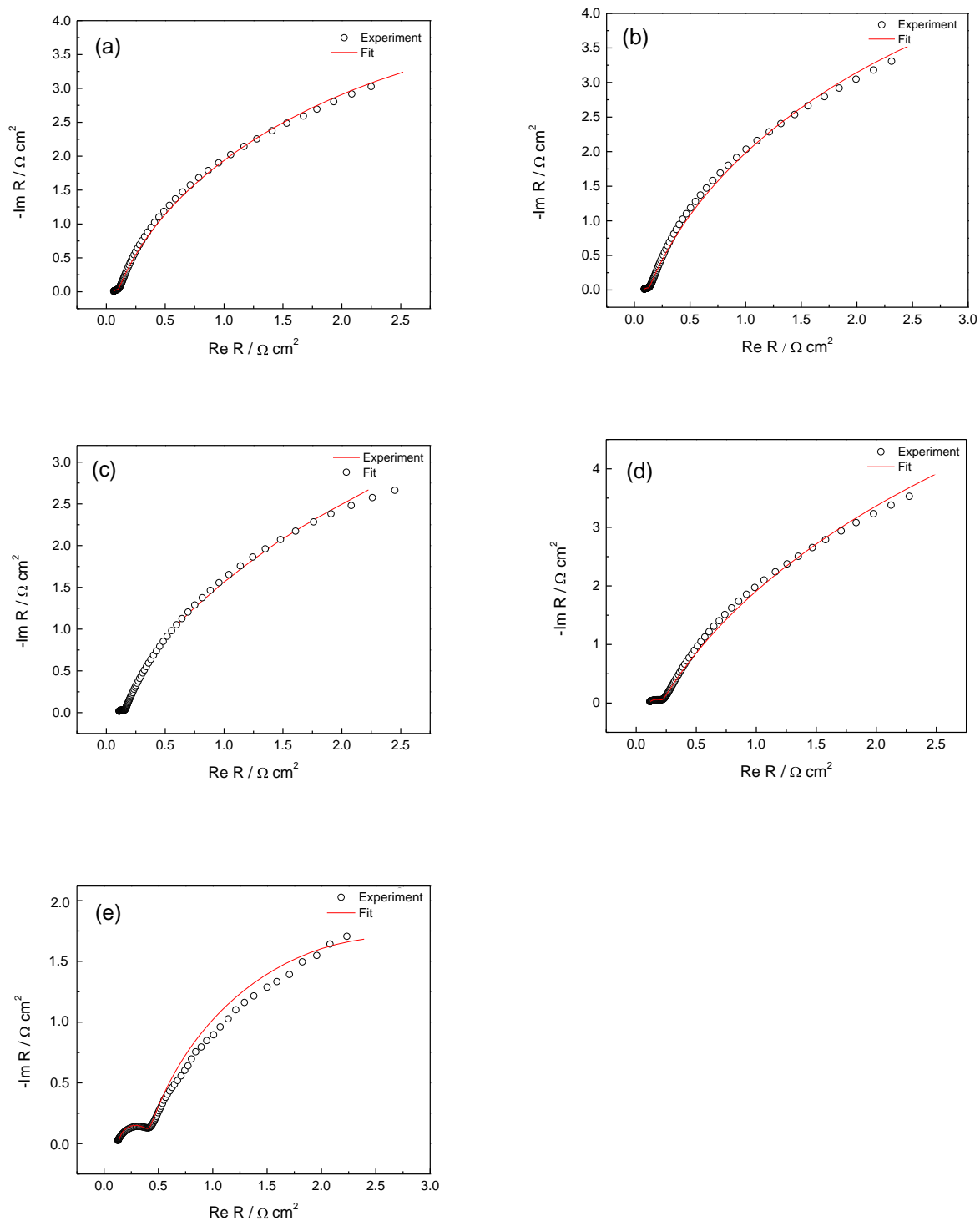


**Figure 6.14** Nyquist plots obtained from in-situ EIS measurement in PEM fuel cell of the (a) Pt@G/N-CNT, (b) Pt@N-G/CNT, (c) Pt@G/CNT, (d) Pt@CNT and (e) Pt@G.

**Table 6.5** The resultant ohmic resistance of different morphology samples obtained from in-situ EIS measurement.

<b>Anode</b>	<b>R<sub>ohm</sub></b> <b>[<math>\Omega</math> cm<sup>2</sup>]</b>	<b>R<sub>ctr</sub> anode</b> <b>[<math>\Omega</math> cm<sup>2</sup>]</b>	<b>C anode</b> <b>[mF cm<sup>2</sup>]</b>	<b>R<sub>ctr</sub> cathode</b> <b>[<math>\Omega</math> cm<sup>2</sup>]</b>	<b>C cathode</b> <b>[mF <math>\Omega</math> cm<sup>2</sup>]</b>
<b>Pt@G/N-CNT</b>	0.064	0.033	4.016	9.555	41.434
<b>Pt@N-G/CNT</b>	0.090	0.036	2.352	12.240	41.205
<b>Pt@G/CNT</b>	0.105	0.046	1.488	7.738	47.771
<b>Pt@CNT</b>	0.115	0.095	1.005	17.560	43.695
<b>Pt@G</b>	0.136	0.255	1.098	4.529	56.884

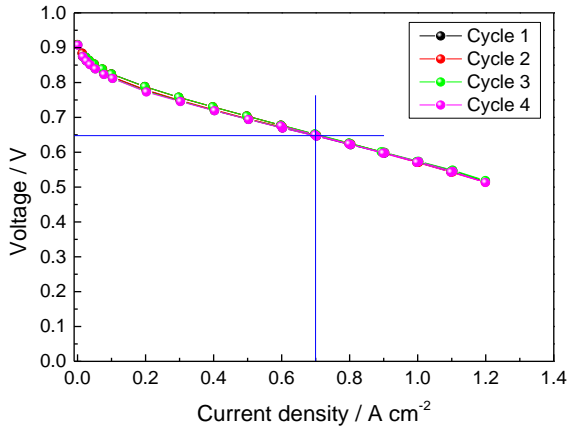
### 6.1.7.3 A fuel cell performance of MEA

The performance of MEAs consisting of an anode coated with self-made platinum catalysts supported on different carbon supports (N-G/CNT and G/N-CNT) and a commercial cathode (ELE162) measured in a fuel cell test station. The polarization curves of the MEAs were taken at two conditions with different operating temperatures (60 °C and 80 °C) and relative humidities (95% RH<sub>Anode</sub> / 95% RH<sub>Cathode</sub> and 70% RH<sub>Cathode</sub> / 50% RH<sub>Anode</sub>) with the anode coated catalyst supports.

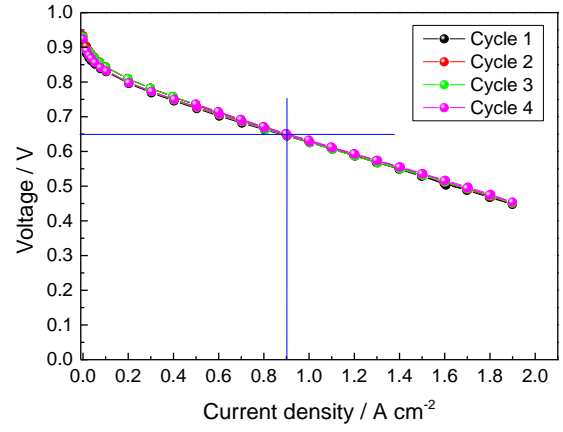
It can be seen that the current density at 0.65 V of the supported Pt catalysts (Figure 6.15) increases in the following order: Pt@G/N-CNT (0.9 A cm<sup>-2</sup>) > Pt@N-G/CNT (0.7 A cm<sup>-2</sup>). Dependence on temperature and relative humidity did not affect on optimized MEAs, which consist of N-coated graphene and CNT. These results are summarized in Table 6.6. It assumes that better stability and performance of the fuel cell MEAs result from nitrogen-containing carbon nanotube systems, which confirm the increased electronic conductivity and catalytic activity by the surface modification. These results reveal that the coated CNT electrode has a stronger influence on the MEAs than coated graphene electrode. The explanation for this behavior is the different interconnecting area of the two carbon morphologies which indicates a higher value for CNT. For this reason, the electrons move very fast in the in-plane direction of the graphene which were interconnected with very good conducting spacers. Thus it is demonstrated that the current density at 0.65 V has a high value of 0.9 A cm<sup>-2</sup> for the coated Pt@G/N-CNT sample whereas the Pt@N-G/CNT sample has a smaller value of 0.7 A cm<sup>-2</sup>.

This series of experiment shows that the design and structure of the GDE as well as the improved conductivity of the catalyst supports contribute to an increase of the performance and efficiency of PEM fuel cells.

60 °C; 70% RH<sub>Anode</sub>; 50% RH<sub>Cathode</sub>

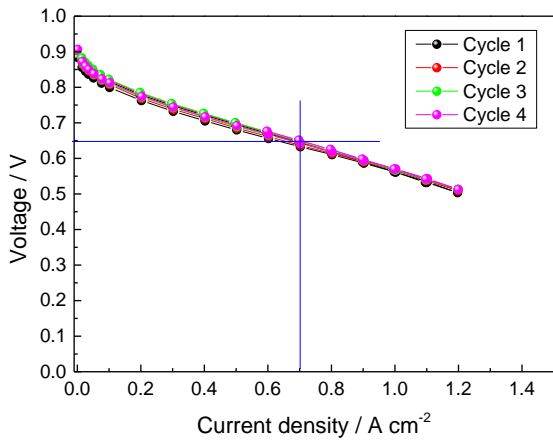


Pt@N-G/CNT

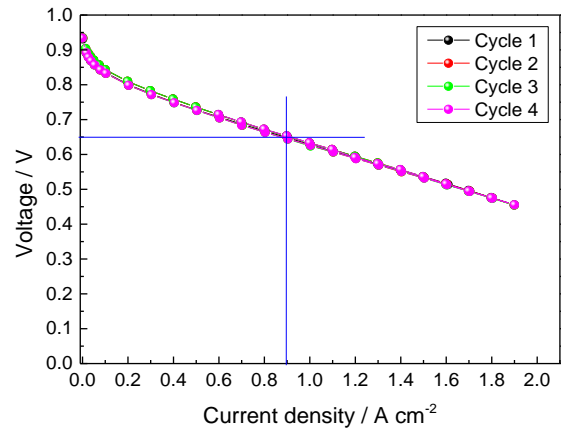


Pt@G/N-CNT

60 °C; 95% RH<sub>Anode</sub>; 95% RH<sub>Cathode</sub>



Pt@N-G/CNT



Pt@G/N-CNT

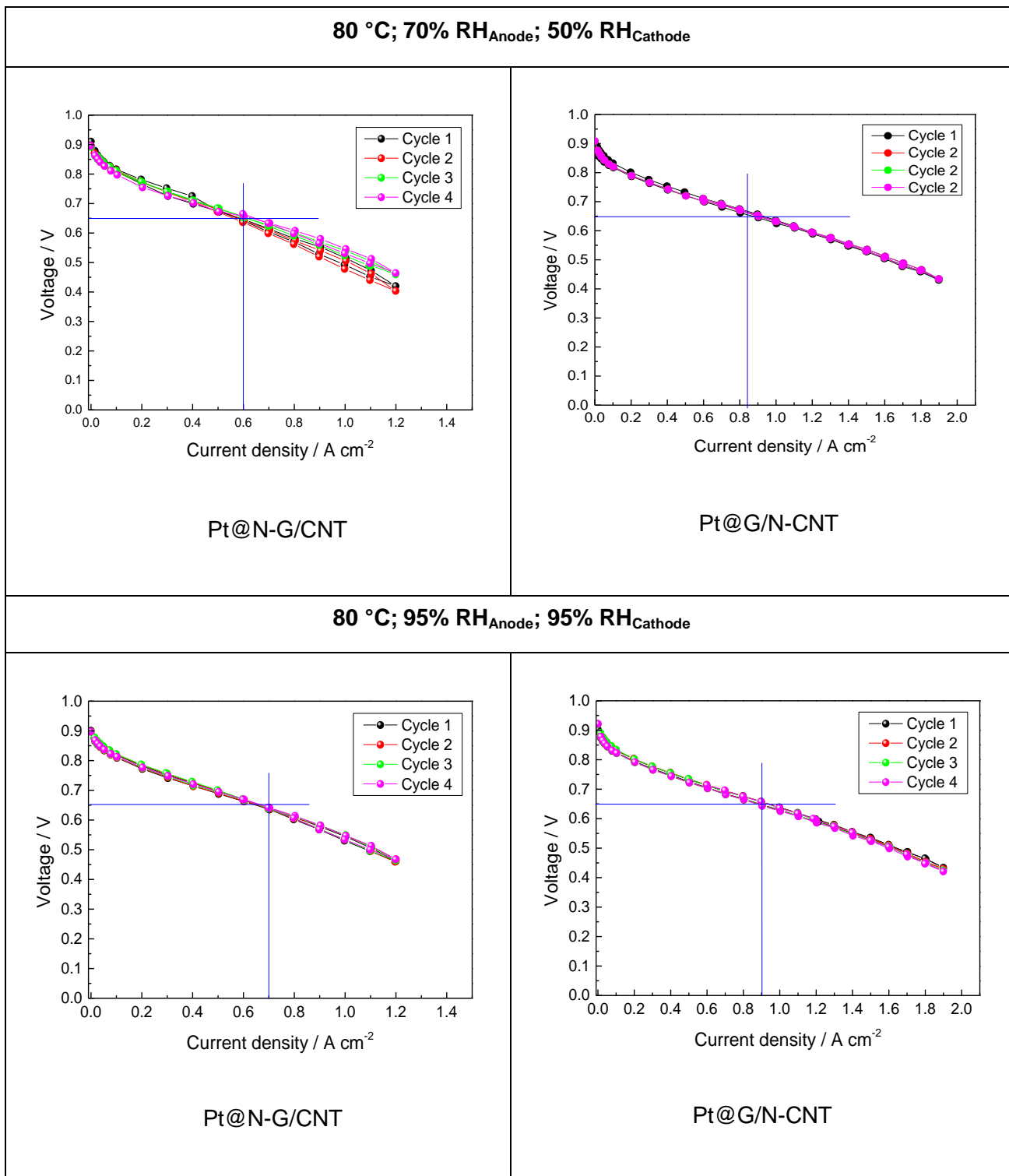


**Figure 6.15** Polarization curves of Pt@N-G/CNT and Pt@G/N-CNT measured at different operating temperatures and relative humidities.

**Table 6.6** Summary of current density at 0.65V of anode coated catalyst support operated on different conditions in PEM fuel cell.

	60 °C		80 °C	
	70% RH <sub>Anode</sub> , 50% RH <sub>Cathode</sub>	95% RH <sub>Anode</sub> , 95% RH <sub>Cathode</sub>	70% RH <sub>Anode</sub> , 50% RH <sub>Cathode</sub>	95% RH <sub>Anode</sub> , 95% RH <sub>Cathode</sub>
<b>Pt@N-G/CNT</b>	0.7 A cm <sup>-2</sup>	0.7 A cm <sup>-2</sup>	0.6 A cm <sup>-2</sup>	0.7 A cm <sup>-2</sup>
<b>Pt@G/N-CNT</b>	0.9 A cm <sup>-2</sup>			

## 6.2 Discussion

We successfully synthesized graphene- and CNT-structures with a nitrogen-containing coating using ionic liquids, with porous 3D structure. The prepared coatings have a nitrogen content of 29 wt% and microporous structure with pore size of 3 to 10 nm. XPS measurement confirms that the coatings of N-G and N-CNT consist of pyridinic-N and  $C_3N_4$  species. The N-coated graphene- and CNT-structures show remarkable physical and electro-catalytic characteristics and their performance demonstrated a higher surface area with better electronic conductivity than unmodified samples. It shows in EIS experiments that the N-G and N-CNT have a relatively low ohmic resistance compared to graphene and CNT. This property suggests that surface modification of nitrogen in the carbon is vital in the ORR process. A large N content in N-G and N-CNT materials is favorable to achieve fast electron transfer, which is desirable for ORR. The resultant electrodes were applied as a highly durable catalyst support in PEMFC, confirming the anode coated with G/N-CNT@0.025 mg  $cm^{-2}$  Pt was obtained to 0.9 A  $cm^{-2}$  of current density at 0.65 V.

## 7. Summary

Hierarchical structured carbon foams coated with a porous and conductive nitrogen-containing carbon layer has been successfully fabricated by thermal decomposition of a nitrogen containing ionic liquid (EMIM-dca). The thermal decomposition of a suited ionic liquid was applied to the surface of any carbon material (foam structures, graphene structures, CNTs, particles, etc.). In particular, hierarchical porous carbon systems consisting of nitrogen atoms could provide a good solution to the issue of poor electronic conductivity and mass transport in PEM fuel cell. In this regard, new types of carbon foams, surface modification of commercial graphene- and CNT-structures are logically demonstrated to improve the issue of properties by confirming the morphological, structural and chemical characterizations.

In the multilayer graphene foam system, the thermal decomposition of ionic liquid produces a hierarchical N-containing carbon layer. High surface area and pore volume in a GF substrate are significantly desired for enhanced applications of hierarchical porous materials. The specific surface area and pore diameter of GF and N-GF are  $477 \text{ m}^2 \text{ g}^{-1}$  and  $833 \text{ m}^2 \text{ g}^{-1}$ , respectively. The pore dimension of GF with 800 nm to 1  $\mu\text{m}$  could minimize the diffusive resistance to mass transport. Moreover, GF coated with nitrogen-containing carbon layers have high surface area for the active sites dispersion over the micro-/mesopores. Coatings with a very high level up to 35.3 wt% were realized. It could be demonstrated that a N-containing carbon layer consists of  $\text{C}_5\text{N}$ ,  $\text{C}_3\text{N}_4$  and pyridinic N-species, confirmed by XPS measurement. This result assumes that the pyridinic-N and more graphitic N-species ( $\text{C}_5\text{N}$ ,  $\text{C}_3\text{N}_4$ ) could offer more active sites to enhance the ORR activity. Structural characterisations reveal a hierarchical pore structure with macro- and micropores in the substrate and micro-/mesopores in the N-containing carbon layer. Furthermore, we could demonstrate that the N-containing carbon layer system has an increased electronic conductivity compared to the uncoated catalyst support systems measured by EIS experiments. These results demonstrate that the optimized hierarchical porous carbon foams in PEM fuel cell MEAs have ten-times higher mass activity compared to conventional CNT MEA. It could lead to a reduction of 90% lower Pt loading on fuel cell MEAs.

The new concept of coating process was extensively used for surface medication of commercial graphene and CNT surfaces. The graphene- and CNT-structures with high nitrogen content (about 29%) are a provision of anchoring sites to obtain a uniform distribution of well-defined metal particles which results in stability and high catalytic activity. Because of maintenance of their outstanding properties, such as good electronic conductivity, excellent electronic activity, and unique physicochemical properties, graphite structured N-containing porous carbons could improve

the electrochemical activity in the ORR. It is demonstrated in EIS experiments that the N-G and N-CNT have a relatively low ohmic resistance compared to the graphene and CNT. This property suggests that surface modification of nitrogen in the carbon is vital in the ORR process. A large number of N content in N-G and N-CNT materials is favorable to achieve fast electron transfer, which is desirable for the ORR. It shows remarkably that the anode coated with G/N-CNT@0.025 mg cm<sup>-2</sup> Pt were obtained to 0.9 A cm<sup>-2</sup> of current density at 0.65 V in PEMFC. These materials exhibit prominent catalytic properties, which makes them attractive for many potential applications, primarily in the field of renewable energy.

Consequently, I suggest that the hierarchical design improves the mass transport in PEM fuel cell MEAs by the formation of a very porous gas diffusion network. I propose that the new type of hierarchical porous carbon systems could enable the production of cheaper fuel cell membrane electrode assemblies.

In the following I summarize the highlights of the present thesis:

1. A hierarchical porous carbon system consisting of macro-sized carbon pores coated with a conductive nitrogen-containing carbon layer was achieved by thermal decomposition of an ionic liquid in a carbon substrate.
2. This new concept using a template-free method can modify any kind of carbon materials with a high specific surface area and excellent physical and morphological properties.
3. The electrical conductivity of nitrogen-containing porous carbons is enhanced compared to the unmodified samples. The increased conductivity results from the high level of nitrogen coating up to 35 wt%.
4. This special structural material design of the hierarchical structured nitrogen-containing porous carbons was optimized for applications/processes in which the diffusion of educt/products plays a crucial role.

## 8. Outlook

The introduction of micro-/mesopores into a macroporous substrate has shown significant benefits for their catalytic activity and stability. Given their rich properties, hierarchical porous carbons are potential candidates for energy storages and generations, especially as supercapacitor electrode materials, Li-ion adsorption-desorption in batteries, and fuel cell catalysts.

Hierarchical porous carbons with heteroatom such phosphorus, boron doping would be the selection for the fabrication of new generation electrodes for highly efficient electrocatalysts in ORR and OER through a favorable direct four-electron reaction pathway. Strategies for deriving heteroatom-doped carbons can be developed from different ionic liquids following by coating process. Obviously, the choice of an ionic liquid as a precursor plays a critical role in obtaining desirable porosities in the  $sp^2$ -bonded carbons and N-doping can considerably enhance their energy related applications.

Moreover, it could be feasible to replace the expensive of precious metal by exploring precursors, which are low-cost, readily available and renewable. This could play a key role for conventional applications. For example, the use of potential raw materials like biorenewable resources or biomass as a carbon source have to be explored for the design of hierarchical porous carbons with a network of pores.

For further pore optimization/functionalization, the control of textural properties, such as pore size and volume, must be maximized to improve power densities and electrochemical stability. Also the heteroatom-containing graphitic carbon structures can be optimized by pyrolysis at high temperatures. Study on the catalytic mechanism and kinetics will be also desirable in order to design and develop rationally carbon-based metal-free catalysts with a desirable activity and durability.

## 9. Appendix

### 9.1 List of Figures

**Figure 2.1** Schematic illustration of PEMFC.

**Figure 2.2** Typical fuel cell polarization curve with labeled regions of loss.

**Figure 2.3** Fuel-cell components.

**Figure 2.4** Chemical structure of perfluorinated sulfonic acid ionomer with different types of membranes.

**Figure 2.5** SEM images of gas diffusion layer morphology.

**Figure 2.6** Typical flow channels designs; (a) Serpentine, (b) Parallel, (c) Interdigitated, (d) Pin.

**Figure 2.7** Graphical representation of the reaction sites.

**Figure 2.8** Schematic illustration of nitrogen species in N-containing graphitic carbons.

**Figure 2.9** Schematic presentation of ORR pathway.

**Figure 3.1** Classification of hysteresis loops and pore types.

**Figure 3.2** Linear sweep voltammogram of Pt@C (0.2 – 1.1 V vs. RHE, 5 mV s<sup>-1</sup>, 1600 rpm, saturated-O<sub>2</sub>, 0.1M HClO<sub>4</sub>).

**Figure 3.3** Scheme of ex-situ electrochemical impedance spectroscopy.

**Figure 3.4** The equivalent circuit used for fitting of the EIS plots.

**Figure 3.5** CV of Pt@N-GF (0.05 – 1.1 V vs. RHE, 20 mV s<sup>-1</sup>, 0.1 M HClO<sub>4</sub>).

**Figure 4.1** Illustration for the synthesis of hierarchical structured multilayer graphene foams coated with N-containing carbon layers.

**Figure 5.1** Scheme of the new hierarchically structured carbon foam concept used for electrocatalytical processes.

**Figure 5.2** Element compositions of the pure IL and N-GF prepared with different EMIM-dca contents and temperatures.

**Figure 5.3** Morphology and structures of GF and N-GF. (a,b) SEM images of GF (scale bars: 10 μm, b: 1 μm and insert 200 nm); (c) SEM images of N-GF (scale bars: 1 μm, insert: 200 nm); (d) SEM image of N-GF (scale bar: 100 nm).

**Figure 5.4** TEM images of the surfaces of GF (a) and N-GF (b) show the microporous structure. The inserted schemes illustrate their surface structures before and after the coating process. Cross section of a N-GF pore lamella (c) and a high resolution TEM of the coated GF (d).

**Figure 5.5** The specific surface area and pore size distribution of GF and N-GF. BET isotherms of GF (a) and N-GF (c); Pore-size distribution of the GF (b) and N-GF (d) measured by nitrogen adsorption–desorption.

**Figure 5.6** Characterization of GF and N-GF by XPS. (a) XPS survey spectra of GF (black curve) and N-GF (red); (b,c) High-resolution of C 1s XPS spectra (b) and O 1s spectra (c) of the GF; (d-f) High-resolution C 1s XPS spectra (d), N 1s spectra (e) and O 1s spectra (f) of the N-GF.

**Figure 5.7** XRD patterns of the (a) GF and (b) N-GF structures.

**Figure 5.8** Raman spectroscopy of the GF and N-GF measured with a wavelength of 633 nm (a) and temperature dependence of N-GF between 600 °C and 1000 °C (b).

**Figure 5.9** Structure characterization of Pt@N-GF.

**Figure 5.10** TEM images of Pt catalysts deposited on the inner side of the N-GF mesopores.

**Figure 5.11** EDX measurement of N-GF.

**Figure 5.12** Electrochemical impedance spectroscopy of GF and N-GF.

**Figure 5.13** Oxygen reduction reaction of the (a) Pt@GF, (b) Pt@N-GF and (c) Pt@C at rotation speeds of 200 – 2000 rpm in O<sub>2</sub>-saturated 0.1 M HClO<sub>4</sub>. (d) Compared ORR polarization curves of 32.2 wt%Pt@GF, 7.7 wt%Pt@N-GF and 40 wt%Pt@C measured by RDE experiments at 1600 rpm.

**Figure 5.14** (a) Koutecky – Levich plots of 32.2 wt%Pt@GF and 7.7 wt%Pt@N-GF measured by RDE experiments at 0.6 V vs NHE in 0.1M HClO<sub>4</sub> at 25 °C. (b) The K-L plots of 40 wt%Pt@C (JM) was performed between 0.9 V and 0.7 V.

**Figure 5.15** CVs of (a) Pt@GF and (b) Pt@N-GF were taken at a scan rate of 20 mV s<sup>-1</sup> in N<sub>2</sub>-saturated HClO<sub>4</sub>. (c) ECSA of Pt@GF (red column) and Pt@N-GF (black column) calculated from H<sub>2</sub>-desorption regions of CV measurements.

**Figure 5.16** Fuel cell test station measurement for self-prepared anodes. (a) current density of an anode coated with GF (Pt loading: 0.322 mg cm<sup>-2</sup>) or N-GF (Pt loading: 0.077 mg cm<sup>-2</sup>) at 80 °C; (b) current density and power density of Pt@N-GF; (c) polarization curves of MEAs prepared with different catalyst supports; and (d) Tafel representation of cell voltage (V) vs Pt mass activity (A/mg<sub>Pt</sub>).

**Figure 6.1** Scheme of different carbon morphologies: (a) graphene, (b) CNT, (c) G/CNT, (d) N-G/CNT and (e) G/N-CNT.

**Figure 6.2** SEM images of commercial (a) AO-2 graphene, (b) C150P nanotubes and nitrogen-coated (c) N-G, (d) N-CNT.

**Figure 6.3** TEM images of (a) AO-2 graphene, (b) CNT, (c) N-G and (d) N-CNT.

**Figure 6.4** XRD patterns of (a) pure AO-2, N-G and (b) pure CNT, N-CNT.

**Figure 6.5** N<sub>2</sub> adsorption-desorption isotherms for (a) the graphene and N-G, (c) CNT and N-CNT; pore diameter for (b) the N-G and (d) N-CNT.

**Figure 6.6** Raman spectra of (a) pure graphene, (b) N-G, (c) pure CNT and (d) N-CNT.

**Figure 6.7** (a) XPS wide scan signals of the pure graphene, N-G, (b) high-resolution C 1s XPS spectra, (c) N 1s spectra of N-G, (d) O 1s spectra. (e) XPS wide scan signals of pure CNT, N-CNT and (f) high-resolution C 1s XPS spectra, (g) N 1s spectra of N-CNT, (h) O 1s spectra.

**Figure 6.8** SEM images of (a) Pt@N-G/CNT and (b) Pt@G/N-CNT.

**Figure 6.9** TEM images of (a) Pt@N-G and (b) Pt@N-CNT.

**Figure 6.10** XRD patterns of (a) Pt@N-G and (b) Pt@N-CNT

**Figure 6.11** ORR polarization curves of (a) Pt@N-G and (b) Pt@N-CNT. (c) The compared polarization curves of Pt@N-G and Pt@N-CNT by provided for 1600 rpm.

**Figure 6.12** Nyquist plots obtained from ex-situ EIS with RDE measurements in the presence of N-G and N-CNT compared with uncoated graphene (G) and CNT.

**Figure 6.13** Impedance spectra of different morphology samples measured by in-situ EIS measurement in PEM fuel cell.

**Figure 6.14** Nyquist plots obtained from in-situ EIS measurement in PEM fuel cell of the (a) Pt@G/N-CNT, (b) Pt@N-G/CNT, (c) Pt@G/CNT, (d) Pt@CNT and (e) Pt@G.

**Figure 6.15** Polarization curves of Pt@N-G/CNT and Pt@G/N-CNT measured at different operating temperatures and relative humidities.

## 9.2 List of Tables

**Table 2.1** Different types of fuel cells and characteristics.

**Table 2.2** Types of carbonaceous support materials for PEMFC: properties, catalysts and observations.

**Table 2.3** Thermodynamic electrode potentials of electrochemical O<sub>2</sub> reductions.

**Table 4.1** Carbon supports for Pt catalyst.

**Table 5.1** Element compositions of the GF and N-GF prepared with different EMIM-dca contents and temperatures.

**Table 5.2** Evaluation of Raman spectra measured on GF and N-GF samples prepared at different temperatures. P indicates the position, I the intensity, FWHM<sub>G</sub> the peak breath of a Lorentzian fitting function, and La the size of undistorted carbon domains.

**Table 5.3** Summary of the results obtained by RDE experiments in 0.1M HClO<sub>4</sub>.

**Table 6.1** Element compositions of the N-G and N-CNT prepared with different EMIM-dca contents and temperatures.

**Table 6.2** Element composition of N-G and N-CNT measured by EDX.

**Table 6.3** Porous properties of graphene, CNT, N-G and N-CNT.

**Table 6.4** Evaluation of Raman spectra prepared at different temperatures. P indicates the position, I the intensity, FWHM<sub>G</sub> the peak breath of a Lorentzian fitting function, and La the size of undistorted carbon domains.

**Table 6.5** The resultant ohmic resistance of different morphology samples obtained from in-situ EIS measurement.

### 9.3 Acknowledgements

This work would not have been possible without the support, guidance, efforts, and friendship of many people.

First and foremost, I would like to thank my advisor, Prof. Dr. Rolf Hempelmann for giving me the great opportunity, for providing fruitful ideas and for showing his support throughout this study. He has been a true inspiration to me. His guidance and mentoring have helped me become a better researcher.

I really appreciate PD. Dr. Harald Natter for providing me with invaluable advice and with all the support in my experiments. I learned how to approach scientific and logical thinking, during the PhD study. I would also like to thank Sylvia Kuhn for the SEM, TEM measurements. Thanks to Reiner Wintringer for the CHN analysis and Marco Zeiger for Raman spectroscopy measurement. I would like to thank my colleague, Dan Durneata for the discussion and for the help in technical problems.

Special thanks to Dr. Ivan Radev (Duisberg), who measured all of my coating samples for the electronic conductivity. I gratefully thank Dr. Valentin Nica for showing many expert skills related to research. His enthusiastic supports and efforts helped me to the completion of PhD work by connecting the XPS, BET and Raman spectroscopy operators in Prof. Stancu's group (Iasi). Furthermore, I would like to thank all my committee members for their insightful inputs on my dissertation and positive feedback during all the conversations.

This PhD would not have been possible without the unrelenting support and the backing of my family. I sincerely thank my parents Mr. Giseok Oh and Mrs. Jeongrye Kim for their love, encouragement, and understanding. Thank you both for providing the strength to accomplish my goals. Special thanks go to my sisters Sungum, Ranhee, Kahee for their love, support, and belief in me.

This work was financially supported by the AiF (Arbeitsgemeinschaft industrieller Forschungsvereinigungen "Otto von Guericke" e.V.) in the framework of the Projekt ISECD (Nr. 18128 N) "Elektrochemische Verfahren zur Herstellung von Gasdiffusionselektroden für PEM-Brennstoffzellen". I wish to thank our industrial project partners Dr. Peinecke, Dr. Baumgärtner, Dr. Freudenberger for organizing the projects and their valuable advice.

## 9.4 References

- [1] N. Rajalakshmi, N. Lakshmi, K. S. Dhathathreyan, *Int. J. Hydrogen Energy*, 2008, 33, 7521.
- [2] H. P. Bennetto, J. L. Stirling, K. Tanaka, C. A. Vega, *Biotechnol. Bioeng.*, 1983, 25, 559.
- [3] E. Ticianelli, C. Derouin, A. Redondo, S. Srinivasan, *J. Electrochem. Soc.*, 1988, 135, 2209.
- [4] O. Yamamoto, Y. Takeda, R. Kanno, M. Noda, *Solid State Ionics*, 1987, 22, 241.
- [5] K. S. Howe, K. Kendall, *J. Fuel Cell Sci. Technol.*, 2011, 8, 034502.
- [6] H. Qiao, M. Kunimatsu, T. Okada, *J Power Sources*, 2005, 139, 30.
- [7] L. Zhang, L. Wang, C. M. B. Holt, B. Zahiri, Z. Li, K. Malek, et al., *Energy Environ. Sci.*, 2012, 5, 6156.
- [8] J. -H. Jang, J. Kim, Y. -H. Lee, I. Y. Kim, M. -H. Park, C. -W. Yang, *Energy Environ. Sci.*, 2011, 4, 4947.
- [9] Y. Tan, C. Xu, G. Chen, N. Zheng, Q. Xie, *Energy Environ. Sci.*, 2012, 5, 6923.
- [10] Y. C. Xing, *J. Phys. Chem. B*, 2004, 108, 19255.
- [11] S. Ohyagi, T. Matsuda, Y. Iseki, T. Sasaki, C. Kaito, *J. Power Sources*, 2011, 196, 3743.
- [12] M. Lefevre, E. Proietti, F. Jaouen, J. P. Dodelet, *Science*, 2009, 324, 71.
- [13] R. Bashyam, P. Zelenay, *Nature*, 2006, 443, 63.
- [14] F. Y. Cheng, Y. Su, J. Liang, Z. L. Tao, J. Chen, *Chem. Mater.*, 2010, 22, 898.
- [15] K. P. Gong, F. Du, Z. H. Xia, M. Durstock, L. M. Dai, *Science*, 2009, 323, 760.
- [16] L. T. Qu, Y. Liu, J. B. Baek, L. M. Dai, *ACS Nano*, 2014, 4, 1321.
- [17] R. L. Liu, D. Q. Wu, X. L. Feng, K. Müllen, *Ang. Chem.*, 2010, 49, 2565.
- [18] D. S. Geng, Y. Chen, Y. G. Chen, Y. L. Li, R. Y. Li, X. L. Sun, *Energy Environ. Sci.*, 2011, 4, 760.
- [19] H. -J. Choi, S.-M. Jung, J.-M. Seo, D.W. Chang, L. Dai, J.-B. Baek, *Nano Energy*, 2012, 1 534.
- [20] M. Zhang, L. Dai, *Nano Energy*, 2012, 1, 514.
- [21] S. L. Candelaria, Y. Shao, W. Zhou, X. Li, J. Xiao, J.-G. Zhang, *Nano Energy*, 2012, 1, 195.
- [22] D. C. Wei, Y. Q. Liu, Y. Wang, H. L. Zhang, L. P. Huang, G. Yu, *Nano Letters*, 2009, 9, 1752.
- [23] X. R. Wang, X. L. Li, L. Zhang, Y. Yoon, P. K. Weber, H. L. Wang, *Science*, 2009, 324, 768.
- [24] L. S. Panchokarla, K. S. Subrahmanyam, S. K. Saha, A. Govindaraj, H. R. Krishnamurthy, U. V. Waghmare, *Adv. Mater.*, 2009, 21, 4726.
- [25] H. M. Jeong, J. W. Lee, W. H. Shin, Y. J. Choi, H. J. Shin, J. K. Kang, *Nano Lett.*, 2011, 11, 2472.
- [26] Y. Wang, Y. Y. Shao, D. W. Matson, J. H. Li, Y. H. Lin, *ACS Nano*, 2010, 4, 1790.
- [27] Z. Q. Niu, J. Chen, H. H. Hng, J. Ma, X. D. Chen, *Adv. Mater.*, 2012, 24, 4144.
- [28] H. Y. Sun, Z. Xu, C. Gao, *Adv. Mater.*, 2013, 25, 2554.
- [29] Z. Xu, Y. Zhang, P. G. Li, C. Gao, *ACS Nano*, 2012, 6, 7103.
- [30] H. Hu, Z. B. Zhao, W. B. Wan, Y. Gogotsi, J. S. Qiu, *Adv. Mater.*, 2013, 25, 2219.

- [31] C. H. Wang, X. D. He, Y. Y. Shang, Q. Y. Peng, Y. Y. Qin, E. Z. Shi, Y. B. Yang, S. T. Wu, W. J. Xu, S. Y. Du, A. Y. Cao, Y. B. Li, *J. Mater. Chem. A*, 2014, 2, 14994.
- [32] F. Liu, T. S. Seo, *Adv. Funct. Mater.*, 2010, 20, 1930.
- [33] Y. X. Xu, K. X. Sheng, C. Li, G. Q. Shi, *ACS Nano*, 2010, 4, 4324.
- [34] B. Tang, G. X. Hu, H. Y. Gao, Z. X. Shi, *J. Power Sources*, 2013, 234, 60.
- [35] J. J. Liu, W. Lv, W. Wei, C. Zhang, Z. J. Li, B. H. Li, F. Y. Kang, Q. H. Yang, *J. Mater. Chem. A*, 2014, 2, 3031.
- [36] Bai, H., Sheng, K., Zhang, P., Li, C. & Shi, G., *J. Mater. Chem.* 2011, 21, 18653.
- [37] Wei, H., Xu, M.-W., Bao, S.-J., Yang, F. & Chai, H, *RSC Adv.*, 2014, 4, 16979.
- [38] Guo, Z., Jiang, C., Teng, C., Ren, G., Zhu, Y. & Jiang, L., *ACS Appl. Mater. Interfaces*, 2014, 6, 21454.
- [39] H. M. F. Amin, Thesis, 2009/2010.
- [40] N. Sammes, *Fuel Cell Technology: Reaching Towards Commercialization*, Springer, London, 2006.
- [41] L. J. M. J. Blomen, M. N. Mugerwa, *Fuel Cell Systems*, Plenum Press, New York, 1993.
- [42] M. M. Mench, *Fuel Cell Engines*, John Wiley and Sons Ltd., London, 2008.
- [43] G. D. J. Harper, *Fuel Cell Projects for the Evil Genius*, 2008.
- [44] S. Srinivasan, *Fuel Cells: From Fundamentals to Applications*, Springer Verlag, 2006.
- [45] A. Hermann, T. Chaudhuri, P. Spagnol, *Int. J. Hydrogen Energy*, 2005, 30, 1297.
- [46] S. Giddey, S. P. S. Badwal, A. Kulkarni, Munnings, C., *Progress Energy Combust. Sci.*, 2012, 38, 360.
- [47] <https://www.scientific-computing.com/feature/fuel-thought-cars-future>
- [48] <http://www.sigmaaldrich.com/technical-documents/articles/materials-science/perfluorosulfonic-acid-membranes.html>
- [49] H. S. Chu, C. Yeh, F. Chen, *J. Power Sources*, 2003, 123, 1.
- [50] Y. Yu, Z.K. Tu, Z.G. Zhan, M. Pan, *Int. J. Energy Res*, 2012, 36, 845.
- [51] Y. Tang, W. Yuan, M. Q. Pan, Z. P. Wan, *Int. J. Hydrogen Energy.*, 2010,35,9661.
- [52] Y. Tang, W. Zhou, M. Pan, H. Chen, W. Liu, H. Yu, *Int. J. Hydrogen Energy*, 2008, 33, 2950.
- [53] Y. Fu, G.Q. Lin, M. Hou, B. Wu, H.K. Li, L.X. Hao, *Int. J. Hydrogen Energy*, 2009, 34, 453.
- [54] Y. Tang, W. Yuan, M. Pan, Z. Li, G. Chen, Y. Li, *Appl. Energy.*, 2010, 87, 1410.
- [55] X. Li, I. Sabir., *Int. J. Hydrogen Energy*, 2005, 30, 359.
- [56] M. M. Mench, C. -Y. Wang, S. T. Thynell, *J. Transport Phenomena*, 2001, 3, 151.
- [57] Y. Lin, X. Cui, X. Ye, *Electrochem. Commun.*, 2005, 7, 267.
- [58] W. Z. Li, C. H. Liang, W. J. Zhou, J. S. Qiu, Z. H. Zhou, G. Q. Sun, Q. Xin, *J. Phys. Chem. B*, 2003, 107, 6292.
- [59] C. Wang, M. Waje, X. Wang, J. M. Tang, R. C. Haddon, Y. S. Yan, *Nano Lett.*, 2004, 4, 345.

- [60] C. A. Bessel, K. Laubernds, N. M. Rodriguez, R. T. K. Baker, *J. Phys. Chem. B*, 2001, 105, 1115.
- [61] S. H. Joo, S. J. Choi, I. Oh, J. Kwak, Z. Liu, O. Terasaki, R. Ryoo, *Nature*, 2001, 412, 169.
- [62] H. Chhina, S. Campbell, O. Kesler, *J. Power Sources*, 2006, 161, 893.
- [63] R. Ganesan, J. S. Lee, *Angew. Chem.-Int. Edit.*, 2005, 44, 6557.
- [64] H. X. Zhong, H. M. Zhang, G. Liu, Y. M. Liang, J. W. Hu, B. L. Yi, *Electrochem. Comm.*, 2006, 8, 707.
- [65] Y. Shao, J. Sui, G. Yin, Y. Gao, *Applied Catalysis B: Environmental*, 2008, 79, 89.
- [66] G. Wu, D. Y. Li, C. S. Dai, D. L. Wang, N. Li, *Langmuir*, 2008, 24, 3566.
- [67] G. Chen, D. G. Xia, Z. R. Nie, Z. Y. Wang, L. Wang, L. Zhang, J. Zhang, *J. Chem. Mater.*, 2007, 19, 1840.
- [68] B. D. McNicol, R. T. Short, *J. Electroanal. Chem.*, 1977, 81, 249.
- [69] S. R. Brankovic, J. McBreen, R. R. Adzic, *J. Electroanal. Chem.*, 2001, 503, 99.
- [70] S. R. Brankovic, Wang, J. X. Adzic, R. R. *Electrochem. Solid-State Lett.*, 2001, 4, A217.
- [71] K. Mo. Sasaki, Y. J. X. Wang, M. Balasubramanian, F. Uribe, J. McBreen, R. R. Adzic, *Electrochim. Acta*, 2003, 48, 3841.
- [72] J. Zhang, Y. Mo, M. B. Vukmirovic, R. Klie, K. Sasaki, R. R. Adzic, *J. Phys. Chem. B*, 2004, 108, 10955.
- [73] J. Zhang, M. B. Vukmirovic, Y. Xu, M. Mavrikakis, R. R. Adzic, *Angew. Chem. Int. Ed.*, 2005, 44, 2132.
- [74] H. Naohara, S. Ye, K. Uosaki, *Electrochim. Acta*, 2000, 45, 3305.
- [75] S. R. Brankovic, J. McBreen, R. R. Adzic, *Surf. Sci.*, 2001, 479, L363.
- [76] X. Sun, R. Li, D. Villers, J. P. Dodelet, S. Desilets, *Chem. Phys. Lett.*, 2003, 379, 99–104.
- [77] A. L. Dicks, *J. Power Sources*, 2006, 156, 128.
- [78] H. Chang, S.H. Joo, C. Pak, *J. Mater. Chem.*, 2007, 17, 3078.
- [79] R. Ryoo et al., *Advanced Materials*, 2001, 13, 677.
- [80] H. Yang, D. Zhao, *J. Mater. Chem.*, 2005, 15, 1217.
- [81] A. H. Lu, F. Schüth, *Adv. Mater.*, 2006, 18, 1793.
- [82] J. Lee, J. Kim, T. Hyeon, *Adv. Mater.*, 2006, 18, 2073.
- [83] T. Kyotani, *Carbon*, 2000, 38, 269.
- [84] J. C. Ndamanisha, L.-p. Guo, *Analytica Chimica Acta*, 2012, 747, 19.
- [85] L. Guo, L. Zhang, J. Zhang, J. Zhou, Q. He, S. Zeng, X. Cui, J. Shi, *Chem. Comm.*, 2009, 40, 6071.
- [86] J. -W. Lang, X. -B. Yan, X. -Y. Yuan, J. Yang, Q. -J. Xue, *J. Power Sources*, 2011, 196, 10472.
- [87] J. Y. Cheon, J. Y. Cheon, C. Ahn, D. J. You, C. Pak, S. H. Hur, J. Kim, S. H. Joo, *J. Mater. Chem. A*, 2013, 1, 1270.

- [88] J. B. Xu, T.S. Zhao, RSC Advances, 2013, 3, 16.
- [89] Y. Xia, R. Mokaya, Chem. Mater., 2005, 17, 1553.
- [90] C. Liang, Z. Li, S. Dai, Angew. Chem. Int. Ed., 2008, 47, 3696.
- [91] X. Chen, K. Kierzek, Z. Jiang, H. Chen, T. Tang, M. Wojtoniszak, R. J. Kalenczuk, P. K. Chu, E. B. -Palen, J. Phys. Chem. C, 2011, 115, 17717.
- [92] H. -J. Liu, H. -J. Liu, X. -M. Wang, W. -J. Cui, Y. -Q. Dou, D. -Y. Zhao Y. -Y. Xia, J. Mater. Chem., 2010, 20, 4223.
- [93] T. Kyotani, L. -f. Tsai, A. Tomita, Chem. Mater., 1995, 7, 1427.
- [94] Z. Ma, T. Kyotani, A. Tomita, Chem. Comm., 2000, 2365.
- [95] F. Stoeckli, T. A. Centeno, A. B. Fuertes, J. Muñiz, Carbon, 1996, 34, 1201.
- [96] A. B. Fuertes, Chem. Mater., 2004, 16, 449
- [97] A. A. Zakhidov, R. H. Baughman, Z. Iqbal, C. X. Cui, I. Khayrullin, S.O. Dantas, I. Marti, V. G. Ralchenko, Science, 1998, 282, 897.
- [98] Y. Wan, D. Zhao, Chemical Reviews, 2007, 107, 2821.
- [99] S. H. Joo, S. J. Choi, I. Oh, J. Kwak, Z. Liu, O. Terasaki, R. Ryoo, Nature, 2001, 412, 169.
- [100] R. Ryoo, S. H. Joo, S. Jun, J. Phys. Chem. B, 1999, 103, 7743.
- [101] S. Jun, S. H. Joo, R. Ryoo, M. Kruk, M. Jaroniec, Z. Liu, T. Ohsuna, O. Terasaki, J. Am. Chem. Soc., 2000, 122, 10712.
- [102] J. -S. Lee, S. H. Joo, R. Ryoo, J. Am. Chem. Soc., 2002, 124, 1156.
- [103] B. Tian, S. Che, Z. Liu, X. Liu, W. Fan, T. Tatsumi, O. Terasaki, D. Zhao, Chem. Comm., 2003, 2726.
- [104] P. M. Barata-Rodrigues, T. J. Mays, G. D. Moggridge, Carbon, 2003, 41, 2231.
- [105] S. Alvarez, A. B. Fuertes, Carbon, 2004, 42, 433.
- [106] A. Lu, A. Kiefer, W. Schmidt, F. Schüth, Chem. Mater., 2004, 16, 100.
- [107] Z. -A. Qiao, B. Guo, A. J. Binder, J. Chen, G. M. Veith, S. Dai, Nano Letters, 2012, 13, 207.
- [108] Y. Meng, D. Gu, F. Zhang, Y. Shi, L. Cheng, D. Feng, Z. Wu, Z. Chen, Y. Wan, A. Stein, D. Zhao, Chem. Mater., 2006, 18, 4447.
- [109] Y. Meng, D. Gu, F. Zhang, Y. Shi, H. Yang, Z. Li, C. Yu, B. Tu, D. Zhao, Angew. Chem. Int. Ed., 2005, 44, 7053.
- [110] S. Tanaka, N. Nishiyama, Y. Egashiraa, K. Ueyamaa, Chem. Comm., 2005, 2125.
- [111] F. Zhang, Y. Meng, D. Gu, Yan, C. Yu, B. Tu, D. Zhao, J. Am. Chem. Soc., 2005, 127, 13508.
- [112] Y. Fang, D. Gu, Y. Zou, Z. Wu, F. Li, R. Che, Y. Deng, B. Tu, D. Zhao, Angew. Chem. Int. Ed., 2010, 49, 7987.
- [113] F. B. Su, J. H. Zeng, X. Y. Bao, Y. S. Yu, J. Y. Lee, X. S. Zhao, Chem. Mat., 2005, 17, 3960.
- [114] W. C. Choi, S. I. Woo, M. K. Jeon, J. M. Sohn, M. R. Kim, H. J. Jeon, Adv. Mater., 2005, 17, 446.

- [115] G. S. Chai, S. B. Yoon, J. S. Yu, J. H. Choi, Y. E. Sung, *J. Phys. Chem. B*, 2004, 108, 7074.
- [116] S. H. Joo, C. Pak, D. J. You, S. -A. Lee, H. I. Lee, J. M. Kim, H. Chang, D. Seung, *Electrochem. Acta*, 2006, 52, 1618.
- [117] J. B. Joo, P. Kim, W. Kim, J. Kim, J. Yi, *Catal. Today*, 2006, 111, 171.
- [118] N. Nakagawa, Y. Suzuki, T. Watanabe, T. Takei, K. Kanamura, *Electrochem.*, 2007, 75, 172.
- [119] K. Y. Chan, J. Ding, J. W. Ren, S. A. Cheng and K. Y. Tsang, *J. Mater. Chem.*, 2004, 14, 505.
- [120] Y. G. Wang, L. Cheng, F. Li, H. M. Xiong and Y. Y. Xia, *Chem. Mat.*, 2007, 19, 2095.
- [121] H. Chang, S. H. Joo and C. Pak, *J. Mater. Chem.*, 2007, 17, 3078.
- [122] R. C. Mani, S. Sharma, M. K. Sunkara, J. Gullapalli, R. P. Baldwin, R. Rao, A. M. Rao, J. M. Cowley, *Electrochem. Solid-State Lett.*, 2002, 5, E32.
- [123] A. E. Fischer, G. M. Swain, *J. Electrochem. Soc.* 2005, 152, B369.
- [124] Y. Hayashi, D. Mori, T. Soga, T. Jimbo, *Phys. Solid State*, 2004, 46, 733.
- [125] V. Danilenko, *Phys. Solid State*, 2004, 46, 595.
- [126] Y. V. Pleskov, *Russ. J. Electrochem.*, 2002, 38, 1275.
- [127] G. Bogatyreva, M. Marinich, E. Ishchenko, V. Gvyazdovskaya, G. Bazalii, N. Oleinik, *Phys. Solid State*, 2004, 46, 738.
- [128] K. S. Novoselov, A.K. Geim, S.V. Morozov, D. Jiang, M. I. Katsnelson, I. V. Grigorieva, S. V. Dubonos, A. A. Firsov, *Nature*, 2005, 438, 197.
- [129] Y. C. Cao, C. Xu, X. Wu, X.Wang, L. Xing, K. Scott, *J. Power Sources*, 2011, 96, 8377, 2011.
- [130] S. Liu, J. Wang, J. Zeng, J. Ou, Z. Li, X. Liu, *J. Power Sources*, 2010, 195, 4628.
- [131] L. Qu, Y. Liu, J. B. Baek, L. Dai, *ACS Nano*, 2010, 4, 1321.
- [132] N. Soin, S. S. Roy, T. H. Lim, J. A. D. McLaughlin, *Mater. Chem. Phys.*, 2011,129, 1051.
- [133] S. Guo, S. Dong, E. Wang, *ACS Nano*, 2009, 4, 547.
- [134] C. T. Hsieh, J. Y. Lin, J. L. Wei, *Int. J. Hydrogen Energy*, 2009, 34, 685.
- [135] E. Antolini, *Appl. Catal. B: Environ.*, 2007, 74, 337.
- [136] N. Jha, A. Leela Mohana Reddy, M. M. Shaijumon, N. Rajalakshmi, S. Ramaprabhu, *Int. J. Hydrogen Energy*, 2008, 33, 427.
- [137] L. Gan, R. Lv, H. Du, B. Li, F. Kang, *Electrochem. Comm.* 2009, 11, 355.
- [138] Z. Tang, C. K. Poh, K. K. Lee, Z. Tian, D. H. C. Chua, J. Lin, *J. Power Sources*, 2010, 195, 155.
- [139] C. T. Hsieh, J. L. Wei, J. Y. Lin, B. H. Yang, *Diamond Relat. Mater.*, 2011, 20, 1065.
- [140] W. Li, M. Waje, Z. Chen, P. Larsen, Y. Yan, *Carbon*, 2010, 48, 995.
- [141] S. Kang, S. Lim, D.H. Peck, S. K. Kim, D. H. Jung, S. H. Hong, *Int. J. Hydrogen Energy*, 2011, 37, 4685.
- [142] D. Sebastián, M. Lázaro, I. Suelves, R. Moliner, V. Baglio, A. Stassi, et al., *Int. J. Hydrogen Energy*, 2011, 37, 6253.

- [143] D. Sebastián, J. Calderón, J. González-Expósito, E. Pastor, M. Martínez-Huerta, I. Suelves, R. Molinera, M. J. Lázaro, *Int. J. Hydrogen Energy*, 2010, 35, 9934.
- [144] S. Song, Y. Liang, Z. Li, Y. Wang, R. Fu, D. Wu, *Appl. Catal. B: Environ.*, 2010, 98, 132.
- [145] B. Liu, S. Creager, *Electrochim. Acta*, 2010, 55, 2721.
- [146] L. Calvillo, M. Gangeri, S. Perathoner, G. Centi, R. Moliner, M. J. Lázaro, *Int. J. Hydrogen Energy*, 2011, 36, 9805.
- [147] L. B. Kong, H. Li, J. Zhang, Y. C. Luo, L. Kang, *Appl. Surf. Sci.*, 2010, 256, 6688.
- [148] G. Liu, X. Li, P. Ganesan, B. N. Popov, *Appl. Catal. B: Environ.*, 2009, 93, 156.
- [149] E. P. Ambrosio, C. Francia, M. Manzoli, N. Penazzi, P. Spinelli, *Int. J. Hydrogen Energy*, 33, 2008, 3142.
- [150] Z. P. Sun, X. G. Zhang, Y. Y. Liang, H. Tong, R. L. Xue, S. D. Yang, *J. Electroanal. Chem.*, 2009, 633, 1.
- [151] K. K. Tintula, A. K. Sahu, A. Shahid, S. Pitchumani, P. Sridhar, A. K. Shukla, *J. Electrochem. Soc.*, 2010, 157, B1679.
- [152] H. Chang, S. H. Joo, C. Pak, *J. Mater. Chem.*, 2007, 17, 3078.
- [153] G. R. Salazar-Banda, H. B. Suffredini, M. L. Calegario, S. T. Tanimoto, L. A. Avaca, *J. Power Sources*, 2006, 162, 9.
- [154] G. R. Salazar-Banda, K. I. B. Eguluz, L. A. Avaca, *Electrochem. Commun.*, 2007, 9, 59.
- [155] G. R. Salazar-Banda, H. B. Suffredini, L. A. Avaca, S. A. S. Machado, *Mater. Chem. Phys.*, 2009, 117, 434.
- [156] X. Lu, J. Hu, J.S. Foord, Q. Wang, *J. Electroanal. Chem.*, 2011, 654, 38.
- [157] S. Liu, J. Wang, J. Zeng, J. Ou, Z. Li, X. Liu, et al., *J. Power Sources*, 2010, 195, 4628.
- [158] L. Qu, Y. Liu, J. B. Baek, L. Dai, *ACS Nano*, 2010, 4, 1321.
- [159] S. Guo, S. Dong, E. Wang, *ACS Nano*, 2009, 4, 547.
- [160] S. H. Joo, S. J. Choi, I. Oh, J. Kwak, Z. Liu, O. Terasaki, R. Ryoo, *Nature*, 2001, 412, 169.
- [161] H. Chang, S. H. Joo, C. Pak, *J. Mater. Chem.*, 2007, 17, 3078.
- [162] J. -S. Yu, S. Kang, S. B. Yoon, G. Chai, *J. Am. Chem. Soc.*, 2002, 124, 9382.
- [163] B. Fang, J.H. Kim, M. Kim, J.-S. Yu, *Chem. Mater.*, 2009, 21, 789.
- [164] L. Calvillo, M. Gangeri, S. Perathoner, G. Centi, R. Moliner, M.J. Lazaro, *Inter. J. Hydrogen Energy*, 2011, 36, 9805.
- [165] R. Balgis, G. M. Anilkumar, S. Sago, T. Ogi, K. Okuyama. *J. Power Sources*, 2012, 203, 26.
- [166] S. Kundu, T. C. Nagaiah, X. Chen, W. Xia, M. Bron, W. Schuhmann, M. Muhler, *Carbon*, 2012, 50, 4534.
- [167] Y. S. Yun, H. Bak, H.-J. Jin, *Synthetic Metals*, 2010, 160, 561.
- [168] IUPAC Compendium of Chemical Terminology, 2nd ed., 1997, 31.
- [169] IUPAC Compendium of Chemical Terminology, 2nd ed.; 1997, 46.

- [170] J. Aizenberg, J. C. Weaver, M. S. Thanawala, V. C. Sundar, D. E. Morse, P. Fatzl, *Science*, 2005, 309, 275.
- [171] C. Zou, D. C. Wu, M. Z. Li, Q. C. Zeng, F. Xu, Z. Y. Huang, R. W. Fu, *J. Mater. Chem.*, 2010, 20, 731.
- [172] B. -Z. Fang, J. -H. Kim, M. -S. Kim, A. Bonakdarpour, A. Lam, D. Wilkinson, J. -S. Yu, *J. Mater. Chem.*, 2012, 22, 19031.
- [173] H. L. Wang, Y. Yang, Y. Y. Liang, J. T. Robinson, Y. G. Li, A. Jackson, Y. Cui, H. J. Dai, *Nano Lett.*, 2011, 11, 2644.
- [174] B. -Z. Fang, M. -W. Kim, S. -Q. Fan, J. -H. Kim, D. Wilkinson, J. -J. Ko, J. -S. Yu, *J. Mater. Chem.*, 2011, 21, 8742.
- [175] B. -Z. Fang, J. -H. Kim, M. -S. Kim, J. -S. Yu, *Langmuir*, 2008, 24, 12068.
- [176] T. L. Kelly, T. Gao, M. J. Sailor, *Adv. Mater.*, 2011, 23, 1776.
- [177] B. -Z. Fang, J.-H. Kim, M. -S. Kim, J. -S. Yu, *Chem. Mater.*, 2009, 21, 789.
- [178] P. -Z. Li, Y. Zhao, *Chem.-Asian J.*, 2013, 8, 1680.
- [179] A. Huczko, *Appli. Phys. A: Mater. Science & Processing*, 2000, 70, 365.
- [180] L. Chuenchom, R. Kraehnert, B. M. Smarsly, *Soft Matter*, 2012, 8, 10801.
- [181] C. T. Kresge, M. E. Leonowicz, W. J. Roth, J. C. Vartuli, J. S. Beck, *Nature*, 1992, 359, 710.
- [182] C. Liang, Z. Li, S. Dai, *Angew. Chem. Int. Ed.*, 2008, 47, 3696.
- [183] D. Zhao, Q. Huo, J. Feng, B. F. Chmelka, G. D. Stucky, *J. Am. Chem. Soc.*, 1998, 120, 6024.
- [184] J. H. Knox, B. Kaur, G. R. Millward, *J. Chromatography A*, 1986, 352, 3.
- [185] W. Wei, H. Liang, K. Parvez, X. Zhuang, X. Feng, K. Müller, *Angew. Chem., Int. Ed.*, 2014, 53, 1570.
- [186] Y. Wang, X. Wang, M. Antonietti, *Angew. Chem., Int. Ed.*, 2012, 51, 68.
- [187] X. Wang, K. Maeda, X. Chen, K. Takanabe, K. Domen, Y. Hou, X. Fu, M. Antonietti, *J. Am. Chem. Soc.*, 2009, 131, 1680.
- [188] J. Liang, Y. Zheng, J. Chen, J. Liu, D. Hulicova-Jurcakova, M. Jaroniec, S. Z. Qiao, *Angew. Chem. Int. Ed.*, 2012, 51, 3892.
- [189] S. Feng, W. Li, Q. Shi, Y. Li, J. Chen, Y. Ling, A. M. Asiri, D. Zhao, *Chem. Comm.*, 2014, 50, 329.
- [190] Q. Shi, R. Zhang, Y. Lv, Y. Deng, A. Elzatahrya, D. Y. Zhao, *Carbon*, 2015, 84, 335.
- [191] W. Shen, W. Fan, *J. Mater. Chem. A*, 2013, 1, 999.
- [192] S. Maldona, K. J. Stevenson, *J. Phys. Chem. B*, 2005, 109, 4707.
- [193] R. A. Sidik, A. B. Anderson, N. P. Subramanian, S. P. Kumaraguru, B. N. Popov, 2006, 110, 1787.
- [194] S. H. Lim, H. I. Elim, X. Y. Gao, A. T. S. Wee, W. Ji, J. Y. Lee, J. Lin, *Phys. Review B*, 2006, 73, 045402.

- [195] V. K. Tran, H. G. Na, D. S. Kwak, Y. J. Kwon, H. Ham, K. B. Shim, H. W. Kim, *J. Mater. Chem.*, 2012, 22, 17992.
- [196] R. Czerw, M. Terrones, J. -C. Charlier, X. Blase, B. Foley, R. Kamalakaran, N. Grobert, H. Terrones, D. Tekleab, P. M. Ajayan, W. Blau, M. Rühle, D. L. Carroll, *Nano Letters*, 2001, 1, 457.
- [197] W. Yang, T. -P. Fellingner, M. Antonietti, *J. Am. Chem. Soc.*, 2010, 133, 206.
- [198] R. Liu, D. Wu, X. Feng, K. Müllen, *Angew. Chem. Int. Ed.*, 2010, 49, 2565.
- [199] Y. Chang, F. Hong, C. He, Q. Zhang, J. Liu, *Adv. Mater.*, 2013, 25, 4794.
- [200] G. Wu, K. L. More, C. M. Johnston, P. Zelenay, *Science*, 2011, 332, 443.
- [201] C. H. Choi, S. H. Park and S. I. Woo, *J. Mater. Chem.*, 2012, 22, 12107.
- [202] A. Velázquez-Palenzuela, L. Zhang, L. Wang, P. L. Cabot, E. Brillas, K. Tsay, J. Zhang, *J. Phys. Chem. C*, 2011, 115, 12929.
- [203] D. Geng, Y. Y. Chen, Y. Li, R. Li, X. Sun, S. Ye and S. Knights, *Energy Environ. Sci.*, 2011, 4, 760.
- [204] Y. Tang, S. C. Burkert, Y. Zhao, W. A. Saidi, A. Star, *J. Phys. Chem. C*, 2013, 117, 25213.
- [205] W. Yuan et al., *Sci. Rep.*, 2013, 3, 2248.
- [206] R. d'Agostino, P. Favia, C. Oehr, M. R. Wertheimer, *Plasma Processes Polym.*, 2005, 2, 7.
- [207] Q. Chen, L. Dai, M. Gao, S. Huang, A. Mau, *J. Phys. Chem. B*, 2001, 105, 618.
- [208] H. Wang, T. Maiyalagan and X. Wang, *ACS Catal.*, 2012, 2, 781.
- [209] D. Yu, Q. Zhang, L. Dai, *J. Am. Chem. Soc.*, 2010, 132, 15127.
- [210] J. R. Pels, F. Kapteijn, J. A. Moulijn, Q. Zhu, K. M. Thomas, *Carbon*, 1995, 33, 1641.
- [211] D. S. Su, J. Zhang, B. Frank, A. Thomas, X. Wang, J. Paraknowitsch, R. Schlögl, *ChemSusChem*, 2010, 3, 169.
- [212] H. Niwa, M. Kobayashi, K. Horiba, Y. Harada, M. Oshima, K. Terakura, T. Ikeda, Y. Koshigoe, J. -I. Ozaki, S. Miyata, S. Ueda, Y. Yamashita, H. Yoshikawa, K. Kobayashi, *J. Power Sources*, 2011, 196, 1006.
- [213] P. H. Matter, L. Zhang, U. S. Ozkan, *J. Catal.*, 2006, 239, 83.
- [214] H. Kim, K. Lee, S. I. Woo, Y. Jung, *Phys. Chem. Chem. Phys.*, 2011, 13, 17505.
- [215] W. Yuan, Y. Zhou, Y. Li, C. Li, H. Peng, J. Zhang, Z. Liu, L. Dai, G. Shi, *Sci. Rep.*, 2013, 3, 2248.
- [216] A. Shen, Y. Zou, Q. Wang, R. A. W. Dryfe, X. Huang, S. Dou, L. Dai, S. Wang, *Angew. Chem. Int. Ed.*, 2014, 53, 10804.
- [217] D. Yu, Q. Zhang, L. Dai, *J. Am. Chem. Soc.*, 2010, 132, 15127.
- [218] S. Kundu et al., *J. Phys. Chem. C*, 2009, 113, 14302.
- [219] H. Li, W. Kang, L. Wang, Q. Yue, S. Xu, H. Wang, J. Liu, *Carbon*, 2013, 54, 249.
- [220] C. V. Rao, C. R. Cabrera, Y. Ishikawa, *J. Phys. Chem. Lett.*, 2010, 1, 2622.
- [221] K. A. Kurak, A. B. Anderson, *J. Phys. Chem. C*, 2009, 113, 6730.

- [222] J. Yan, H. Meng, F. Xie, X. Yuan, W. Yu, W. Lin, W. Ouyang, D. Yuan, *J. Power Sources*, 2014, 245, 772.
- [223] S. Maldonado, K. J. Stevenson, *J. Phys. Chem. B*, 2005, 109, 4707.
- [224] J. D. Wiggins-Camacho, K. J. Stevenson, *J. Phys. Chem. C*, 2009, 113, 19082.
- [225] H. Niwa, K. Horiba, Y. Harada, M. Oshima, T. Ikeda, K. Terakura, J.-i. Ozaki, S. Miyata, *J. Power Sources*, 2009, 187, 93.
- [226] R. Liu, D. Wu, X. Feng, K. Müllen, *Angew. Chem. Int. Ed.*, 2010, 49, 2565.
- [227] E. Yeager, *J. Mol. Catal.*, 1986, 38, 5.
- [228] A. J. Bard, L. R. Faulkner, New York: Wiley, 1980.
- [229] H. S. Wroblowa, Y. C. Pan, G. Razumney, *J. Electroanal. Chem.*, 1976, 69, 195.
- [230] S. Maass, F. Finsterwalder, G. Frank, R. Hartmann, C. Merten, *J. Power Sources*, 2008, 176, 444.
- [231] P. Serp, J. L. Figueiredo, *Carbon Material for Catalysis*, John Wiley & Sons, Inc., Publication, New Jersey, 2009.
- [232] S. Maldonado, K. J. Stevenson, *J. Phys. Chem. B*, 2005, 109, 4707.
- [233] A. B. Fuertes, T. A. Centeno, *J. Mater. Chem.*, 2005, 15, 1079.
- [234] P. Scherrer, N. M. Götinger, *Phys.*, 1918, 2, 98.
- [235] F. Rouquerol, J. Rouquerol, K. Sing, London, Academic Press, 1999.
- [236] A. C. Ferrari, J. C. Meyer, V. Scardaci, C. Casiraghi, M. Lazzeri, F. Mauri, S. Piscanec, D. Jiang, K. S. Novoselov, S. Roth, A. K. Geim, *Phys. Rev. Lett.*, 2006, 97, 187401.
- [237] C. Coutanceau, P. Crouigneau, J. M. Leger, C. Lamy, *J. Electroanal. Chem.*, 1994, 379, 389.
- [238] I. Radev, K. Koutzarov, A. Pfrang, G. Tsotridis, *Int. J. Hydrogen Energy*, 2012, 37, 11862.
- [239] J. C. Meier, C. Galeano, I. Katsounaros, A. A. Topalov, A. Kostka, F. Schüth, K. J. J. Mayrhofer, *ACS Catal.*, 2012, 2, 832.
- [240] J. Mitzel, F. Arena, H. Natter, T. Walter, M. Batzer, M. Stefener, R. Hempelmann, *Int. J. Hydrogen Energy*, 2012, 37, 6261.
- [241] A. Marinkas, F. Arena, J. Mitzel, G. M. Prinz, A. Heinzl, V. Peinecke, H. Natter, *Carbon*, 2013, 58, 139.
- [242] J. Liu, D. Takeshi, K. Sasaki, S. M. Lyth, *Fuel Cells*, 2014, 14, 728.
- [243] F. Su, C. K. Poh, J. S. Chen, G. Xu, D. Wang, Q. Li, J. Lin, X. W. Lou, *Energy Environ. Sci.*, 2011, 4, 717.
- [244] H. Wang, T. Maiyalagan, X. Wang, *ACS Catal.*, 2012, 2, 781.
- [245] Z. -H. Sheng, L. Shao, J. -J. Chen, W. -J. Bao, F. -B. Wang, X. -H. Xia, *ACS Nano*, 2011, 5, 4350.
- [246] K. Chen, Z. Chai, C. Li, L. Shi, M. Liu, Q. Xie, Y. Zhang, D. Xu, A. Manivannan, Z. Liu, *ACS Nano*, 2016, 10, 3665.
- [247] W. J. Ong, L. L. Tan, S. P. Chai, S. T. Yong, *Chem. Commun.*, 2015, 51, 858.

- [248] R. Sharmaa, K. K. Kar, J. Mater. Chem. A, 2015, 3, 11948.
- [249] A. Primo, P. Atienzar, E. Sanchez, J. M. Delgado, García, Chem. Commun., 2012, 48, 9254.
- [250] K. Zhang, Y. Zhang, S. Wang, Sci. Rep., 2013, 3, 3448.
- [251] J. Liu, D. Takeshi, K. Sasaki, S. M. Lyth, J. Electrochem. Soc., 2014, 161, F838.
- [252] W. H. Bailey, Theses, Dissertations, 2008, 1024.
- [253] Y. Yua et al., Nanoscale, 2015, 7, 12343.
- [254] J. P. Paraknowitsch, A. Thomasa, M. Antonietti, J. Mater. Chem., 2010, 20, 6746.
- [255] J. P. Paraknowitsch, J. Zhang, D. Su, A. Thomasa, M. Antonietti, Adv. Mater., 2010, 22, 87.
- [256] C. H. Choi, S. H. Park, S. I. Woo, ACS Nano, 2012, 6, 7084.
- [257] A. C. Ferrari, J. Robertson, Phys. Rev. B, 2000, 61, 14095.
- [258] Y. Yang, J. Dong, Z. Yao, C. Shen, X. Shi, Y. Tian, S. Lin, X. Zhang, Sci. Rep., 2014, 4, 4501.
- [259] S. Some, J. Kim, K. Lee, A. Kulkarni, Y. Yoon, S. Lee, T. Kim, H. Lee, Adv. Mater., 2012, 24, 5481.
- [260] Z. Liu, F. Peng, H. Wang, H. Yu, W. Zheng, J. Yang, Angew. Chem., Int. Ed., 2011, 50, 3257.
- [261] R. Li, Z. Wei, X. Gou, W. Xu, RSC Adv., 2013, 3, 9978.
- [262] Y. Fu, Y. Huang, Z. Xiang, G. Liu, D. Cao, Eur. J. Inorg. Chem., 2016, 13-14, 2100.
- [263] A. C. Ferrari et al., Phys. Rev. Lett., 2006, 97, 187401.
- [264] F. Tuinstra, J. L. Koenig, J. Chem. Phys., 1970, 53, 1126.
- [265] Y. Wang, D. C. Alsmeyer, R. L. McCreery, Chem. Mater., 1990, 2, 557.
- [266] C. Coutanceau, P. Crouigneau, J. M. Leger, C. Lamy, J. Electroanal. Chem., 1994, 379, 389.
- [267] J. Zhang, Y. Mo, M. B. Vukmirovic, R. Klie, K. Sasaki, R. R. Adzic, J. Phys. Chem. B, 2004, 108, 10955.
- [268] J. S. Lee, X. Q. Wang, H. M. Luo, S. Dai, Adv. Mater., 2010, 22, 1004.
- [269] J. P. Paraknowitsch, A. Thomas, M. Antonietti, J. Mater. Chem., 2010, 20, 6746.
- [270] J. P. Paraknowitsch, J. Zhang, D. S. Su, A. Thomas, M. Antonietti, Adv. Mater., 2010, 22, 87.
- [271] Bayer Material Science AG. Kaiser-Wilhelm-Allee 51368, Leverkusen, Germany.  
<http://www.baytubes.com>
- [272] Z. Chen, D. Higgins, H. Tao, R.S. Hsu, Z. Chen, J. Phys. Chem. C, 2009, 113, 21008.
- [273] C. Y. Du, P. F. Shi, X. Q. Cheng, G. P. Yin, Electrochem. Comm., 2004, 6, 435.

## 9.5 Publications

### 9.5.1 Journal Articles

- 1) **E. -J. Oh**, R. Hempelmann, V. Nica, I. Radev, H. Natter, A new type of hierarchical porous carbon foams, *Energy Environ. Sci.*, rejected, June, 2016.
- 2) **E. -J. Oh**, R. Hempelmann, V. Nica, I. Radev, H. Natter, New catalyst supports prepared by surface modification of graphene- and CNT-structures with nitrogen containing carbon coatings, *J. Power Sources*, submitted, July, 2016.
- 3) **E. -J. Oh**, H. Natter, R. Hempelmann, Hierarchical nanostructured N-doped graphene foams prepared by thermal decomposition, *Verein Koreanischer Naturwissenschaftler und Ingenieure in der BRD e.V. News Letter*, p3, May, 2016.
- 4) **E. -J. Oh**, S. W. Kim, H. Natter, R. Hempelmann, PEM fuel cells with graphene-supported Pt catalysts, *Environment & Energy News Letter*, p87-88, 2013.

### 9.5.2 Presentations

- 1) **E. -J. Oh**, R. Hempelmann, H. Natter, Highly efficient fuel cell electrodes from few-layer graphene sheets prepared by high power ultrasound, Electrochemistry 2016, Goslar, Germany, Sep. 26-28, 2016.
- 2) **E. -J. Oh**, R. Hempelmann, H. Natter, Highly conductive catalyst supports for fuel cell applications prepared by surface modification of Graphene- and CNT-structures, Europe-Korea Conference on Science and Technology (EKC) 2016, Berlin, Germany, July 27-30, 2016.
- 3) **E. -J. Oh**, R. Hempelmann, H. Natter, Hierarchical structured conductive N-doped carbon pores for energy conversion applications, The 3rd Forum of Korean Expert Community on Material Science and Technology in Europe, Praha, Czech Republic, April 15-17, 2016.
- 4) **E. -J. Oh**, H. Natter, R. Hempelmann, Mesoporous N-doped graphene-based catalysts for oxygen reduction reaction in PEM fuel cells, EKC 2015, Strasbourg, France, July 22-24, 2015.
- 5) **E. -J. Oh**, Mixtures of graphene/CNT supports as an electrode in fuel cells, EU-Korean scientists and engineers workshop, Saarbrücken, Germany, July 19, 2014.
- 6) **E. -J. Oh**, S. W. Kim, Graphene-supported Pt catalyst as electrode material for PEMFCs, EU Korean scientist and engineers association, Essen-Heidhausen, Germany, Oct. 25- 27, 2013.

### 9.5.3 Posters

- 1) I. Radev, A. -K. Egetenmeyer, **E. -J. Oh**, D. Durneata, V. Peinecke, H. Natter, R. Hempelmann, M. Baumgärtner, R. Freudenberger, Optimization of electrochemically deposited Pt and Pt<sub>3</sub>Co for PEMFC cathods, Duisburg, Germany, June 17, 2016.
- 2) **E. -J. Oh**, R. Hempelmann, H. Natter, New catalyst supports for energy conversion prepared by surface modification of Graphene- and CNT-structures, Bunsentagung, Rostock University, Rostock, Germany, May 4-6, 2016.
- 3) **E. -J. Oh**, H. Natter, R. Hempelmann, Hierarchical nanostructured N-doped graphene foams prepared by thermal decomposition, Doktorandentag, Saarland University, Saarbrücken, Germany, Nov. 11, 2015.
- 4) **E. -J. Oh**, R. Hempelmann, H. Natter, High-performance N-doped graphene foam as a catalyst support for PEM fuel cells, Bunsentagung 2015, Ruhr-Universität Bochum, Bochum, Germany, May 14-16, 2015.
- 5) **E. -J. Oh**, D. Durneata, H. Natter, R. Hempelmann, Platinum-supported mesoporous graphene as anodic catalyst for polymer electrolyte membrane fuel cells, Electrochemistry 2014, Mainz, Germany, Sep. 22-24, 2014.
- 6) **E. -J. Oh**, S. W. Kim, H. Natter, R. Hempelmann, Nanostructures consisting of graphene and carbon nanotubnes for catalyst support in fuel cells, Doktorandentag, Saarland University, Saarbrücken, Germany, Nov. 10, 2014.
- 7) **E. -J. Oh**, S. W. Kim, H. Natter, R. Hempelmann, Graphene based electrode materials for PEM fuel cells and electrochemical oxygen reduction reaction, Doktorandentag, Saarland University, Germany, Nov. 13, 2013.

### 9.5.4 Awards

- 1) Received a Prize for the best presenter, 11th local region of VekNI conference, KIST Europe, Germany, Feb. 06, 2016.  
“Hierarchical structured N-doped graphene foams as new catalyst support for oxygen reduction reaction”
- 2) Received a Prize for the best PhD poster, Natural Science and Technology Facility III, Saarland University, Germany, Dec. 12, 2013.  
“Graphene based electrode materials for PEM fuel cells and electrochemical oxygen reduction reaction”
- 3) PhD scholarship, International Max Planck Research School (IMPRS), Oct. 27, 2011.

Saarbrücken, den

---

Eun-Jin Oh

---